

**Wave-induced Topographic Change in
Soil Structures Composed of
Dredged Sand**

CHO Yong-Hwan

Wave-induced Topographic Change in Soil Structures Composed of Dredged Sand

CHO Yong-Hwan

Supervised by
Assoc. Prof. NAKAMURA Tomoaki

Coastal & Ocean Engineering Laboratory

Department of Civil Engineering

Nagoya University

JAPAN

ACKNOWLEDGEMENT

First and foremost, I would like to stick out my sincere gratitude to my academic advisor Assoc. Prof. Tomoaki NAKAMURA, Nagoya University, for the everlasting inestimable guidance and encouragement, insightful comments and delicate attention throughout my PhD. course. His navigations as well as subjective and objective discussions gave lots of both enlightenment and assurance to me. Any words are no substitute for my appreciation to him. The growth of my understandings and abilities attributes to my academic advisor.

I would further like to thank this dissertation committee, Prof. Norimi MIZUTANI, Nagoya University; Prof. Tetsuro TSUJIMOTO, Nagoya University; and Assoc. Prof. Shigeru KATO, Toyohashi University of Technology, for taking the time for their valuable suggestions constructive criticisms and careful reviews. I warmly thank to Ex-Assoc. Prof. Koji KAWASAKI, Hydro-soft Technology Institute; and Assist. Prof. Masami KIKU, Nagoya University, for our weekly technical seminar and interesting talks during seminars.

My colleagues at the Coastal Engineering Laboratory provided a sound home base where scientific thoughts are freely shared and exchanged. I wish to express my sincere gratitude to Ryo ISHIHARA, Yuta NEZASA and Manami SUZUKI for their helpful guidance and technical and physical supports in my research. I would also like to thank Kazuki SUZUKI as a captain in our laboratory for mathematical support.

I am grateful to Prof. Kwang-Ho LEE, Kwan Dong University, Korea; and Jae-Jun KIM who supported me to be acclimated and used to life in Japan. Special thanks to Hye-Ryeon AN and Bae-Ho JEON who are always making me comfortable like family in Japanese life.

I gratefully acknowledge the financial support over three years of my Doctoral study by Ministry of Education, Culture, Sports, Science and Technology (MEXT), Japan. Their generous scholarship program has made it possible for me to study at Nagoya University.

I would also like to thank Prof. Yong-Jun CHO, University of Seoul, Korea, for his assistance and guidance in getting my master course. He provided me with the foundation for studying abroad and becoming a coastal engineer with his deep affections.

No student can make it through such an educational process without help from outside of academia. I would extend this appreciation to also include my parents, Yong-Suk KIM and Gun-Sik CHO, who have done nothing but consistently encourage me throughout my entire educational career. "I love mom and I love dad."

Table of Contents

ACKNOWLEDGEMENT	i
LIST OF TABLES	v
LIST OF FIGURES	vii
ABSTRACT	xi
 CHAPTER 1. INTRODUCTION	
1.1 Background and Motivation	01
1.2 Literature Review	07
1.2.1 Incipient motion	07
1.2.2 Forces acting on a particle	09
1.2.3 Shields diagram	09
1.2.4 Hjulström diagram	10
1.2.5 Bed load and suspended load	12
1.2.6 Cohesive sediment transport	14
1.3 Study Objectives	17
1.4 Study Contents	18
 CHAPTER 2. WAVE-INDUCED TOPOGRAPHIC CHANGE IN AN ARTIFICIAL SHALLOWS	
2.1 General	21
2.2 Hydraulic Experiments	23
2.3 Results and Discussion	25
2.3.1 Topographic change in the shallows	25
2.3.2 Influences of bottom flow velocity and pore-water pressure	32
2.3.3 Modified Shields parameter considering the effects of pore-water pressure	38
2.4 Remarks	41
 CHAPTER 3. COMPUTATIONAL ANALYSIS	
3.1 General	43
3.2 Numerical Model Description	44
3.2.1 Generalized Navier-Stokes Solver (GNS)	46
3.2.2 Sediment Transport Module (STM)	47

3.3	Numerical Conditions	49
3.4	Validation of the Mean Water Level	51
3.5	Effects of Still Water Level on the Topographic Change in the Shallows	55
3.6	Suspended Sediment Concentration	58
3.7	Remarks	62

CHAPTER 4. SEDIMENT TRANSPORT CALCULATION CONSIDERING COHESIVE EFFECTS

4.1	General	63
4.2	Sediment Transport Calculation Considering Cohesive Effects	64
4.2.1	Critical Shields parameter	66
4.2.2	Bed load sediment transport rate	67
4.3	Characteristics of Sediment Transport Calculation Considering Cohesive Effects	68
4.4	Three-dimensional Coupled Fluid-Structure-Sediment Interaction Model	70
4.5	Application of the Modified Model Considering Cohesive Effects	71
4.5.1	Numerical condition	71
4.5.2	Effects of the cohesive force on the topographic change in shallows	72
4.6	Remarks	75

CHAPTER 5. INFLUENCE OF COHESIVE SEDIMENTS ON TOPOGRAPHIC CHANGE IN A TIDAL FLAT

5.1	General	77
5.2	Experimental Description	78
5.2.1	Open channel experiment	78
5.2.2	Wave flume experiment	79
5.3	Sediment Transport in the Open Channel	80
5.4	Results in the Wave Flume Experiment	82
5.4.1	A tidal flat profile evolution	82
5.4.2	Evaluation of signed critical Shields parameter	87
5.4.3	Application of the modified sediment calculation	92
5.5	Remarks	96

CHAPTER 6. CONCLUSIONS

REFERENCES	103
-------------------------	------------

LIST OF TABLES

Table 1.1	Recent trend of harbor freight dealt with in Japan (Source: Japanese Ministry of Land, Infrastructure, Transport and Tourism, 2010).	02
Table 1.2	The volume of dredged soil in Japan in 2008 (Source: Japanese Ministry of Land, Infrastructure, Transport and Tourism, 2010).	03
Table 1.3	The volume of dredged soil for each area in Japan in 2008 (Source: Japanese Ministry of Land, Infrastructure, Transport and Tourism, 2010).	03
Table 1.4	The volume of dredged soil for management with soil property (Source: Japanese Ministry of Land, Infrastructure, Transport and Tourism, 2010).	05
Table 2.1	Experimental conditions.	24
Table 2.2	C_s values.	30
Table 3.1	Parameters in the FSSM.	50
Table 5.1	Sediment conditions for the open channel experiment.	78
Table 5.2	Experimental conditions for the wave flume experiment.	80
Table 5.3	C_s values for Cases 7-11.	87

LIST OF FIGURES

Figure 1.1	The proportion of the components in dredged soil in 2008 (Source: Japanese Ministry of Land, Infrastructure, Transport and Tourism, 2010).	04
Figure 1.2	The proportion of dredged soil with soil property between different areas in Japan (Source: Japanese Ministry of Land, Infrastructure, Transport and Tourism, 2010).	04
Figure 1.3	The proportion of the management of dredged soil with soil property (Source: Japanese Ministry of Land, Infrastructure, Transport and Tourism, 2010).	05
Figure 1.4	Shields diagram for incipient motion (COE, 1996).	10
Figure 1.5	Hjulström diagram depicting critical flow velocities with different grain size (Hjulström, 1939).	11
Figure 2.1	Schematic of the experimental setup (W1-W6: wave gauge, P1-P8: pore-water pressure transducer, V1: velocimeter).	23
Figure 2.2	Surface profile of the shallows z at $t_e = 0, 30$ and 60 min.	26
Figure 2.3	Topographic changes in the shallows Δz for $0 \leq t_e \leq 30$ min and $30 \leq t_e \leq 60$ min.	26
Figure 2.4	Sediment transport rate q for $0 \leq t_e \leq 30$ min and $30 \leq t_e \leq 60$ min.	27
Figure 2.5	Topographic changes in the shallows after the completion of wave generating for the still water depth $h = 0.225$ m (upper figure: the initial and final surface profiles of the shallows z ; middle figure: the topographic change in the shallows Δz and the sediment transport rate q ; lower figure: the non-dimensional wave height H/H_i and the non-dimensional mean water level $\bar{\eta}/H_i$).	28
Figure 2.6	Topographic changes in the shallows after the completion of wave generation for the still water depth $h = 0.275$ m (upper figure: the initial and final surface profiles of the shallows z ; middle figure: the topographic change in the shallows Δz and the sediment transport rate q ; lower figure: the non-dimensional wave height H/H_i and the non-dimensional mean water level $\bar{\eta}/H_i$).	31
Figure 2.7	Temporal change in the signed Shields parameter φ_d at $x = 3.6$ m early after the initiation of the wave generating.	33
Figure 2.8	Relationship between the signed Shields parameter φ_d and the relative vertical effective normal stress ratio γ at $x = 3.6$ m for the first 1 min.	35

Figure 2.9	Temporal change in the signed Shields parameter φ_d and the relative vertical effective normal stress ratio γ at $x = 3.6$ m early after the initiation of the wave generation.	35
Figure 2.10	Relationship between the signed Shields parameter φ_d and the relative vertical effective normal stress ratio γ at $x = 3.6$ m for $0 \leq t_e \leq 1$ min and $30 \leq t_e \leq 31$ min in the cases of $d_{50} = 0.1$ mm.	36
Figure 2.11	Temporal change in the signed Shields parameter φ_d and the relative vertical effective normal stress ratio γ at $x = 3.6$ m after $t_e = 30$ min in Case 4.	36
Figure 2.12	Temporal change in the signed Shields parameter φ_d and the relative vertical effective normal stress ratio γ at $x = 3.6$ m early after the initiation of the wave generation in Case 8.	39
Figure 2.13	Temporal change in the signed Shields parameter φ_d and the modified signed Shields parameter φ_{dm} at $x = 3.6$ m early after the initiation of the wave generating.	39
Figure 2.14	Temporal change in the signed Shields parameter φ_d and the modified signed Shields parameter φ_{dm} at $x = 3.6$ m after $t_e = 30$ min for $d_{50} = 0.1$ mm.	40
Figure 3.1	Two-way coupling procedure of the FSSM.	45
Figure 3.2	Schematic numerical wave flume for a shallow profile change against regular waves: W2 to W6 are wave gages and P1 to P8 are pore-pressure gages.	49
Figure 3.3	Time series of water surface elevation predicted at W2, W3, W4, W5 and W6 for $h = 0.2250$ and 0.2275 m.	52
Figure 3.4	Time series of the pore-water pressure in the shallows at P1, P2, P3 and P4 for $h = 0.2250$ and 0.2275 m.	54
Figure 3.5	Cross-shore distribution of: (a) final shallows profile and (b) topographic change with different still water levels of $h = 0.2250$ and 0.2275 m.	56
Figure 3.6	Distribution of the horizontal velocity u	57
Figure 3.7	Cross-shore distribution of: (a) suspended sediment concentration and (b) topographic change for $h = 0.2250$ m at $t = 19.8, 20.5, 24.0, 26.3, 34.5, 38.4,$ and 57.6 s.	59
Figure 3.8	Cross-shore distribution of: (a) suspended sediment concentration and (b) topographic change for $h = 0.2275$ m at $t = 19.8, 20.5, 24.0, 26.3, 34.5, 38.4,$ and 57.6 s.	61
Figure 4.1	The concept of sand-clay mixture (Ashida <i>et al.</i> , 1982).	65
Figure 4.2	Force balance on a sediment particle on a sloping bed in the critical state.	66

Figure 4.3	Force balance on a moving sediment particle on a sloping bed.	68
Figure 4.4	Non-dimensional bed load sediment transport rate q_* versus the Shields parameter τ_* : (a) the characteristic of q_* according to ω ; (b) the characteristic of q_* according to p_f ; and (c) the characteristic of q_* according to f_c	69
Figure 4.5	Computational domain for the topographic change in the shallows.	71
Figure 4.6	Difference in the amount of topographic change Δz caused by the cohesive force at $t = 60$ s: (a) the effects of the cohesive force per unit surface area ($\omega = 0.5, p_f = 0.15$); (b) the effects of the water content ($p_f = 0.15, f_c = 0.1 \text{ N/m}^2$); (c) the effects of the content ratio of the clay ($\omega = 0.5, f_c = 0.1 \text{ N/m}^2$).	73
Figure 4.7	Comparison of cross-shore distribution of the suspended sediment concentration at $t = 24$ s: (a) with non-cohesive effect; (b) $f_c = 0.1 \text{ N/m}^2$; (c) $f_c = 0.5 \text{ N/m}^2$; (c) $f_c = 1.0 \text{ N/m}^2$ ($\omega = 0.5, p_f = 0.15$).	74
Figure 5.1	Set-up for steady flow experiments.	78
Figure 5.2	Set-up for wave flume experiments.	80
Figure 5.3	Longitudinal averaged sediment transport rate computed from bed evolution measurements in Cases 1-6.	81
Figure 5.4	Cross-shore distribution of: tidal flat profile z (upper); topographic change Δz (middle); and non-dimensional wave height H/H_i and mean water level η/H_i (lower) at experimental time $t = 1, 30, 60$ and 300 min.	83
Figure 5.5	Time distribution of signed Shields parameter ϕ_d at $x = 1.50$ m (upper) and 2.00 m (middle) during $t = 1-30$ min and topographic change Δz (lower) at $t = 30$ min.	88
Figure 5.6	Topographic change Δz and time distribution of the signed Shields parameter ϕ_d at $x = 2.00$ m with the modified critical Shields parameter ϕ_{cm} for Case 11 during $t = 1-30$ (upper), $30-60$ (middle) and $60-300$ min (lower).	90
Figure 5.7	Schematic of the computational domain for topographic change in the tidal flat.	92
Figure 5.8	Time series of non-dimensional water surface elevation against incident waves H_i predicted at W1, W2, W3, W4, W5, W6 and W7 during 1 min.	93
Figure 5.9	Cross-shore distribution of topographic change Δz with comparison between the measured data and the predicted results for $f_c = 0.0, 2.5$ and 5.0 N/m^2	94

ABSTRACT

Wave-induced Topographic Change in Soil Structures Composed of Dredged Sand

Constructions of tidal flats and shallows with dredged sand near coastal regions have a variety of benefits in coastal environments and calmness, while dredged sand contains not inconsiderable cohesive sediments. One of the major required understandings is the cohesive effects on erosion in mixed sediments. However, few studies on the structural stability of mixed soil structures against waves have been conducted, thus there is little understanding about the behavior of mixed sediments, *i.e.*, cohesive and non-cohesive sediments, in wave fields. Therefore, this is a foundational study to understand the characteristics of wave-induced topographic change in soil structures composed of dredged sand in free-clay and mixed soil conditions, numerically and experimentally.

The present study consists of mainly four subjects. First, the behavior of sediment transport for fine sand targeting dredged sand is investigated experimentally focusing on pore-water pressure effects on wave-induced topographic change in artificial shallows composed of fine sand. Second, as a methodology, a three-dimensional two-way coupled fluid-structure-sediment interaction model is applied to the experimental investigation to confirm the predictive capability of the model with the general characteristics of sediment transport calculations. Third, a sediment transport calculation considering cohesive force induced by clay surrounding sand particles is proposed and incorporated into the aforementioned model to examine the characteristics of the modified model. Last, laboratory experiments are implemented in terms of cohesive effects on sediment transport in an open channel and wave-

induced topographic change in a tidal flat composed of both sand and sand-clay mixtures in a wave flume. The cohesive effects on topographic change are investigated and the applicability of proposed calculation to the assessment of topographic change is validated.

Consequently, this study draws the following conclusions. From experimental results presenting the variation of pore-water pressure on the surface layer of the shallows, which is related to the incipient sediment motion, pore-water pressure should be considered in the evaluation of the stability of soil structures composed of fine sand. The modified sediment transport scheme considering cohesive effects shows an increase in the resistance as well as the different trend of bed load transport rate. In addition, it is found in the experiments that containing clay in the tidal flat leads to the less topographic change without ripple formation as well as different shoreline displacement. The proposed sediment calculation scheme presents the applicability to the estimation of sediment transport in the mixed soil condition, experimentally and numerically.

Keywords: *Sediment transport, cohesive effect, topographic change, tidal flat, shallows*

Chapter 1

INTRODUCTION

1.1 Background and Motivation

The civilization has drawn a lot of convenient human lives in various aspects. River projects to improve flood risk management, raise flood embankments and remove debris blocking culverts contribute to the communities of homes and business from the risk of the likelihood of flooding and the damage. The construction of dams, which were built at the location where sufficient water is available, meets the demand of human for water supply, irrigation, flood control, navigation and energy. Moreover, evolutions of shipbuilding technology over the last decades have brought people increasingly active maritime trade between countries worldwide with the vast capacity of maritime transport and the continuity of the services in a time when an international trade becomes essential. Among these noticeable developments in human lives, the evolution in coastal area is examined closely.

Specifically, according to the Japanese Ministry of Land, Infrastructure, Transport and Tourism, the recent trend of harbor freight in Japan shows a rapid growth for latest decades (**Table 1.1**). The total quantity of trade rapidly increased in 1960s to 1970s by a factor of four. The amount of trade was constantly increasing until 1990s, and the increased trade amount was sustained until 2010s. Furthermore, the development of coastal area in company with maritime trade encourages people to employ their leisure in coastal regions such as fishing, sailing and relaxing adjacent to the sea. However, such artificial developments commonly accompany with some maintenance problems such as dredging works, particularly near coastal region.

2 Chapter 1

Table 1.1 Recent trend of harbor freight dealt with in Japan (Source: Japanese Ministry of Land, Infrastructure, Transport and Tourism, 2010).

unit: ton (million), %

	1950	1960	1970	1980	1990	2000	2006	2007	2008	2009	2010
Total	118.54	439.94	1,852.55	2,908.62	3,251.98	3,177.30	3,200.97	3,214.96	3,145.73	2,633.56	2,801.51
Foreign trade	17.80	107.03	552.91	828.36	968.97	1,137.40	1,256.47	1,291.55	1,299.03	1,091.90	1,232.30
Export & Import container			6.36	49.03	115.28	192.31	246.05	254.78	252.91	217.47	251.35
The rate of Containerization			1.2	5.9	11.9	16.9	19.6	19.7	19.5	19.9	20.4
Export	4.17	14.82	59.90	152.55	171.14	203.24	284.81	303.83	309.79	244.81	282.35
Export container			3.90	29.09	62.57	82.97	107.02	113.69	110.06	91.59	108.73
The rate of Containerization			6.5	19.1	36.6	40.8	37.6	37.4	35.5	37.4	38.5
Import	13.66	92.21	493.01	675.81	797.83	934.16	971.66	987.72	989.24	847.09	949.95
Export container			2.47	19.94	52.71	109.34	139.04	141.08	142.85	125.88	142.62
The rate of Containerization			0.5	3.0	6.6	11.7	14.3	14.3	14.4	14.9	15.0
Domestic trade	100.72	332.90	881.60	1,238.24	1,278.95	1,201.27	1,154.61	1,167.41	1,130.78	928.61	972.54
Ferry			418.04	842.02	1,004.06	838.63	789.89	755.99	715.92	613.05	596.66

The dredging work is underwater excavation to help to ensure the continuous availability of the desired depths in shipping channels of ports, fishing harbors and other maritime organizations. The increase in maritime trade traffic boosts utilization of harbor, so that the navigation management is of primary importance. Commercial and recreational maritime transportation relies on the maintenance of adequate water depth. Therefore, periodic dredging has been required due to natural accumulations generated from frequent sailing of vessels. Specifically, about 1.5-2.3 million cubic meters of dredged soil is born annually from major and minor ports, recreational harbors and connecting channels. More than 91% of dredged soil was generated from major ports in Japan, which was reported from the Japanese government in 2010 (**Table 1.2**). In the detailed instance, dredging works usually were carried out for navigation channel, anchorage, excavation and the other works and more than half of the volume of dredged soil was generated from the work in navigation channel in the major ports across the country in Japan (**Table 1.3**). New dredging works contained the projects deepening and widening navigation channels.

Table 1.2 The volume of dredged soil in Japan in 2008 (Source: Japanese Ministry of Land, Infrastructure, Transport and Tourism, 2010).

unit: m³ (thousand)

Year	Major ports	Minor ports	Sum total
2008	18,964	1,869	20,833

Table 1.3 The volume of dredged soil for each area in Japan in 2008 (Source: Japanese Ministry of Land, Infrastructure, Transport and Tourism, 2010).

	The place of occurrence								
	Total	Navigation channel			Anchorage			Excavation	The others
		New	Maintenance	Total	New	Maintenance	Total		
Hokkaido	565	357	0	357	106	71	177	29	2
Tohoku	821	39	112	151	353	248	601	69	0
Kanto	4,415	797	824	1,621	680	589	1,269	138	1,388
Hokuriku	2,856	899	794	1,693	1,088	63	1,151	12	0
Chubu	2,926	1,408	354	1,762	649	388	1,037	123	4
Kinki	2,748	1,772	194	1,966	545	112	657	116	9
Chugoku	747	430	55	485	218	34	252	09	1
Shikoku	323	3	8	8	170	18	188	125	2
Kyusyu	3,108	2,044	62	2,106	722	141	863	139	1
Okinawa	455	31	0	31	304	0	304	10	11
Sum total	18,964	7,777	2,402	10,179	4,835	1,663	6,498	771	1,516

On the basis of the data, Japanese government organization investigated components of the dredged sediments from each local region in Japan. As shown in **Fig. 1.1**, most of dredged sediments were composed of finer sediments such as cohesive sediments of 62%. The definition of cohesive sediments in size depends on researchers, while cohesive sediments are defined by the sediments smaller than 62.5 μm in this study according to the definition of Mitchener and Torfs (1996). Many people have common sense in regard to dredged soil composed of mud or clay, whereas there exists considerable amount of 33% sandy soil, and small volume of gravel and bedrock is also contained in dredged soil. The proportion of the components in dredged soil fairly relies on dredged region as shown in **Fig. 1.2**. Therefore, the management of dredged soil is not such an easy undertaking because of a wide variety of soil including cohesive sediments.

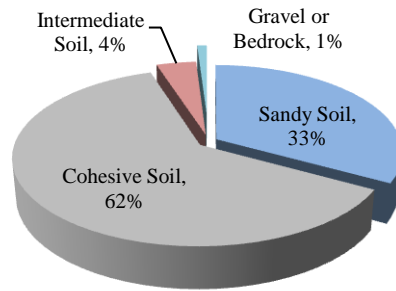


Fig. 1.1 The proportion of the components in dredged soil in 2008 (Source: Japanese Ministry of Land, Infrastructure, Transport and Tourism, 2010).

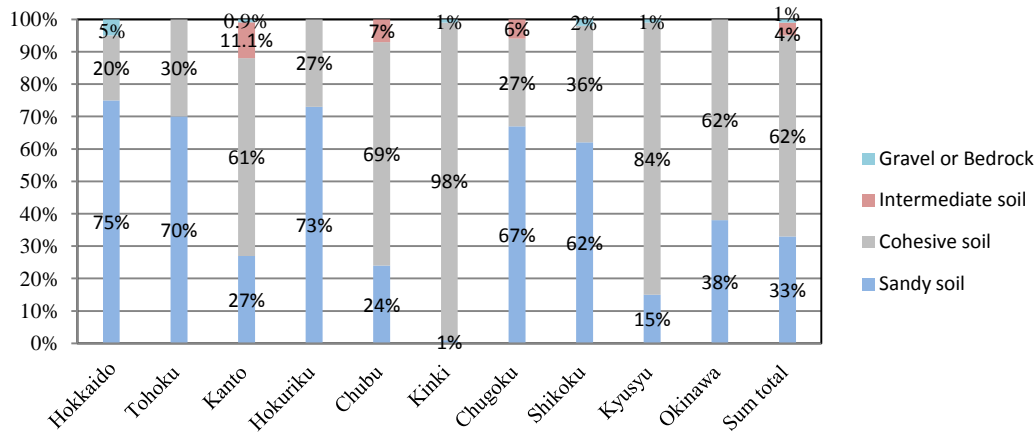


Fig. 1.2 The proportion of dredged soil with soil property between different areas in Japan (Source: Japanese Ministry of Land, Infrastructure, Transport and Tourism, 2010).

Dredged soil has been used in various fields such that clean sandy material is utilized to beach nourishment. There are some technologies and applications of beneficial use in general (Greak Lakes Commission, 2013). In the perspective of engineered uses, dredged soil is managed by beach nourishment to provide a source of nourishment for natural sand movement or to restore a beach, capping using relatively clean dredged material to covering sediments on aquatic environment to provide a layer of cleaner material so that the contaminated material will not be harmful to human health or the marine environment, land creation for shore protection and improvement through reclamation and replacement fill substituting soils or other sediments which moved or removed for construction or landscaping projects. Besides, dredged soil has been used in topsoil enhancement mixing with other material and construction materials such as bricks and concrete employed in road construction or riprap foundation. Although dredged soil is applied to a variety of area, the restrictions to manage dredged sediments still remain with respect to cohesive

Table 1.4 The volume of dredged soil for management with soil property (Source: Japanese Ministry of Land, Infrastructure, Transport and Tourism, 2010).

unit: m³ (thousand)

	Disposal site						
	Total	Harbor reclamation	Overlaying / Tidal flat	Beach nourishment	Harbor work	Airport work	Stockyard
Sandy Soil	6,328	2,036	566	239	11	0	149
Cohesive Soil	11,684	1,977	1,597	10	179	2,287	65
Intermediate Soil	753	634	0	4	0	0	3
Gravel / Bedrock	172	25	0	0	32	0	49
National total	18,937	4,672	2,163	379	222	2,287	293

Disposal field	Ocean disposal	The other constructions	Inland disposal
2,810	53	35	429
4,654	742	38	45
19	0	0	30
66	0	0	0
7,550	795	73	504

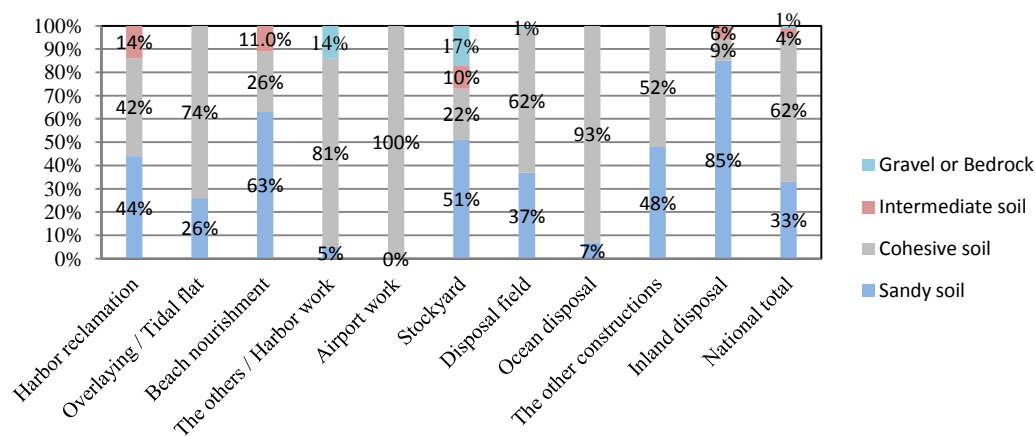


Fig. 1.3 The proportion of the management of dredged soil with soil property (Source: Japanese Ministry of Land, Infrastructure, Transport and Tourism, 2010).

sediments. **Table 1.4** and **Figure 1.3** show the current state of the application of dredged soil well. **Table 1.4** shows the trend of the applications of sandy soil to beach nourishment and inland disposal, and cohesive soil to overlaying and tidal flat construction, harbor work, airport construction and ocean disposal. Nevertheless, large volume of dredged soil, both sandy and cohesive sediments, is abandoned in

disposal fields. Thus, managements of dredged soil are a still remained subject to utilize dredged soil effectively.

Constructing artificial shallows, tidal flats and overlaying sand using dredged sand was one of the effective applications of dredged soil. Kazama *et al.* (2006) presented the positive influence in marine environment near shore with increasing bottom livings and self-purification capacity of coast seawater. Particularly, artificial shallows are also expected as a natural submerged breakwater functioning enhancement in port calmness, recovery of ecosystem, improvement of water quality and recreational spaces. However, the stability of near-shore structures is concerned due to fine sediments mainly consisting of the structures, which are vulnerable to incident waves owing to relatively light weight. Actually, the installed earth structures consisted of finer sand with the median grain size $d_{50} = 0.15$ mm. Therefore, an investigation of the stability of the near-shore structures composed of dredged sand is required for the improvement in durability and the economic utilization.

The stability problem in those structures composed of dredged sand is closely related to the erodibility of sediments. Conventionally, many studies on erosion problems have been carried out focusing on the behavior of either non-cohesive or cohesive sediments due to considerably different sediment properties. Non-cohesive sediments rely on the gravitational force to erosion, while cohesive sediments are influenced by the inter-particle force such as ionic charges. However, as mentioned earlier, no small quantity of cohesive sediments are predicted in dredged sand used in the construction of the earth structures (Kazama *et al.*, 2006). Therefore, overall understanding of sediment transport characteristics of both cohesive sediments and non-cohesive sediments is required as well as an investigation of the stability problem in a mixed soil condition.

From a numerical point of view in hydrodynamics, engineer's capability of hydraulic solution is rapidly leaped up after the computer era. In pre-computer era, engineering problem-solving process was arisen from analytical or exact solution serving outstanding insight of the specific hydraulic phenomenon, graphic solution, *e.g.*, plots or nomographs, and manual devices. However, these approaches to solving engineering problem have many limitations in simple geometry, low dimensionality, low precision, awkwardness and inconsistent results. Pre-computer techniques

imposed engineers on tremendous amounts of endeavor to solution performance itself. The development of digital computers in the late 1940s and the easy availability of personal computers in the present have contributed to relieving engineer's hard works and extending their potential to significantly elaborate problem solution with highly efficient numerical tools, which deal with many equations, non-linearity phenomenon, complex geometries and diverse hydraulic conditions.

1.2 Literature Review

In a few decades, study on sediment transport problem closely related to the stability problem of earth structures as a basic approach has concentrated on the prediction of the flow strength or intensity, expressed in terms of either a critical shear stress or a threshold shear stress, when incipient movements of individual sediments take place. The investigators have interested in the problem of sediment transport regarded as the minimum shear stress at which an individual particle moves or the maximum grain size moved by an allowed shear stress. In sediment-free condition commonly adopted, incipient motion is one of the important issues in simplified sediment transport problem. The incipient motion of the bed particles relies on the external forces. Generally, the forces acting on an individual particle are particle weight forcing downward and inter-particle contact forces exerted upward, normally with three contact points and fluid forces. Inter-particle contact forces are usually subordinated to the other forces. The particle weight is a manageable term, while the fluid forces are much more difficult. There are some variables governing the fluid force on a particle, that is, the particle diameter D relevant to surface area of the particle and the particle projects, the fluid viscosity μ , the fluid density ρ , the boundary or bed shear stress τ_0 , which is the best characterizing the flow strength around the particle, and the geometry of the particle (Kelin, 2004). Among these variables, τ_0 is a good indicator of the incipient movement in the threshold condition and represents the average of the forces in the vicinity of the particles.

1.2.1 Incipient motion

In sediment transport problem, the most important issue is an incipient motion of a particle giving an explanation of bed stability and morphological evolution. An understanding of incipient motion of sediments is usually applied to bed load calculation mostly based on the bed shear stress induced by bottom flow exceeding a

threshold/critical stress (Yalin, 1977). There are two ways to attempt to identify the threshold motion. One is the watch-the-bed technique, which is direct observation. Neil (1968) and Yalin (1977) are representative investigators using the technique, who attempted to quantify the conditions of incipient motion. Another method is the reference-transport-rate method, which is to avoid the uncertainty of the moment of incipient movement. This method is defining a small specific value representing the threshold condition, and then the value is extrapolated from bed load transport rates.

Shields (1936) and Carling (1983) defined the incipient particle motion as mean boundary/bed shear stress moving the particles. Einstein and El-Samni (1949) and Sumer and Deigaard (1981) presented stochastic approaches with turbulent stresses. Kramer (1935), Vanoni *et al.* (1966) and Fenton and Abbott (1977) treated the incipience of particle motion at the moment when the fewer particles begin to move. However, these studies were established by laboratory experiments and analysis of the research implemented by Shields (1936) introducing similarity theory to incipient motion, which is widely employed all over the world until now. In fact, the concept of threshold condition was first suggested by Duboys (1879). In the same context, a number of researchers have concentrated efforts to account for Shields' study experimentally and theoretically despite of some criticisms in Shields diagram (Dey and Raju, 2002).

Petit (1994) demonstrated that the incipient motion of a particle can be expressed by shear stress itself and a morphological structure of bottom has considerable effects on initiation of movement for bed such as imbrication with high resistance and protrusion liable to erode in common with Fenton and Abbott (1977). Dancey *et al.* (2002) proposed a new criterion of initiation of motion condition as bed load for experimental characterization with probability concept presuming that the threshold motion takes place when the force/moments acting on a particle is the completely same as the force/moments holding out in motion. He associated the packing density of bed to threshold movement of bed particles.

The definition and derived treatment of incipient motion of a particle have been developed by various researchers. However, there was little correlation between them, unfortunately. Most researches on incipient motion of a particle depended on individual tendency of researchers. In this study, the author takes the theory of Shields

diagram defined by a function of dimensionless stress and grain diameter in place of boundary Reynolds number, which is an original indicator in Shields diagram, into basis of incipient motion of particles. This study puts more weight on wave induced topographic evolution based on an incipient motion of a particle, thus less efforts are given in an in-depth study on an establishment of critical Shields parameter itself, a non-dimensional term with a shear stress when a particle is first in motion.

1.2.2 Forces acting on a particle

Particles begin to move when resultant forces induced by the flow, which are drag forces parallel to the bed and lift forces normal to the bed, are larger to counteract forces that make the particles stay in-situ such as gravity and friction forces produced by particles. These drag and lift forces have been measured directly by many investigators with epoch-making techniques in laboratory experiments (Einstein and El-Samni, 1949; Chepil, 1958, 1961; Coleman, 1967). Since the degree of exposure of particles to flow is different and the fluid forces are not constant with time due to turbulence in the flow, defining a single fluid force able to apply to all particles on the bed is scarcely possible in general (Kelin, 2004). Thus, an average concept was introduced that an average fluid force is considered with an average particle in an average position on the bed. The theory taking into account the force balance between fluid drag force and the submerged weight of a particle was derived by White (1940) and Egiazaroff (1965). The lift force, which was first introduced by Jeffreys (1929), was incorporated into the force balance between drag force and submerged weight (Coleman, 1967; Wiberg and Smith; 1987).

1.2.3 Shields diagram

Shields diagram (**Fig. 1.4**) was plotted by Shields (1936) from flume experiments on a graph of boundary shear stress non-dimensionalized by the submerged specific weight and the median sediment size versus the boundary Reynolds number. The non-dimensionalized variable is well known Shields parameter. Shields parameter is the simplified description relevant to incipient motion of particles and indicates the critical value of a dimensionless variable with a function of grain geometry and boundary Reynolds number. The variables accounting for incipient motion is pretty straightforward: the boundary shear stress τ_0 , the particle diameter D , the fluid viscosity μ , the fluid density ρ , the particle density ρ_s and submerged specific weight

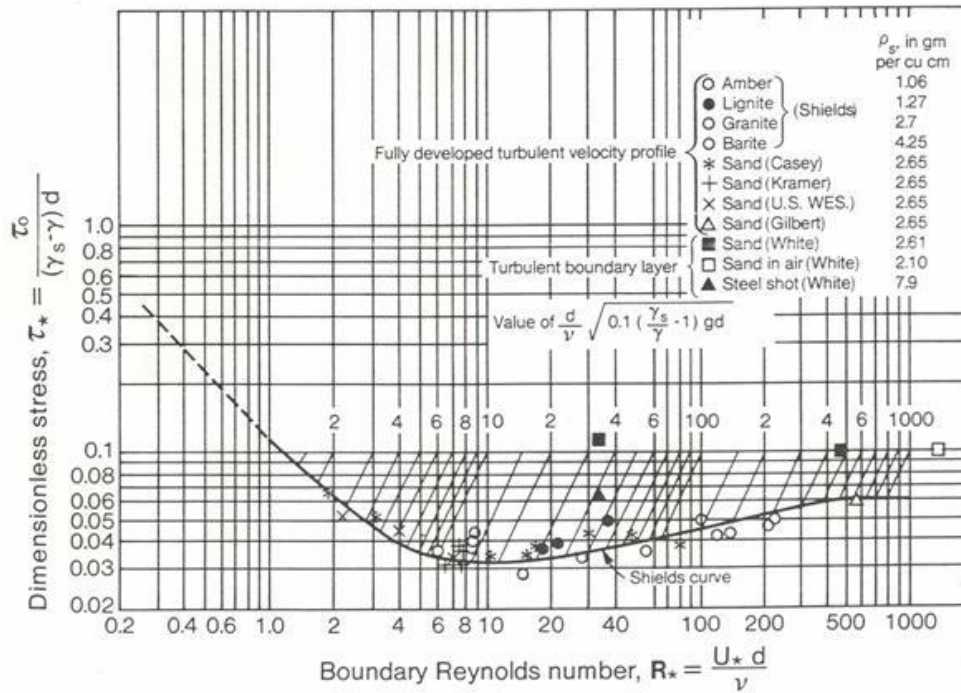


Fig. 1.4 Shields diagram for incipient motion (COE, 1996).

γ . Flow depth is not important because only the local layer, which is inner side of turbulent boundary layer of the flow, involves in the incipient motion of the bed particle. Accordingly, non-dimensionalizing Shields parameter can be described by:

$$\frac{\tau_c}{\gamma' D} = f\left(\frac{\rho u_* D}{\mu}\right), \quad (1.1)$$

in which τ_c is the threshold value of the bed shear stress. Shields diagram adopted the boundary shear stress rather than a velocity in virtue of a difficulty to specify a velocity actually engaging in particle motion. However, Shields diagram is sometimes modified into a form with interest variable such as flow velocity and flow depth. Miller *et al.* (1977) replotted the Shields diagram and redrew the curve by adding various recent data. Moreover, they recast the diagram into two equivalent dimensionless variables, D and τ_0 separately, because of inconvenience to find the threshold shear stress or critical Shields parameter corresponding to the specific particle diameter due to D and τ_0 belonging to both of the axis variables.

1.2.4 Hjulström diagram

Hjulström diagram (Fig. 1.5) is also a representative indicator to investigate sediment transport problem, which is usually used and cited by sedimentationists

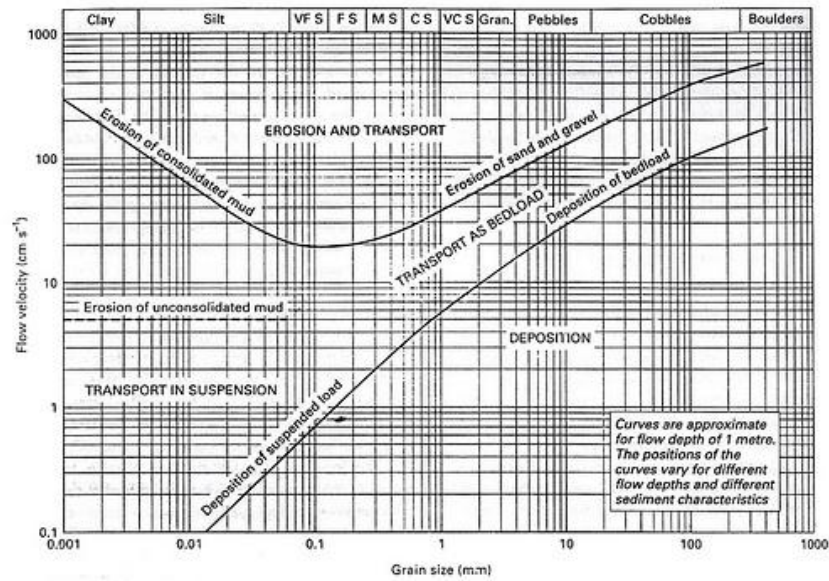


Fig. 1.5 Hjulström diagram depicting critical flow velocities with different grain size (Hjulström, 1939).

(Hjulström, 1939). The diagram represents the boundaries among erosion, transportation and deposition with flow velocity against particle size. He detected a minimum critical flow velocity occurred for particles with 0.5 mm diameter. In contrast with Shields diagram, which rarely dealt with small particle diameters and did not include cohesive effects, those effects were taken into account in Hjulström diagram with two separated empirical equations. Sunborg (1956) updated the Hjulström diagram with several water depths corresponding to the threshold movement for the separated curves. He used the flow velocity as the flow strength and included different levels of cohesion. Postma (1967) improved the Hjulström diagram making mention of consolidated and unconsolidated soils. Dou (1962) presented the velocity distribution for the direct application of Hjulström diagram with the bed roughness, while the proposed curve fitting Hjulström diagram is overestimated rather than the typical one for water level of 1 m.

Some researchers contributed to the zone existing cohesive effects for finer sediment diameter in Hjulström diagram. Zanke (1892) regarded that cohesive forces are induced by surface tension which is originated by small film surrounding particles. Based on the assumption, he derived sliding and rolling equations considering cohesive effects with the factor K including the factor c that represents the degree of the cohesive effects between particles. He said the value of c is equal to 1 when natural sand condition (Zanke, 2003). Besides cohesive zone, he also derived an

approximation equation for Hjulström curve with average flow velocities (Zanke, 1977). Dade *et al.* (1992) incorporated adhesive and cohesive forces into rolling motion of particles in an equilibrium moment condition. In a similar vein, critical shear stress versus grain diameter was proposed by several researchers. Chepil (1959) presented the relation between critical shear stress and grain diameter only for coarse particles with little thought of cohesive forces. White (1970) extended the relation to fine particles. The general modeling of cohesive effects based on several experiments was given by Lick *et al.* (2004). He presumed the relation between cohesive forces and sediment diameters has proportional correlation. The additional binding force introduced by Lick *et al.* (2004) was able to account for the experimental results for 2%-bentonite mixture exceeding original Shields diagram. Miedema (2013) took the concept of the van der Waals forces ingenerated by silt fractions into the modeling of cohesive effects and developed it.

These studies associated with cohesive forces are subordinate to either non-cohesive particles or the particles with weak cohesive bonding such as silt based on the relatively feeble forces, surface tension and van der Waals force. The results are valuable to accounting the necessity for the investigation of cohesive effects in very small size particles for itself as well as the role to influence larger cohesionless particles. The author employs these similar approaches to investigate cohesive effects or cohesive forces in mixed soil structures containing cohesive sediments. More description is presented in Section 1.3.

1.2.5 Bed load and suspended load

Sediment transport modes are conventionally classified by three "loads", wash load, bed load and suspended load. Wash load is the finest particles of the load transported through a flow. These particles are not placed in the bed. Therefore, wash load was typically negligible in sediment transport problem. Bed load and suspended load are sometimes called "bed-material load" due to the particles on the bed traveled by the form of bed load and suspend load. Bed load is the part of the total load and is subdivided into saltating, rolling and sliding. Bed load generally moves slowly than the flow near the bed surface and takes place locally and randomly. Thus, bed load is either discontinuous or un-uniform. Bed load is typically determined by effective shear stress, normally known as threshold/critical shear stress, acting on the particle

directly. Suspended load is moving without continuous contact in the bed and traveling for long distances with flow intensity, which is expressed by the boundary shear stress τ_0 , near the bed. If the finer particles are on the bed and the flow intensity is stronger, the concentration of the suspended load becomes higher. Therefore, the suspended load is closely related to flow intensity, τ_0 . Suspended load is composed of particles of the fine sand, silt and clay. The existing transport rate formulas came from these separated three different transport modes and some investigators still have efforts on improving equations.

Practical prediction of sediment transport rate was derived in 1950s by Einstein (1950) whose achievement is one of the first theoretical approaches of bed load transport rate applying the probability theory to agitating force induced by turbulence near bed particles. He assumed the mean distance between detached position and subsequent reattachment of a traveling sand particle is proportional to the grain size (diameter) without regard to the hydraulic conditions and the volume of sand on the basis of laboratory experiments. In addition, he presented the number of reattached particles should be equal to the number of detached them in an equilibrium condition. Bagnold (1954) suggested separated form of the total shear stress into the fluid stress transmitted by the intergranular fluid and the grain shear stress entraining sediment particles for the sake of account for drawback of the Einstein theory that the continuative erosion would occur on the layers simultaneously when the bed stress exceeds the threshold stress of bottom. Subsequently, Luque and van Beek (1976) developed the theory of Bagnold considering the incipient motion of an individual particle with the results that bed load controls erosion rate reducing the max fluid shear stress. Engelund and Fredsøe (1976, 1982) simplified the bed load formula containing time-averaged quantities and expended the formula to a transverse motion of a bed load particle on a slope.

Suspended load is defined as sediment particles transported by fluid turbulence rather than intergranular collisions which cause bed load (Wilson, 1966). The mechanism of vortices, which trap particles on the bed with the horizontal transverse axes, was explained by Tooby *et al.* (1977) at the very beginning. As suspended load expression, Engelund and Fredsøe (1976) introduced the dispersive stress decreased rapidly away from the bed and presented a reasonable estimation of the maximum

value for suspended load in motion. Garcia and Parker (1991) updated the value of dynamic friction coefficient μ_d around 0.50 to 0.65 rather than 1.0 which value gives too low bed concentration at low dimensionless bed shear stress. The awareness of the importance in oscillating flow generated by surface wave behavior has derived some concepts which are a delay distance idea (Hattori, 1969) and the time lag hypothesis for small particles in purely oscillating flows (Bhattacharya, 1971). Defining the suspended load concentration is a substantially hard subject because of the difficulties to separate the suspended load and the bed load from the measured total load. Horikawa *et al.* (1982) gave the criteria for the inception of sheet flow to enable to separate the suspended load from the total sediment concentration in the several experiments, whose results generally corresponded to the advanced researches (Manohar, 1955; Komar and Miller, 1974). The modeling of suspended sediment transport is basically separated into two processes, which are the pick up process from the bed and the mechanism of distribution of particles through fluid. Conventional approaches are based on the assumption of equilibrium state between bed/boundary shear stress and sediment transport rate in steady and uniform flow conditions. However, because there is little relationship with real conditions, Nielsen *et al.* (1978) proposed a new approach for oscillatory flow by treating sediment migration and accretion independently. More detailed information of bed load and suspended load is described in Fredsøe and Deigarrd (1992) for bed load transport and Nielsen (1992) for suspended load transport.

1.2.6 Cohesive sediment transport

The characteristics of the movement of the non-cohesive sediments can be summarized readily based on the numerous advanced researches and they are mainly depending on physical properties of the particles such as the density, size/diameter and shape. However, the cohesive sediments migrate with very complicated variables such as not only soil structure and composition, but fluid composition. The biggest discrepancy between the incipient motion of non-cohesive sediments and cohesive sediments is the strength of the attracting cohesive force between inter-particles on which cohesive sediments heavily depend. For the correct understanding of the terms of cohesive force or cohesion, it is necessary to be the exact naming convention. In this study, cohesive force is a physical property between two dissimilar sediments, *e.g.*, clay and sand, induced by intermolecular attraction acting to stick each other.

Cohesive force can be distinguished by mechanical, chemical and electrostatic cohesion. The author defines the term, cohesive force, taking in a contrary sense of adhesive force and cohesive force defined by Miedema (2013).

The classification of cohesive sediments is not manageable by the size and distribution of particles. However, sediment diameters smaller than $2\ \mu\text{m}$ are generally considered as cohesive sediments, *i.e.*, clay and mud. If the median sediment diameter, d_{50} , is greater than $65\ \mu\text{m}$, the sediments are coarse cohesionless sediments such as sand, pebble and rubble. Silt is in the intermediate state with the grain size, $2\ \mu\text{m} \leq d_{50} \leq 65\ \mu\text{m}$. If silt is characterized by cohesive properties, it is due to the existence of clay in the silt. Cohesive sediments consist of inorganic minerals, which are subdivided into clay mineral (*e.g.*, silica, alumina, montmorillonite, illite and kaolinite), non-clay mineral (*e.g.*, quartz, carbonate and others) and organic minerals (plant, animal debris and bacteria).

The weight of an individual fine particle is too light to involve in sediment transport because all particles will be suspended despite of small turbulence fluctuation. Instead, the inter-particle forces dominate the settlement of the finer particles because of their ionic charges on the surface of the particles tending to bind together to increase their body and weight. The floc structure formed by inter-particle forces is determining the settling velocity according to shape, density and size, which are obtained from experiments and normally expressed by an empirical constant. The characteristics of aggregates cause the erosion in the form of large flakes or chunks of aggregates, called by mass erosion (Millar and Quick, 1998). It is different from surface erosion easily observed on the non-cohesive bed, in which erosion is described by removal of individual particles.

A lot of parameters are characterizing cohesive sediments relevant to the erosion behavior such as temperature, oxygen content, pH, sodium adsorption ratio, organic content, bulk density, specific surface and the others. These parameters can be grouped primarily by three classifications, which are physical effects, electro-chemical effects and biological effects. Recently, the biological factors were issued due to the substantial impact on cohesive sediment erosion (Paterson, 1994). Physical factors affecting erodibility contain the particle properties such as clay content, water content, clay type, bulk density, pore pressure and the history of the deposition. There

are many unfamiliar parameters in electrochemical factors such as Cation Exchange Capacity (CEC) (Arulanandan, 1975; Ariathurai and Arulanandan, 1978), pH level of the pore fluid (Ravisanger *et al.*, 2001), salinity in fluid (Sherard *et al.*, 1972; Kelly and Gularte, 1981; Parchure and Mehta, 1985), Sodium Adsorption Ratio (SAR) (Arulanandan, 1975) and Natural Organic Matter (NOM) (Schnitzer and Khan, 1972; Bennett *et al.*, 1991; Dennett *et al.*, 1998). The summary of the results of each parameter is not described in this paper since the bed is rarely composed of only clay components because of fine sand and silt consisting of the large portion of the bed with clay, occasionally. Moreover, the author considers mixed soil conditions targeting dredged sand excluding any electro-chemical and biological effects due to complexity, thus concentrates on only physical properties of cohesive sediments in this study.

There are no comprehensive expressions for the erosion form of cohesive sediments despite of a great number of studies on cohesive sediment behavior. Only one or two parameters were included in the studies due to much variables and complexities. The investigation of cohesive sediment behavior in fluid covers not only hydraulics, sedimentation mechanics and soil mechanics, but electrochemistry. Consequently, understanding of cohesive sediment erosion problem has not been fully accomplished until the present.

Although numerous studies about erosion and sediment problems were implemented for decades, there are still remained several blanks in understandings of sediment transport mechanism in cohesive sediments because of the dependence of each studies on case-by-case empirical methods with little correlations between them beside in non-cohesive sediments which led to appropriate agreements in general, numerically and experimentally.

Meanwhile, as aforementioned, dredged soil consists of quite a large volume of cohesive and finer sediments, thus cohesive sediments should exists in dredged sand. It seems to tend to behave like non-cohesive sediments, but not thoroughly because of the existence of cohesive sediments, *e.g.*, silt and clay.

1.3 Study Objectives

The ultimate objective of this study is to understand wave-induced topographic change of earth structures composed of dredged sand near coast against incident waves in the interests of an effective application of dredged soil. A study for apprehending dredged sand behavior requires comprehensive understandings of the characteristics of both cohesive and non-cohesive sediments based on their physical and electrochemical features. The direct treatment of dredged sand is considered as an unsuitable choice due to fairly many variables affecting sediment transport of earth structures for cohesive sediments as demonstrated in a lot of advanced researches. Accordingly, in current situation of a lack of understandings in cohesive sediments, it is more important to trace the influence on one another between non-cohesive and cohesive sediments and parameterize them rather than straightly undertake dredged sand in the practical side of the application and analysis. Therefore, prior to investigating the structural stability of the earth structures composed of dredged sand, the understanding of the sediment transport system in a mixed soil condition is a precedence assignment. Furthermore, the research of in-situ observations and laboratory experiments can offer practical clues to analyze sediment transport, but produce rarely practical uses directly because of commonly known limitations of the results relying on the performed method and the similarity laws in experiments with regard to sediments. Thus, relieving this kind of problems turns up in a computational analysis which is possible to extend our knowledge to both more detailed portion of the mechanism and more wide area estimating.

In general, there are two approaches to analyze the sediment transport problem in a mixed soil condition. One is to add non-cohesive sediments gradually to cohesive sediments. This approach bears the uncertainty and the uncontrollability for the aforementioned many effective variables leading to parameterization with difficulties. Another one is the analysis in a mixture conditions putting cohesive sediments into non-cohesive sediments. The advantages of this approach are a better accessibility and a higher availability based on well developed knowledge of non-cohesive sediments than the former approach. In addition, the dredged sand is targeted in this study. Therefore, the latter approach is adopted in this study to understand the behavior characteristics in a mixed soil condition.

As a basic study for an effective application of dredged sand, the author have carried out experimental and numerical studies to investigate the characteristics of wave-induced topographic change and sediment transport in coastal structures composed of pure fine sand and mixed sediments, which are sand-kaolin mixtures. There are primary two targeted soil structures in the present study as follows:

- Shallow structures composed of fine sand.
- Tidal flat structures composed of fine sand and sand-kaolin mixtures.

Above all, the study is conducted experimentally to investigate the responses of topographic change in a shallow structure composed of fine sand, which is hydraulically modeled based on the actual structure installed in Mikawa bay, against a variety of approaching waves. Subsequently, numerical analysis is implemented by using a three-dimensional coupled fluid-structure-sediment interaction model (referred to as FSSM) developed by Nakamura *et al.* (2011) to verify the predictive capability of the model based on the experimental results. As a consecutive work, the time-dependent sediment calculation considering cohesive sediment effects in a mixed soil condition is developed and applied to the wave-induced topographic change simulation. Lastly, the effects of cohesive sediments on wave-induced topographic change in mixed sediment condition are investigated experimentally and the performance of the developed calculation is verified. The series of this study can be summarized as follows with respective aspects:

- The wave-induced topographic change in artificial shallows composed of fine sand.
- The applicability of FSSM to the prediction of wave-induced topographic change.
- The modified sediment transport calculation considering cohesive effects.
- The cohesive influence on wave-induced topographic change in tidal flat structures composed of mixed soil.

1.4 Study Contents

The present dissertation includes six-chapters with this introduction. This section briefly demonstrates the respective contents of the chapters.

Chapter 2 demonstrates the experimental results as regards the wave-induced topographic change in artificial shallows composed of fine sand. The trends of topographic change with various wave conditions are demonstrated. The characteristics of sediment transport are investigated focusing on bottom flow velocities on the surface of the shallows and pore-water pressure variations in the surface layer of the shallows. The relative vertical effective normal stress ratio calculated from the measured pore-water pressure data and the singed Shields parameter derived from the data of bottom flow velocity are introduced for analyzing sediment transport. The study implemented in Chap. 2 was published in the Coastal Engineering Journal of JSCE in 2014.

In Chap. 3, the predictive capability of the FSSM on wave-induced topographic change is examined with the computational domain based on the experiments in Chap. 2. Despite of the confirmation of the effects of pore-water pressure in a previous chapter, the computational analysis is implemented focusing on the possibility of varied experimental conditions during experimental time due to the fine sand which is substantially sensitive to somewhat variations leading to different trend to topographic change. The numerical results comparing with experimental data are investigated in that topographic change, still water level variation and pore-water pressure at experimental time $t = 1$ min. The contents were included in the treatise published in the Journal of Advanced Simulation in Science and Engineering (JASSE) in 2014.

In Chap. 4, a modified sediment transport calculation considering cohesive force based on the FSSM is introduced to manage the non-cohesive and cohesive sediment mixtures. Among numerous factors having effects on sediment transport system in the property of cohesive sediments, physical factors such as cohesive resistance force per unit surface area, the content ratio of mud and water content are considered and incorporated into the sediment transport module in the FSSM. The characteristics of the modified calculation are described based on the relationship between non-dimensional bed load sediment transport rates versus Shields parameters. Additionally, numerical simulations based on the same numerical domain in Chap. 3 are carried out assuming the shallows containing a small quantity of cohesive sediments and the sensitivity of the modified calculation and the effects of cohesive sediments on topographic change are investigated. The contents in Chap. 4 were

published in the Journal of Korean Society of Coastal and Ocean Engineers (KSCOPE) in 2013.

Chapter 5 describes the results of experimental investigations of sediment transport and wave-induced topographic change exposed to steady flow in an open channel and regular waves in a wave flume with a tidal flat structure in mixed soil condition. The cohesive sediments are employed by kaolin in both experiments. The results in topographic change are noted and the degree of cohesive effects on topographic change is compared with the impacts of steel slag on it based on different mechanism of increasing resistance of erosion in the open channel experiments. In wave flume experiments, the author gives attention to the trend of final topographic changes under wave conditions and the influence of cohesive sediments on topographic change. Evaluation of sediment transport on the surface of the tidal flat is implemented based on the measured bottom velocities by applying modified critical Shields parameters considering cohesive effects illustrated in Chap. 4. Lastly, the applicability of the FSSM incorporating the modified sediment transport model considering cohesive effects is examined based on the results of water level elevation and topographic change in the wave flume experiments. These contents in Chap. 5 were published in the Journal of Japan Society of Civil Engineers, Series B3 (Ocean Engineering), in 2014.

In Chap. 6, an overview of the main conclusions in the present study is described. The perspectives and recommendations for future extensions are also presented.

Chapter 2

WAVE-INDUCED TOPOGRAPHIC CHANGE IN AN ARTIFICIAL SHALLOWS

2.1 General

Deeper and wider channels and berths are required for mass marine transportation. Dredging work for maintaining them produces large volumes of dredged sand. However, the volumes of dredged sand that can be used for landfill are becoming limited, and designated areas available for disposing the dredged sand have reduced. To address this issue, it is necessary to use such dredged sand in a range of innovative ways.

The construction of artificial shallows and tidal flats is attracting attention as a way to effectively use dredged sand. Here, according to Nakamura and Ishikawa (2007), a shallow area which appears above the water level at low tide is called a tidal flat. Over the last decade, studies on such artificial shallows and tidal flats were carried out from an environmental point of view. Kazama *et al.* (2006) conducted field surveys at artificial shallows and tidal flats in Mikawa Bay, Japan, and confirmed the possibility of using dredged sand in beneficial ways for coastal environments such as increasing bottom living and recovering self-purification capacity. Although the construction of artificial shallows and tidal flats contributes not only to the effective use of dredged sand but also the improvement of marine environments, shallows and tidal flats composed of dredged sand is vulnerable to approaching waves in energetic marine environments because the relatively fine sediments in dredged sand. Accordingly, studies on the characteristics of the wave-

induced topographic change in artificial shallows and tidal flats composed of fine sediments have been carried out experimentally and numerically (Kang *et al.*, 2000; Nakamura *et al.*, 2011). Furthermore, it has been pointed out that the effects of pore-water pressure need to be taken into account when evaluating the transport of such fine sediments. Zen and Yamazaki (1990) found that wave-induced fluctuation of excess pore-water pressure caused repetitive liquefaction and densification near the surface layer of the seabed. Takahashi *et al.* (1997) pointed out from large-scale hydraulic experiments that upward seepage flow induced by the upward gradient of pore-water pressure loosened the seabed, thus resulting in liquefaction. Sakai *et al.* (2002) found that the additional lift force generated by the upward gradient of pore-water pressure increased the sediment transport rate in horizontal axes on seabed under unidirectional flow. Sumer *et al.* (2011) confirmed that superficial sediment particles experienced such an upward gradient force, which was caused by the phase lag of pore-water pressure generated during the rundown and hydraulic jump stages, and the magnitude of this force reached certain values as much as about 30% of the submerged weight of particles. Furthermore, they also revealed that topographic change in a uniform sloping beach is possible to be accounted by bottom shear stress and pressure gradient force. In particular, such effects of pore-water pressure for tsunamis were considered as essential factors in sediment transport relevant to topographic change (Tonkin *et al.*, 2003; Nakamura *et al.*, 2008). Therefore, the consideration of pore-water pressure effects is suggested in studies on wave-induced topographic change such as artificial shallows composed of dredged sand due to low weight.

To address these issues, this study is devoted to experimentally investigating the characteristics of wave-induced topographic change in artificial shallows composed of fine sand focusing on not only bottom flow velocity on its surface but pore-water pressure on the surface layer of the shallows. This chapter is organized as follows. In Section 2.2, experimental setup and hydraulic conditions of experiments is described in detail. In Section 2.3, the characteristics of topographic change in the shallows are discussed surrounding wave fields. Subsequently, the effects of pore-water pressure are examined in terms of the relationship with the Shields parameter with an expression of a function of bottom flow velocity. The tendency of the sediment transport is then investigated using a modified Shields parameter that considers the

effects of the pore-water pressure. Finally, main conclusions are summarized in Section 2.4.

2.2 Hydraulic Experiments

A series of hydraulic experiments were carried out using a 25-m-long, 2.22-m-wide, and 1-m-deep wave flume with a piston-type wave generator. **Figure 2.1** shows a schematic of an experimental setup. As shown in **Fig. 2.1**, shallows composed of fine sand were laid on a horizontal impermeable flat bed. Here, the dimensions of the shallows (height: 0.20 m; crown width: 2.0 m; seaward slope: 1/20) were determined by the dimension of actual artificial shallows composed of dredged sand constructed in Mikawa Bay, Japan under the “Sea Blue Project” based on the Froude similarity rule with a length scale of 1/20. Note that a 0.20-m-high vertical impermeable wall was fixed behind the shallows because the surface profile of shallows exhibited little change on its landward slope (Nakamura *et al.*, 2011). Water level fluctuations at cross-shore locations of $x = -4.8, -1.0, 1.8, 3.6, 4.2,$ and 4.8 m were obtained using six capacitance-type wave gauges (KENEK: CHT6-40). To measure pore-water pressure on the surface layer of the shallows, eight pore-water pressure transducers (Kyowa: BP-500GRS, BPR-A-50KPS), which were equipped stainless porous filters on their pressure-sensing surface to remove soil pressure change, were installed at the same positions as the wave gauges. In addition, bottom flow velocity at 0.01 m away from the surface of the shallows was measured using an electromagnetic velocimeter (KENEK: VMT2-200-04PL).

Regular waves with two patterns of wave heights H_i ($= 0.025$ and 0.065 m) and wave periods T ($= 1.0$ and 1.6 s) were generated at two different still water depths h

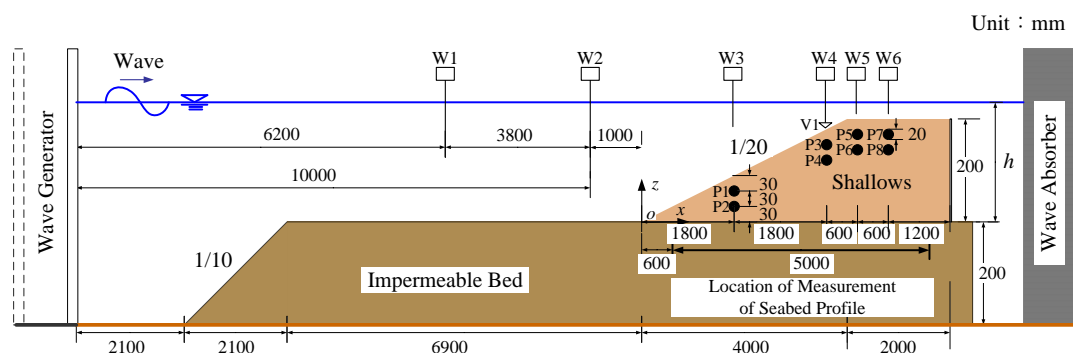


Fig. 2.1 Schematic of the experimental setup (W1-W6: wave gauge, P1-P8: pore-water pressure transducer, V1: velocimeter).

Table 2.1 Experimental conditions.

Case	h [m]	H_i [m]	T [s]	d_{50} [mm]
1	0.275	0.025	1.0	0.1
2		0.065		
3	0.225	0.025		
4		0.065		
5	0.275	0.065	1.6	0.1
6	0.225			
7	0.275	0.065	1.0	0.2
8	0.225			

(= 0.225 and 0.275 m), for which the value of H_i was defined as the incident wave height at the most distance measurement point from the shallows, *i.e.*, W1 with the scale of 1:20 (see **Fig. 2.1**). For $H_i = 0.065$ m and $T = 1.0$ s, the median grain size of the sand composing the shallows d_{50} was changed to 0.1 and 0.2 mm. Noted that although the coarser sand than the sediments accurately modeled by the Froude similarity rule was used in this study ($d_{50} = 0.30$ and 1.42 mm in prototype), two sizes of the fine sand ($d_{50} = 0.1$ and 0.2 mm) were appropriated to investigate the mechanism of the topographic change in the shallows composed of fine sand because finer sediments showed cohesive characteristics. Hydraulic conditions in experiments were adopted based on in-situ conditions. In the prototype, incident wave height is 1.3 m and wave period is 5.1 s corresponding to 1 year probability waves, which were employed in the experiments. Water level was based on the water depth on the crown of shallows when mean water level (MWL), 5.5 m, and low water level (LWL), 4.5 m.

As above mentioned, the stability of dredged sand structures is targeted. However, in this section, the behavior of non-cohesive sediment in dredged sand is focused to understand sediment transport characteristics of very fine sand. A total of eight experimental cases were implemented as summarized in **Table 1**. Once the set of the initial shallow structure was accomplished, each experimental run was implemented with the following steps.

1. The initial surface profile of the shallows was measured in the range from $x = 0.6$ m to $x = 5.6$ m using a surface profiler (Masatoyo Engineering: MT-E.P.I-2) and a potentiometer (Kyowa: DTP-D-5KS).

2. The specific waves were generated for 1 min. Water surface elevations, pore-water pressures, and bottom flow velocity were measured and recorded at the sampling frequency of 100 Hz in a personal computer, simultaneously.
3. The wave generating was ceased and the developed surface profile of the shallows during experimental time was measured.
4. The waves were generated again for 9 min (*i.e.*, the total elapsed time $t_e = 10$ min). Similar to the step 2, water surface elevations, pore-water pressures, and bottom flow velocity were measured and recorded for 1 min after resuming and before ceasing the wave generating.
5. Step 3 and 4 was iterated for $t_e = 30, 60,$ and 300 min.

In preliminary runs, it was observed that the topographic change including the formulation of ripples was practically uniform in the longitudinal direction of the shallows. Therefore, the surface profile of the shallows was measured along the centerline of the flume.

2.3 Results and Discussion

2.3.1 Topographic change in the shallows

Figure 2.2 shows the surface profile of the shallows z at $t_e = 0, 30,$ and 60 min. **Figures 2.3** and **2.4** show the topographic change in the shallows Δz and the sediment transport rate per unit long-shore length q for $0 \leq t_e \leq 30$ min and $30 \leq t_e \leq 60$ min, in which the positive values of Δz and q indicate the deposition and landward sediment transport. Here, the value of q was calculated based on the following mass conservation equation of the sand on the assumption of $q \approx 0$ at $x = 0.6$ m:

$$(1-m) \frac{\partial z}{\partial t} + \frac{\partial q}{\partial x} = 0, \quad (2.1)$$

because it was observed that the topographic change at $x = 0.6$ m was as small as 5.8 mm at a maximum value of Δz after the completion of the wave generating ($t_e = 300$ min) except for Case 6, which will be explained later. In Eq. (2.1), m is the porosity of the sand ($= 0.4$) and t is the time.

In Case 3, **Figs. 2.2(a)** and **2.3(a)** show that small-scale erosion was formed at the upper part of the slope ($3.3 \leq x \leq 3.9$ m), and smaller-scale deposition was formed

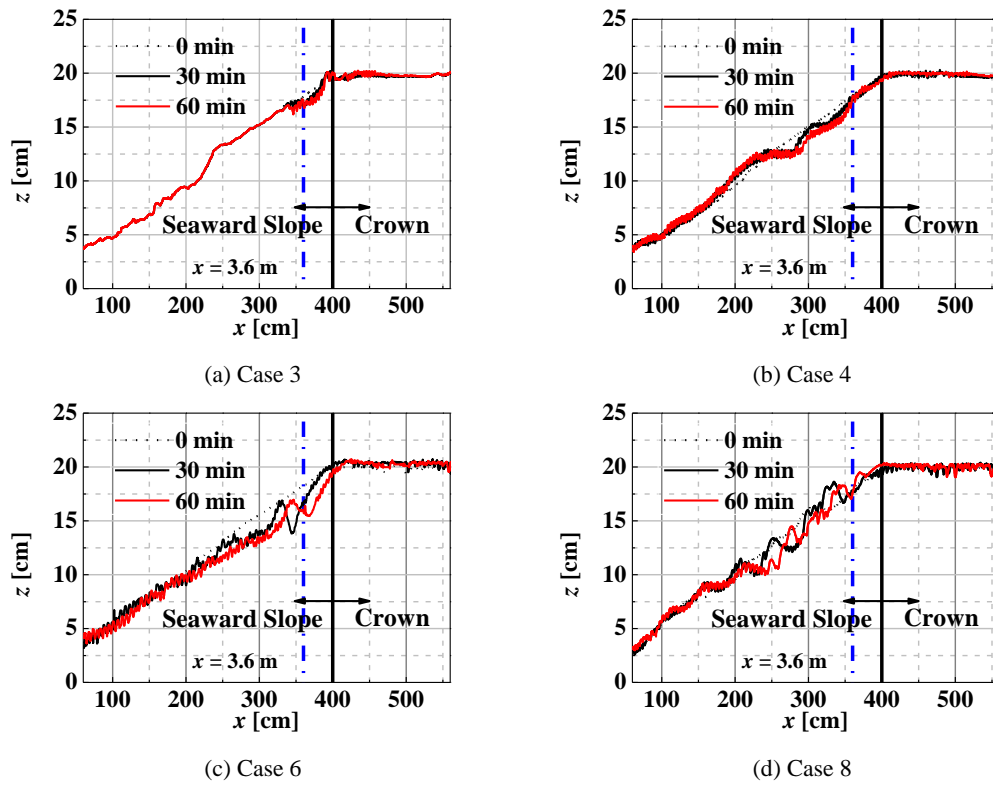


Fig. 2.2 Surface profile of the shallows z at $t_e = 0, 30$ and 60 min.

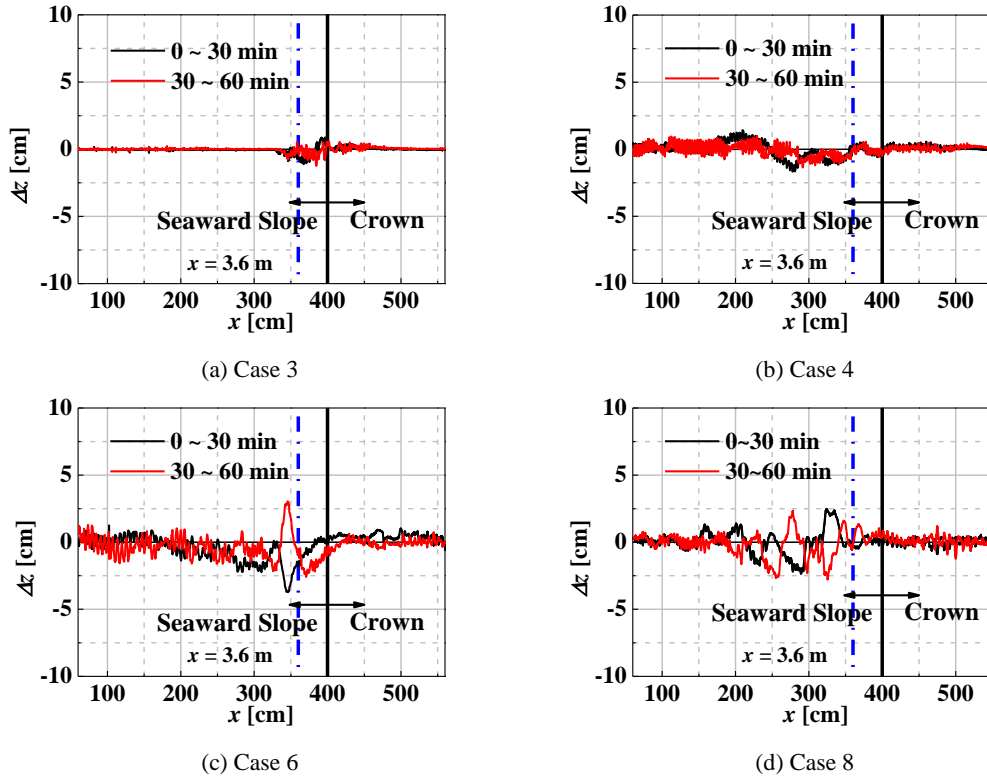


Fig. 2.3 Topographic changes in the shallows Δz for $0 \leq t_e \leq 30$ min and $30 \leq t_e \leq 60$ min.

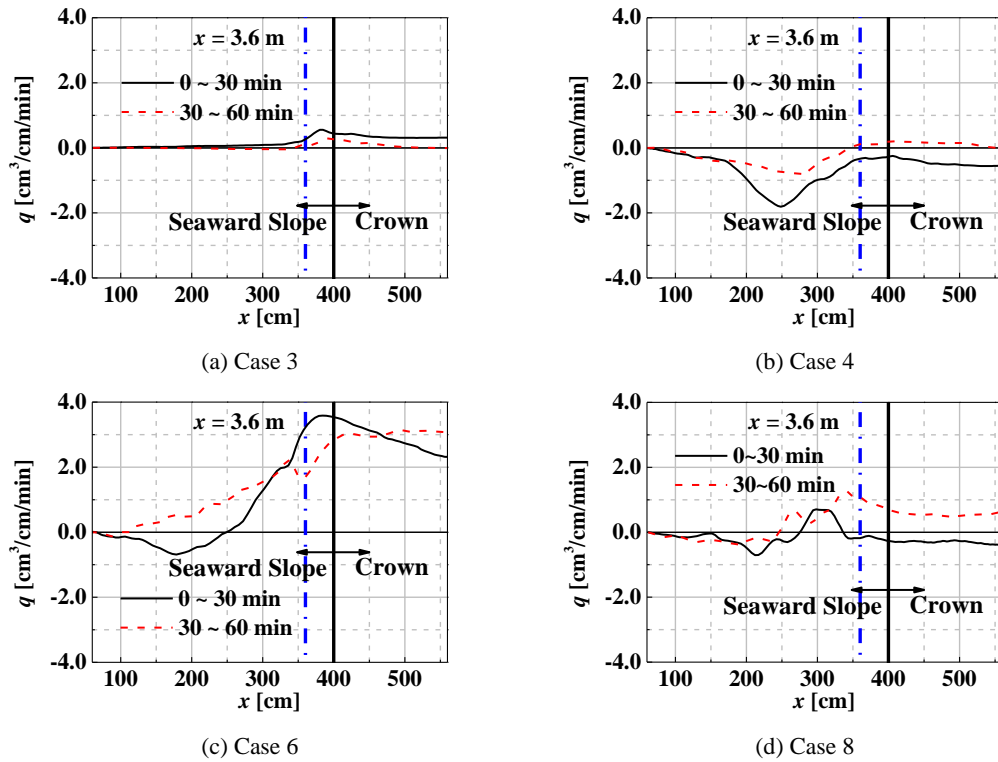


Fig. 2.4 Sediment transport rate q for $0 \leq t_e \leq 30$ min and $30 \leq t_e \leq 60$ min.

at the landward side of the erosion. Accordingly, as indicated in **Fig. 2.4(a)**, q had a small positive value, *i.e.*, little sediment transport occurred in the seaward direction. In Case 4, **Figs. 2.2(b)** and **2.3(b)** show the formation of deposition on the lower part of the slope ($1.7 \leq x \leq 2.3$ m) and erosion on the upper part of the slope ($2.3 \leq x \leq 3.6$ m). As shown in **Fig. 2.4(b)**, seaward sediment transport occurred unlike in Case 3. In Case 6, **Figs. 2.2(c)** and **2.3(c)** show that erosion took place over a wide area of the slope ($1.5 \leq x \leq 4.0$ m) different from the results for Cases 3 and 4 due to the effect of longer wave length. In this case, it was also observed from visual observation in the hydraulic experiments that deposition had already occurred at $t_e = 10$ min at the seaward side of $x < 0.6$ m where the surface profile of the shallows was inaccessible because of the limitations of the apparatus. Specifically, the topographic change Δz at $x = 0.6$ m after the completion of the wave generating ($t_e = 300$ min) was 28.2 mm, which was more than four times larger than that in the other cases. The deposition at the seaward side at $x = 0.6$ m means $q < 0$ at $x = 0.6$ m dissimilar to the assumption of $q \approx 0$, and consequently the value of q in the landward direction was presumably overestimated due to non-consideration of the deposited area in q as shown in **Fig. 2.4(c)**. In Case 8, it was observed in **Figs. 2.2(d)** and **2.3(d)**

that erosion and deposition took place sequentially over a wide range of the slope ($1.5 \leq x \leq 3.8$ m), and their locations moved with time. Thus, **Fig. 2.4(d)** also shows that the direction of the sediment transport varied with time and location.

Figure 2.5 shows the initial and final surface profiles of the shallows z , the topographic change in the shallows Δz , and the sediment transport rate per unit long-shore length q after the completion of the wave generating ($t_e = 300$ min). In **Fig. 2.5**, the spatial distribution of the non-dimensional wave height H/H_i and the non-dimensional mean water level $\bar{\eta}/H_i$ are presented together. Here, the values of H/H_i and $\bar{\eta}/H_i$ were calculated from experimental data during three wave periods early after the initiation of wave generating.

From a comparison between **Figs. 2.5(a)** and **(b)** with different incident wave heights H_i , it was found that the area of the topographic change became large with an

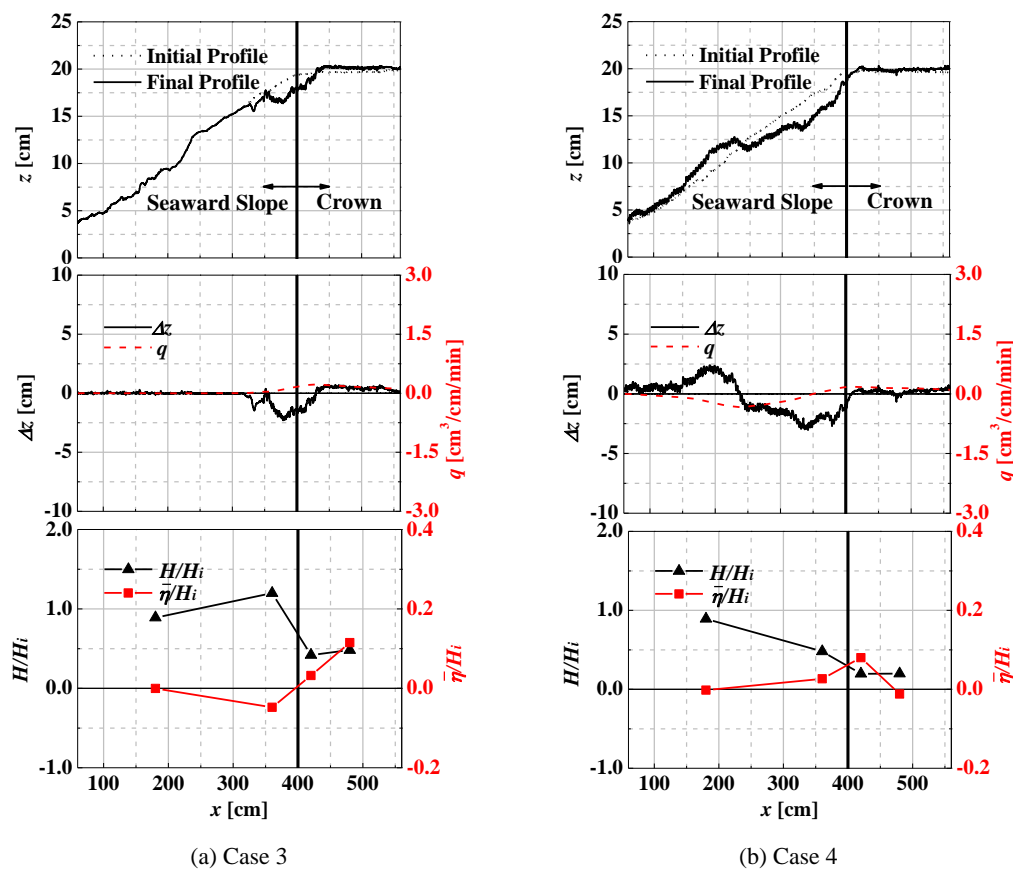


Fig. 2.5 Topographic changes in the shallows after the completion of wave generating for the still water depth $h = 0.225$ m (upper figure: the initial and final surface profiles of the shallows z ; middle figure: the topographic change in the shallows Δz and the sediment transport rate q ; lower figure: the non-dimensional wave height H/H_i and the non-dimensional mean water level $\bar{\eta}/H_i$).

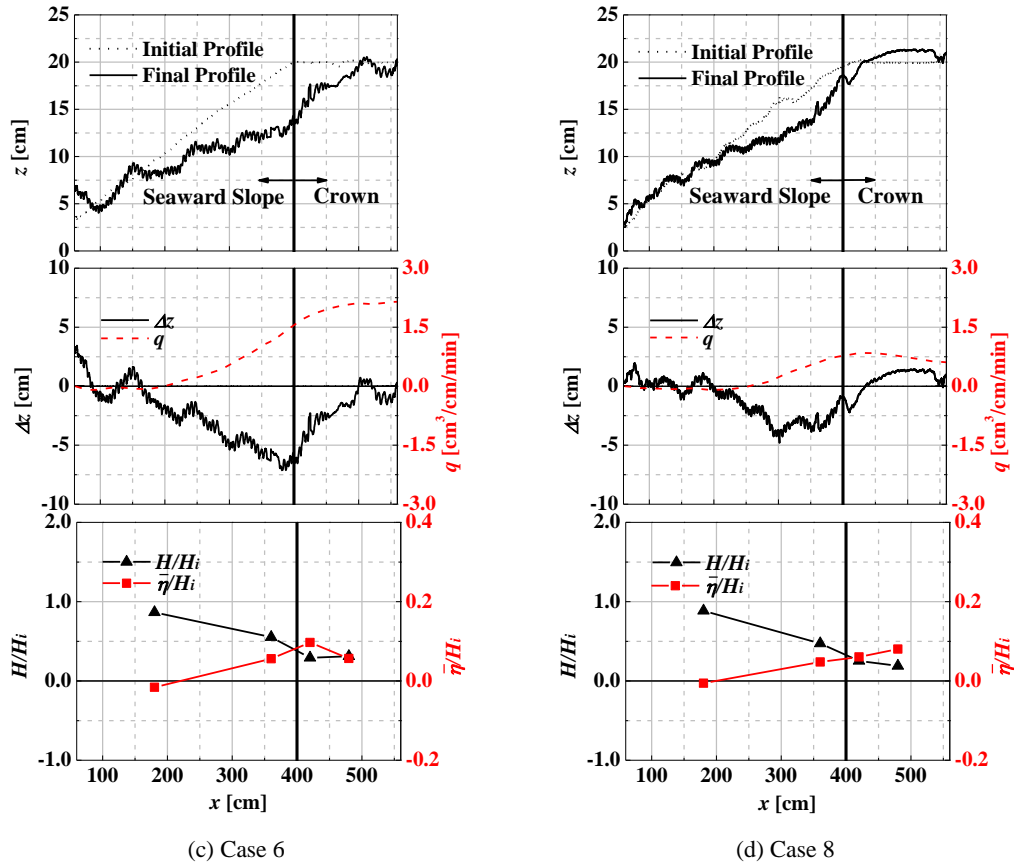


Fig. 2.5 (Continued).

increase in H_i . In **Figs. 2.5(b)** and **(c)** with different wave periods T , it was observed that although the degree of the topographic change became large with an increase in T , the trends seemed to be similar. In contrast, **Figs. 2.5(b)** and **(d)** with different median grain sizes of the sand d_{50} show a different trend in z and Δz . In particular, the deposition in **Fig. 2.5(d)** was formed not on the lower part of the slope as in **Fig. 2.5(b)**, but on the crown of the shallows.

As for H/H_i and $\bar{\eta}/H_i$, **Fig. 2.5(a)** shows that $\bar{\eta}/H_i$ decreased with an increase in H/H_i , and reached the minimum value at the upper part of the slope. At its landward side where on the crown of the shallows, peculiar results were shown that conversely $\bar{\eta}/H_i$ increased with a decrease in H/H_i . Dissimilar to **Fig. 2.5(a)**, **Figs. 2.5(b)–(d)** indicate that $\bar{\eta}/H_i$ continued to decrease with an increase in H/H_i across the all measured positions on the shallows. These phenomena have relevance to wave breaking. The position of the wave breaking corresponded to the location near the minimum $\bar{\eta}/H_i$ in visual observations of the experiments. The respective wave

Table 2.2. C_s values.

Case	C_s	h [m]
1	4.90	0.275
2	12.40	0.275
3	5.16	0.225
4	12.40	0.225
5	11.40	0.275
6	12.40	0.225
7	7.94	0.275
8	7.88	0.225

breaking positions are expected at near $x = 3.6$ m for Case 3 and between $x = 1.8$ - 3.6 m for Case 4, 6 and 8. Furthermore, the magnitude of the wave breaking seemed to depend on the incident wave height H_i and the wave period T . This result suggests that, as mentioned earlier, the area and scale of the topographic change in the shallows grow with an increase in H_i and T .

The C_s value proposed by Sunamura and Horikawa (1974) is generally used when evaluating the equilibrium surface profile of a uniform sloping beach, which is calculated from

$$C_s = \frac{H_o}{L_o} (\tan \beta)^{0.27} \left(\frac{d_{50}}{L_o} \right)^{-0.67}, \quad (2.2)$$

in which H_o is the offshore wave height, L_o is the offshore wave length, and β is the angle of the sloping beach. According to the value of C_s , the tendency of topographic change in a beach is classified into the following three types: the erosion type when $C_s \geq 8$, in which a shoreline retrogresses and sand piles up in offshore region; the transitional type when $4 < C_s < 8$, in which a shoreline advances and sand accumulates offshore; and the deposition type when $C_s \leq 4$, in which a shoreline proceeds and no sand deposition occurs offshore. The C_s value has been proposed for a uniform sloping beach, and accordingly the experimental conditions of this study are beyond its scope because of the existence of the crown. However, the value of C_s in each experimental case was calculated as shown in **Table 2.2** and examined by the relationship with the topographic change in the shallows. In calculating these C_s values, the incident wave height H_i , its wavelength L_i , and the seaward slope of the shallows ($= 1/20$) were substituted into H_o , L_o , and β respectively in Eq. (2.2). For the low still water depth $h = 0.225$ m, as indicated in **Table 2.2** and **Fig. 2.5**, the

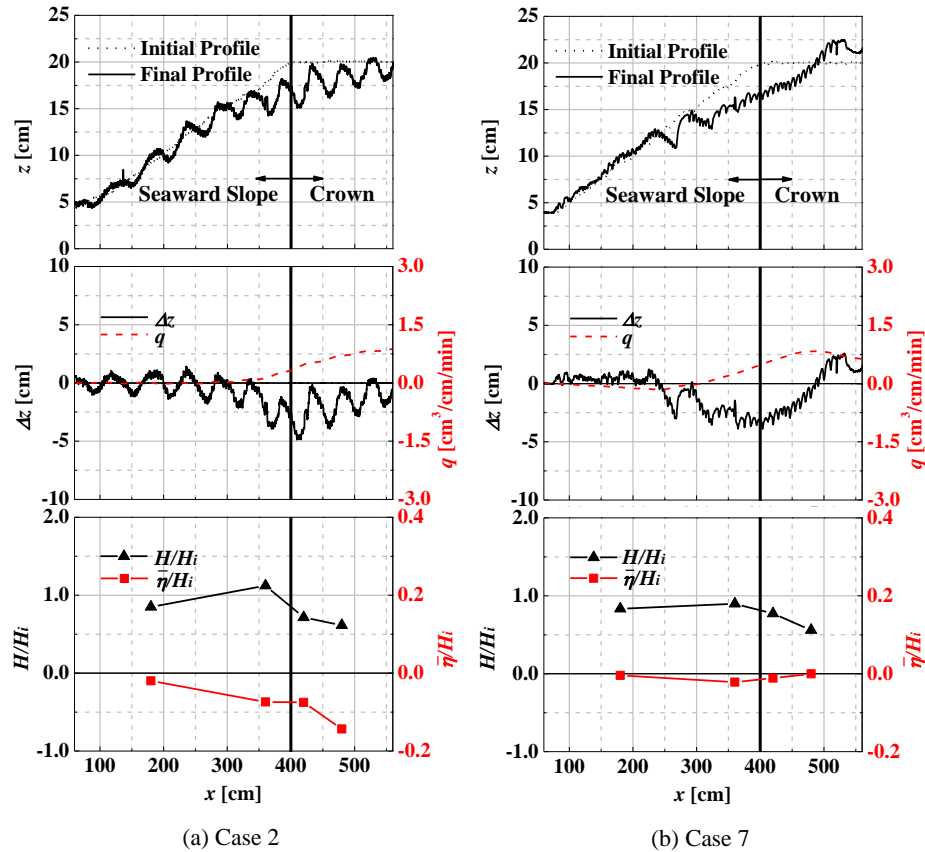


Fig. 2.6 Topographic changes in the shallows after the completion of wave generation for the still water depth $h = 0.275$ m (upper figure: the initial and final surface profiles of the shallows z ; middle figure: the topographic change in the shallows Δz and the sediment transport rate q ; lower figure: the non-dimensional wave height H/H_i and the non-dimensional mean water level $\bar{\eta}/H_i$).

topographic change in the shallows showed the characteristics of the erosion type for the value of C_s was relatively large (Cases 4 and 6). In contrast, such a trend was not confirmed when the value of C_s was small (Cases 3 and 8). In representative cases for the deeper still water depth $h = 0.275$ m, the initial and final surface profiles of the shallows z , the topographic change in the shallows Δz , and the sediment transport rate per unit long-shore length q after the completion of the wave generation ($t_e = 300$ min) as well as the non-dimensional wave height H/H_i and the non-dimensional mean water level $\bar{\eta}/H_i$ during three wave periods early after the initiation of wave generation are shown in **Fig. 2.6**. From **Table 2.2** and **Fig. 2.6**, the characteristics of the erosion type were not observed even when the value of C_s was relatively large. These results imply that the possibility to evaluate the trend of the topographic change in the shallows using the C_s value is confirmed when the shallows can be considered as a uniform sloping beach due to the shallow water depth on its crown.

2.3.2 Influences of bottom flow velocity and pore-water pressure

To examine the relationship between the topographic change in the shallows and bottom flow velocity on its surface, a signed Shields parameter defined as positive landward φ_d was calculated from:

$$\varphi_d = \frac{u_* |u_*|}{(\rho_s / \rho_w - 1) g d_{50}}, \quad (2.3)$$

in which u_* is the friction velocity defined as positive landward, ρ_s is the density of sand particles ($= 2.65 \times 10^3 \text{ kg/m}^3$), ρ_w is the density of water ($= 1.00 \times 10^3 \text{ kg/m}^3$), and g is the gravitational acceleration ($= 9.80 \text{ m/s}^2$). Here, instantaneous values of the Shields parameter calculated from each experimental case were adopted because ensemble-averaged values of the Shields parameter were unavailable due to the lack of multiple experimental data under the same condition. Defining the Kármán constant as $\kappa (= 0.4)$, the equivalent sand roughness as $k_s (= 2.5d_{50})$, the height of the velocimeter from the surface of the shallows as z_h , and the empirical constant as $B_s (= 8.5)$, the value of u_* can be estimated by the following equation:

$$\frac{u_t}{u_*} = \frac{1}{\kappa} \ln \frac{z_h}{k_s} + B_s, \quad (2.4)$$

in which the value of u_t was calculated from the bottom flow velocity measured at V1 and the local slope angle, *i.e.*, at the position of $x = 3.6 \text{ m}$ (see **Fig. 2.1**). Furthermore, because the surface of the shallows was not horizontal at $x = 3.6 \text{ m}$, the absolute values of the landward and seaward critical Shields parameters φ_c' were determined to be 0.057 and 0.043 using the following equation (Kawata, 1989):

$$|\varphi_c'| = \varphi_c \left\{ \cos \beta \pm \frac{\rho_s / \rho_w}{(\rho_s / \rho_w - 1) \sin \beta / \tan \phi} \right\}, \quad (2.5)$$

in which the sign of + and – corresponds to the landward and seaward directions, φ_c is the critical Shields parameter on a horizontal flat surface ($= 0.05$), and ϕ is the repose angle of submerged sand particles ($= 29^\circ$).

Figure 2.7 shows the temporal change in φ_d for 25 wave periods early after the initiation of the wave generation, in which the horizontal broken lines indicate the

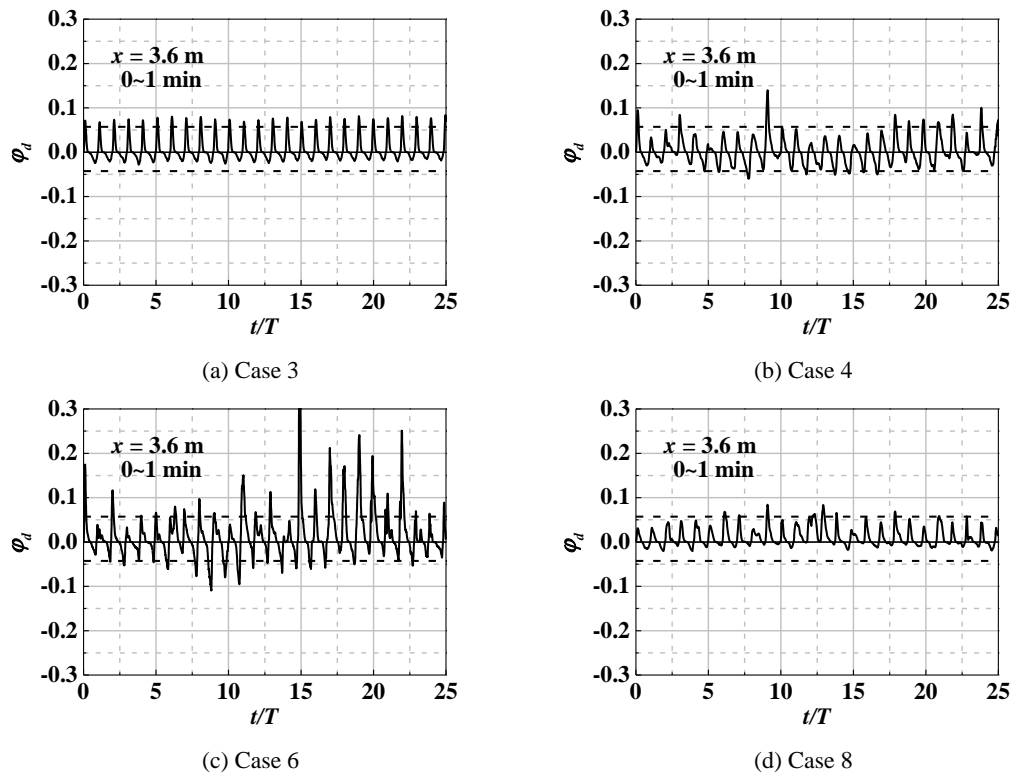


Fig. 2.7 Temporal change in the signed Shields parameter φ_d at $x = 3.6$ m early after the initiation of the wave generating.

critical Shields parameters. In Case 3, **Fig. 2.7(a)** shows that the value of φ_d periodically slightly exceeded only the landward critical Shields parameter, which was consistent with the occurrence of the small positive q at $x = 3.6$ m for $0 \leq t_e \leq 30$ min (see **Fig. 2.4(a)**). In Case 6, **Fig. 2.7(c)** shows that the value of φ_d fluctuated considerably, and many signed Shields parameters are above the landward critical Shields parameter compared with the seaward one. The results of the direction of φ_d exceeding the critical Shields parameter corresponded to the results of q (see **Fig. 2.4(c)**). In Case 8, as can be seen in **Fig. 2.7(d)**, the value of φ_d hardly exceeded the critical Shields parameters because its fluctuation was smaller than that in Case 3. Consequently, as shown in **Fig. 2.4(d)**, little sediment transport occurred at $x = 3.6$ m for $0 \leq t_e \leq 30$ min. In contrast, a different trend between φ_d and q was observed in Case 4. Specifically, **Fig. 2.7(b)** shows that the value of φ_d intermittently exceeded the landward critical Shields parameter, whereas **Fig. 2.4(b)** shows that sediment transport occurred in the opposite direction, seaward, different from the trend of φ_d . These results suggest that the value of φ_d is insufficient to explain the trend of q . Note that the sediment transport for $0 \leq t_e \leq 30$ min was discussed in this study using the

temporal change in φ_d for the first 25 wave periods due to the lack of the experimental data after $t_e = 1$ min.

For the appropriate evaluation of q , the effects of pore-water pressure and the relationship with φ_d were examined using the vertical effective normal stress σ' at the same position as φ_d , which was estimated using the following equation (Zen and Yamazaki, 1990):

$$\sigma' = (\rho_t - \rho_w)gz_d + (p_b - p), \quad (2.6)$$

in which ρ_t is the density of saturated sand particles ($= 1.99 \times 10^3 \text{ kg/m}^3$), p_b is the water pressure on the surface of the shallows, and p is the pore-water pressure at a depth of z_d from the surface of the shallows. Assuming that the amplitude of pore-water pressure decreased exponentially in the downward direction, the value of p_b was extrapolated from pore-water pressures measured at P3 and P4. To focus on σ' near the surface of the shallows, the pore-water pressure measured at P3 was used as p . From the estimated value of σ' , the relative vertical effective normal stress ratio γ was calculated from:

$$\gamma = \frac{\sigma'_0 - \sigma'}{\sigma'_0}, \quad (2.7)$$

in which σ'_0 represents the initial value of σ' . Note that the γ value is one of the non-dimensional indices for evaluating sand liquefaction, with liquefaction occurring when $\gamma = 1$.

Figure 2.8 shows the relationship between φ_d and γ for the first 1 min, *i.e.*, $0 \leq t_e \leq 1$ min, in which the vertical broken lines represent the landward and seaward critical Shields parameters, and the horizontal dotted line means the occurrence of liquefaction ($\gamma = 1$).

For $d_{50} = 0.1$ mm, as can be seen in **Figs. 2.8(a)–(c)**, γ was negatively correlated with φ_d . The temporal change in φ_d and γ for the corresponding cases to **Figs. 2.8(a)–(c)** is shown in **Fig. 2.9**. From **Fig. 2.9**, it was found that γ had the phase opposite to φ_d . This result was also observed by Miura *et al.* (2010) and they defined this phenomenon as phase lag. Consequently, it was demonstrated that the phase lag caused the negative correlation between φ_d and γ . In addition, **Figs. 2.8(a)–(c)**

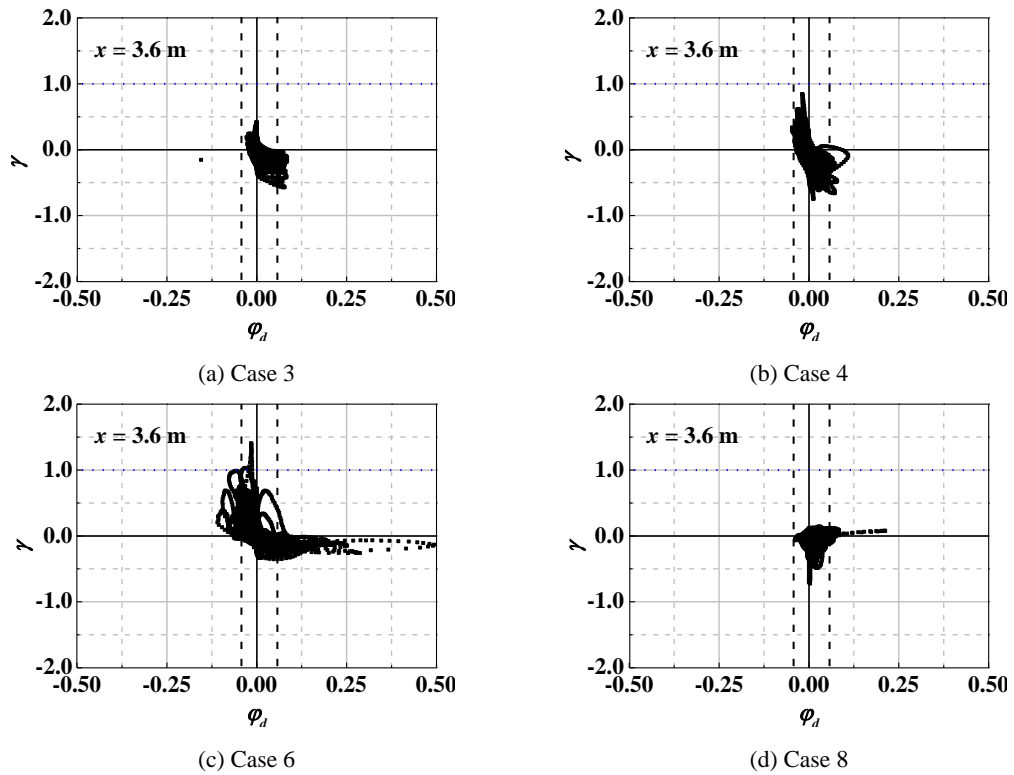


Fig. 2.8 Relationship between the signed Shields parameter φ_d and the relative vertical effective normal stress ratio γ at $x = 3.6$ m for the first 1 min.

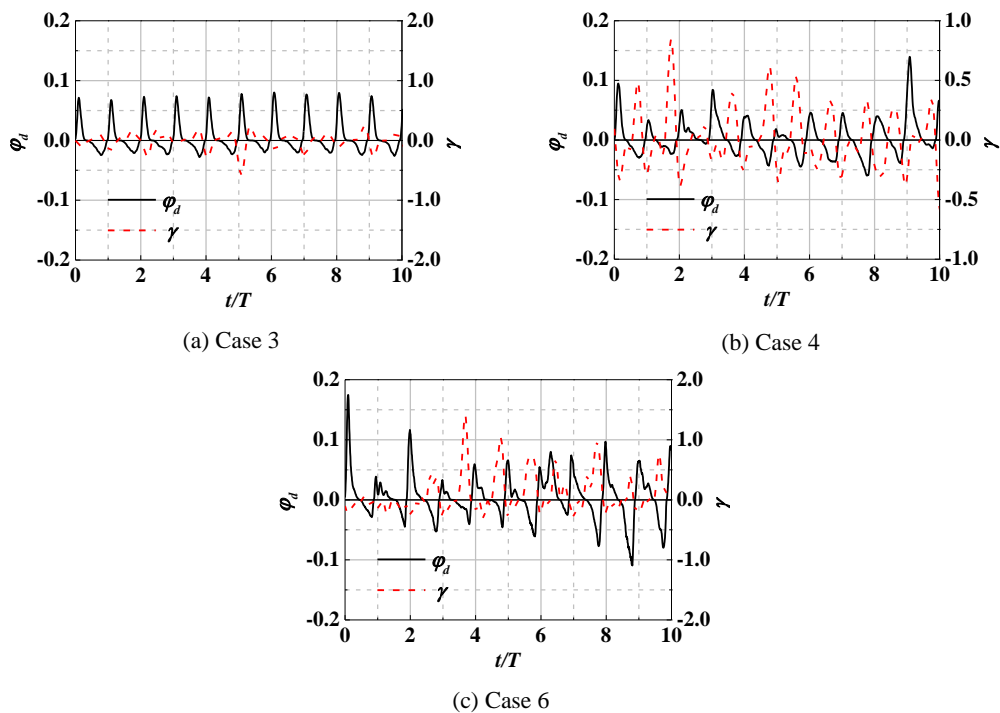


Fig. 2.9 Temporal change in the signed Shields parameter φ_d and the relative vertical effective normal stress ratio γ at $x = 3.6$ m early after the initiation of the wave generation.

indicate that the values of γ became negative in the phase of positive φ_d values. The result implies that landward sediment transport decreases because an increase in restricting force between sand particles is operated by a decrease in γ , *i.e.*, an increase in σ^{\prime} . In contrast, the values of γ became positive at the phase of negative φ_d values that implies accelerating sediment transport seaward. From these results, it is inferred that the sediment transport for $d_{50} = 0.1$ mm was related with φ_d and γ , *i.e.*, the bottom flow velocity and pore-water pressure. In particular, in Cases 4 and 6, the pore-water

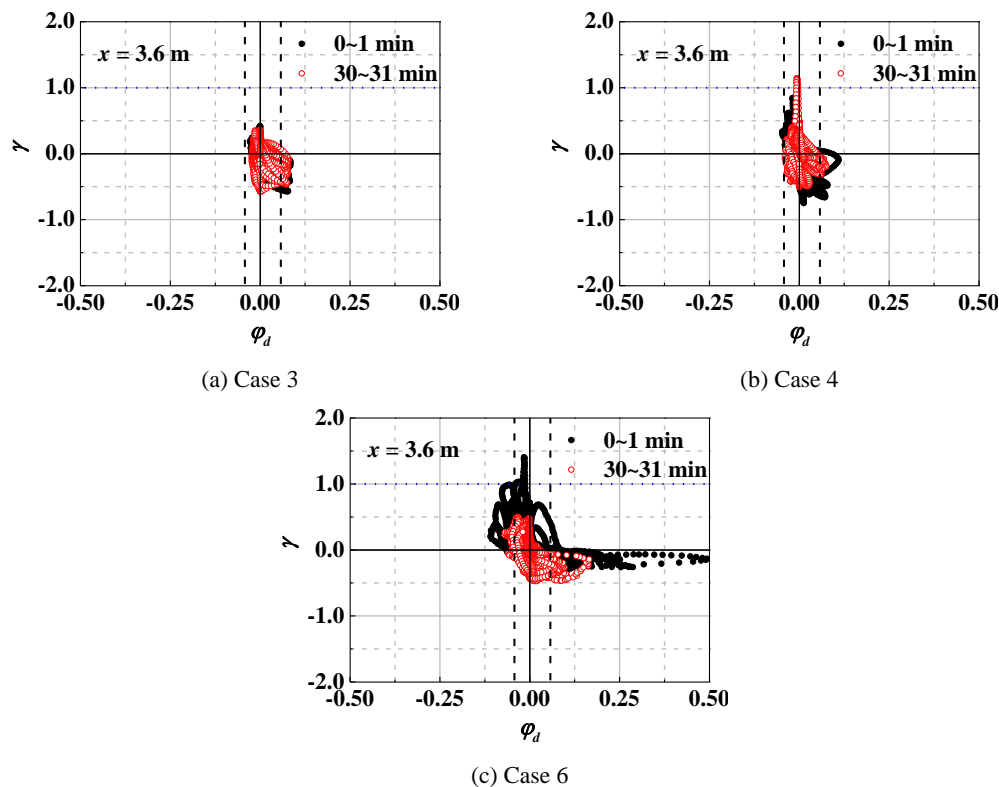


Fig. 2.10 Relationship between the signed Shields parameter φ_d and the relative vertical effective normal stress ratio γ at $x = 3.6$ m for $0 \leq t_e \leq 1$ min and $30 \leq t_e \leq 31$ min in the cases of $d_{50} = 0.1$ mm.

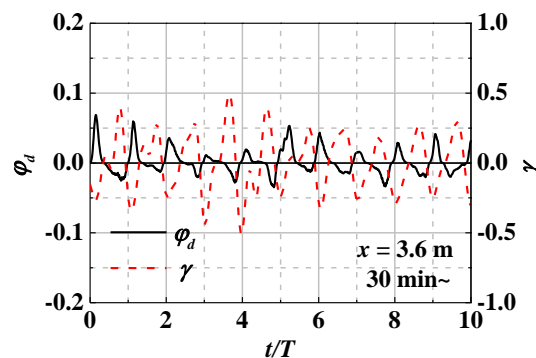


Fig. 2.11 Temporal change in the signed Shields parameter φ_d and the relative vertical effective normal stress ratio γ at $x = 3.6$ m after $t_e = 30$ min in Case 4.

pressure had a close relationship with the seaward sediment transport because γ increased close to unity, which means liquefaction, in the phase of negative φ_d values.

To investigate whether the above-mentioned relationship between φ_d and γ was observed regardless of the topographic change in the shallows, **Fig. 2.10** shows a comparison of its relationship between $0 \leq t_e \leq 1$ min and $30 \leq t_e \leq 31$ min for $d_{50} = 0.1$ mm. In Cases 3 and 4, as indicated in **Figs. 2.10(a)** and **(b)**, there was a relatively small difference in the fluctuation of φ_d and γ . This was because the topographic change in the shallows Δz at $x = 3.6$ m was small for $0 \leq t_e \leq 30$ min (see **Figs. 2.3(a)** and **(b)**). In contrast, in Case 6, **Fig. 2.10(c)** shows that the fluctuation of φ_d and γ significantly decreased with time because of the large change in Δz for $0 \leq t_e \leq 30$ min (see **Fig. 2.3(c)**). Nevertheless, it should be noted that the relationship between φ_d and γ was unchanged regardless of the value of Δz . **Figure 2.11** shows an example of the temporal change in φ_d and γ after $t_e = 30$ min in Case 4. From **Fig. 2.11**, it was observed that the phase of γ remained opposite to that of φ_d , resulting in an unchanged relationship between φ_d and γ . As a result, it is suggested that the consideration of the effects of the pore-water pressure in discussing the sediment transport is necessary regardless of the topographic change in the shallows.

Figure 2.8(d) for $d_{50} = 0.2$ mm shows a different correlation between φ_d and γ compared with the cases for $d_{50} = 0.1$ mm. The temporal change in φ_d and γ in this case is presented in **Fig. 2.12**. As shown in **Fig. 2.12**, the fluctuation of γ was almost 0 when φ_d reached near maximum and minimum. Furthermore, γ decreased when the sign of φ_d shifted from positive to negative, and vice versa. However, the absolute value of the decreased γ was smaller than that of the increased γ . Consequently, as shown in **Fig. 2.8(d)**, the shape of the relationship between φ_d and γ became an inverted triangle. From the result that little fluctuation of γ occurred near maximum and minimum φ_d , it is suggested that the pore-water pressure had little effect on the sediment transport in the case where the construction sand becomes coarse up to a median grain size of 0.2 mm in this study.

2.3.3 Modified Shields parameter considering the effects of pore-water pressure

To appropriately evaluate the trend of q , a signed Shields parameter modified to consider the gradient of pore-water pressure φ_{dm} (Sumer *et al.*, 2011) was calculated from:

$$\varphi_{dm} = \frac{u_* |u_*|}{(\rho_s / \rho_w - 1)gd_{50} - \frac{(P - P_b) / \gamma_w}{z_d} gd_{50}}, \quad (2.8)$$

in which γ_w is the unit weight of water ($= \rho_w g$). Similar to φ_d , φ_{dm} was defined as positive landward.

Figure 2.13 shows a comparison between the temporal change in φ_d and φ_{dm} for 25 wave periods early after the initiation of the wave generation, in which the horizontal broken lines indicate the critical Shields parameters. In **Fig. 2.13**, a comparison for $d_{50} = 0.2$ mm is also presented.

Of the cases for $d_{50} = 0.1$ mm, in Case 3, **Fig. 2.13(a)** indicates that the positive amplitude of φ_{dm} was slightly smaller than that of φ_d , while the negative amplitude of φ_{dm} was slightly larger than that of φ_d ; *i.e.*, the effects of the pore-water pressure changed depending on the phase because of the negative correlation between φ_d and γ , as shown in **Fig. 2.8**. Note that this is the reason why the instantaneous values of φ_d and φ_{dm} were adopted in this study to examine the effects of the pore-water pressure. However, the difference between φ_d and φ_{dm} was small, and both values slightly exceeded only the landward critical Shields parameter. From this result, it is confirmed that the change in both φ_d and φ_{dm} was consistent with the small positive q at $x = 3.6$ m for $0 \leq t_e \leq 30$ min (see **Fig. 2.4(a)**). In Case 6, **Fig. 2.13(c)** indicates that the positive amplitude of φ_{dm} was slightly smaller than that of φ_d , while the negative amplitude of φ_{dm} was instantaneously larger than that of φ_d . This is because γ increased close to unity in the phase of seaward sediment transport, and the denominator of Eq. (2.8) for calculating the value of φ_{dm} approached zero with the increase in γ . Nevertheless, the value of φ_{dm} remained unchanged and considerably exceeded the landward critical Shields parameter compared with the seaward one. In this case, the both trends of φ_{dm} and φ_d correspond to that of q (see **Fig. 2.4(c)**). In Case 4, a similar relationship between φ_d and φ_{dm} was observed in **Fig. 2.13(b)**.

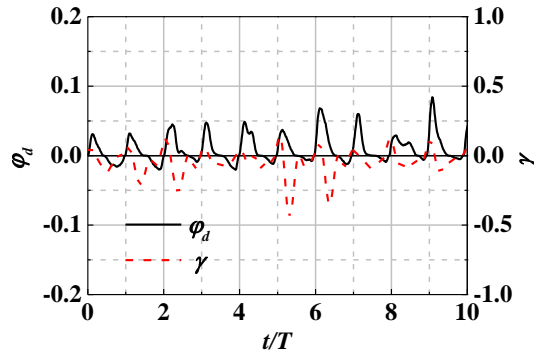


Fig. 2.12 Temporal change in the signed Shields parameter φ_d and the relative vertical effective normal stress ratio γ at $x = 3.6$ m early after the initiation of the wave generation in Case 8.

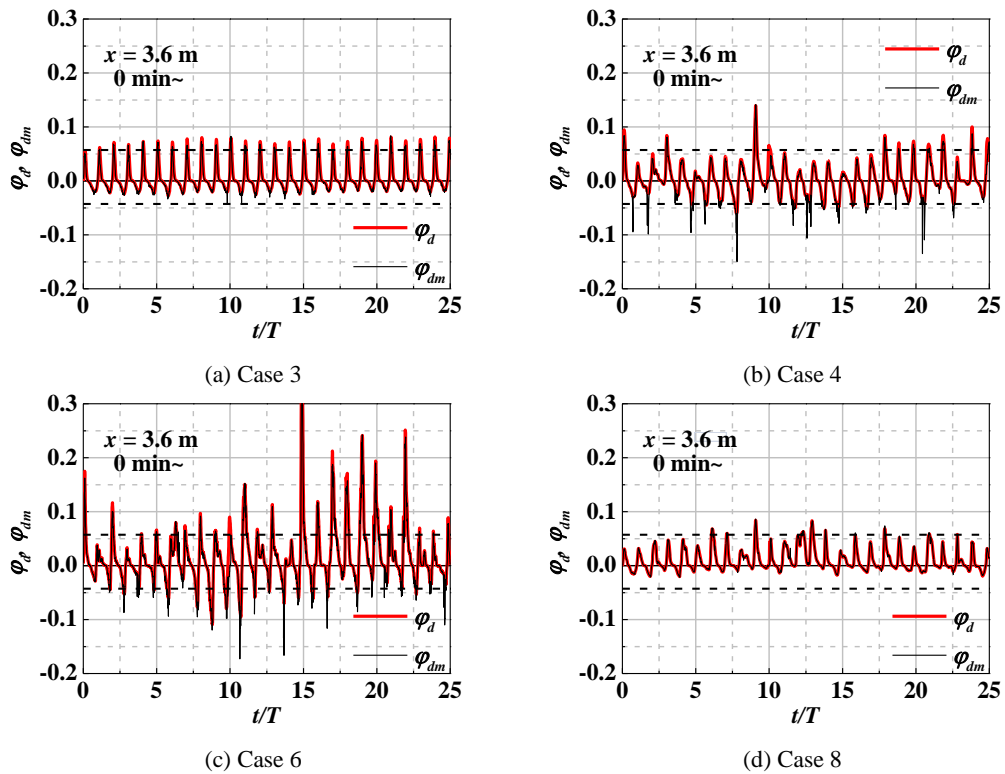


Fig. 2.13 Temporal change in the signed Shields parameter φ_d and the modified signed Shields parameter φ_{dm} at $x = 3.6$ m early after the initiation of the wave generating.

However, it was confirmed from **Fig. 2.13(b)** that the value of φ_d intermittently exceeded the landward critical Shields parameter, while that of φ_{dm} exceeded the seaward critical Shields parameter more frequently and more significantly than the landward critical Shields parameter. Consequently, it is suggested that, φ_{dm} has a reasonable correspondence with the negative q unlike φ_d (see **Fig. 2.4(b)**).

Figure 2.14 shows the temporal change in φ_d and φ_{dm} , after $t_e = 30$ min for $d_{50} = 0.1$ mm, to compare them before and after the onset of the topographic change in

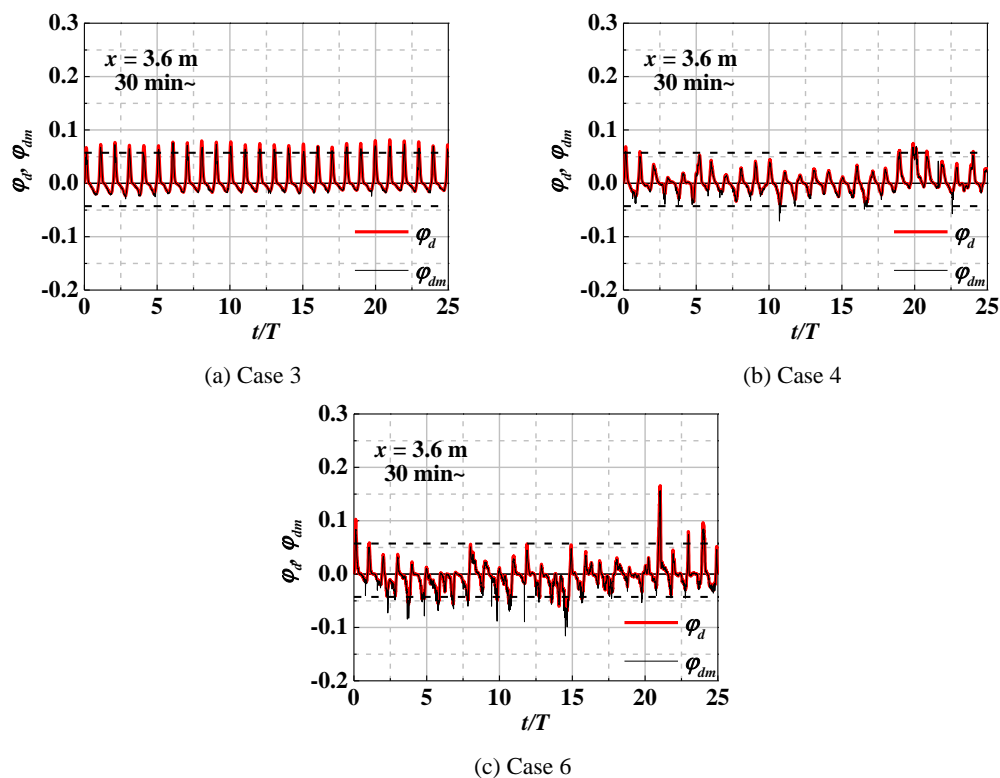


Fig. 2.14 Temporal change in the signed Shields parameter φ_d and the modified signed Shields parameter φ_{dm} at $x = 3.6$ m after $t_e = 30$ min for $d_{50} = 0.1$ mm.

the shallows. In Case 3, as mentioned in the explanation of **Fig. 2.10(a)**, a comparison between **Fig. 2.13(a)** and **Fig. 2.14(a)** shows somewhat variations with time in the fluctuation of φ_{dm} , *i.e.*, in the magnitude of φ_{dm} over the landward critical Shields parameter. This result was consistent with the result of q decreased (see **Fig. 2.4(a)**). Similar to Case 3, in Case 4, it was observed in **Figs. 2.13(b)** and **2.14(b)** that the fluctuation of φ_{dm} slightly decreased with time. As mentioned earlier, although **Fig. 2.13(b)** shows that the value of φ_{dm} largely exceeded the seaward critical Shields parameter at the early stage of the wave generation, **Fig. 2.14(b)** indicates that it rarely exceeded the both seaward and landward Shields parameters after $t_e = 30$ min, which corresponded to a very tiny volume of sediment transport (see **Fig. 2.4(b)**). In Case 6, as shown in **Figs. 2.13(c)** and **2.14(c)**, the fluctuation of φ_{dm} significantly decreased with time, and accordingly the value of φ_{dm} over the landward critical Shields parameter reduced in magnitude and frequency to be nearly comparable to that over the seaward critical Shields parameter. This trend of φ_{dm} was similar to the decreased q with time despite of overestimation in **Fig. 2.4(c)**.

For $d_{50} = 0.2$ mm, **Fig. 2.13(d)** shows that φ_d and φ_{dm} were almost same because there was no negative correlation between φ_d and γ . Consequently, although no figures in the other cases of $d_{50} = 0.2$ mm are presented, the unchanged relationship between φ_{dm} and q with that of φ_d and q was confirmed.

Overall, the temporal change in φ_{dm} was found to be similar with that in φ_d . However, the effects of the pore-water pressure influenced the decreased positive amplitude of φ_{dm} over the landward critical Shields parameter and the increased negative amplitude of φ_{dm} over the seaward critical Shields parameter compared with φ_d . Consequently, it was confirmed that the evaluation of the trend of q was improved using φ_{dm} in some cases. From these results, it is demonstrated that the use of φ_{dm} that considers the effects of the pore-water pressure is more suitable than that of φ_d to explaining the trend of q , especially when the construction sand is fine down to a median grain size of 0.1 mm. Furthermore, it is accordingly confirmed again in terms of φ_{dm} that it is essential to take into account the effects of the pore-water pressure in evaluation of the sediment transport.

2.4 Remarks

In this section, a series of hydraulic experiments on the wave-induced topographic changes in artificial shallows composed of fine sand were conducted. The characteristics of the topographic changes in terms of surrounding wave fields, the relationship between the Shields parameter and the relative vertical effective normal stress ratio, and the trend of sediment transport using a modified Shields parameter that considered the effects of pore-water pressure were examined. Experimental results showed that the trend of the topographic change in the shallows can be evaluated using the C_s value proposed by Sunamura and Horikawa (1974) when the water level on the crown of the shallows is shallower, *i.e.*, $h = 0.225$ m. It was also found that when the sand composing the shallows is fine down to a median grain size of 0.1 mm, the relative vertical effective normal stress ratio shows negatively correlated with the signed Shields parameter defined as positive landward, and its relationship is unchanged despite a change in the surface profile of the shallows. The result implies an acceleration in seaward sediment transport and a reduction in landward sediment transport without the effects of the topographic changes in the shallows. Furthermore, it was revealed that a signed Shields parameter considering

the effects of pore-water pressure gives a reasonable evaluation of the trend in the sediment transport. From these results, it was recommended that the effects of pore-water pressure should be taken into account when discussing the characteristics of the sediment transport in soil structures composed of fine sand.

Chapter 3

COMPUTATIONAL ANALYSIS

3.1 General

The verification of sediment transport problems, particularly for fine sediments in dredged sand, has many difficulties in laboratory conditions in terms of the degree of similarity. To overcome these limitations, numerical schemes to analyze hydraulic phenomena involving such sediment transport problems are enhanced with advances in the performance of computers.

In the past few decades, two-way coupling procedures for fluid dynamic models considering seabed profile evolution were developed for uniform flow (Brøns, 1999; Roulund *et al.*, 2005) and waves (Li *et al.*, 2002; Liang and Cheng, 2005; Nakamura and Mizutani, 2010). Nakamura and Yim (2011) developed a three-dimensional coupled fluid-structure-sediment interaction model (referred to as FSSM), which was combined with a two-way coupling procedure implemented at every time step to ensure fluid-structure-sediment interaction. In the surf zone where wave breaking occurs, it is important to track air-water interface motion precisely because vortices induced by wave breaking have a significant effect on suspended sediments. Three-dimensional numerical models dealing with complex air-water interface motion and suspended sediment transport were developed (Suzuki *et al.*, 2007; Liu and García, 2008), in some of which the diffusion of suspended sediment transport was ignored. Nakamura and Mizutani (2011) also improved the FSSM to take into account all suspended sediment transport processes of pickup, advection, diffusion and settling.

Based on the above-mentioned progress in numerical schemes, Nakamura *et al.* (2012) investigated the characteristics of wave-induced topographic change in

shallows composed of fine sand in terms of the effects of pore-water pressure using numerical model of the FSSM. They found that the prediction of the trend of topographic change of the shallows was improved by considering the gradient of pore-water pressure on the surface layer of the shallows. However, a sediment transport calculation of the FSSM was confirmed to be very sensitive to small variations in several parameters such as the critical Shields parameter, incident wave conditions, and mean water level drawing a different wave breaking position and trend of topographic change on the top of shallows, and they mentioned the necessity for further improvement in the FSSM (Nakamura *et al.*, 2012).

To address this issue, this section focuses on the factor of mean water level variation to investigate the effect on topographic change. The mean water level variation in the hydraulic experiments conducted in Chap. 2 is examined by means of two-dimensional numerical simulation with two different initial still water levels, $h = 0.2250$ and 0.2275 m. Specifically, the predicted results of water surface elevation and pore-water pressure are compared with the measured data in Chap. 2 in the early and latter stages. Moreover, the time evolution of topographic change in the shallows depending on different still water level conditions is investigated. The final topographic change is compared with the experimental results using the numerical results of topographic change and suspended sediment concentration. Finally, the effects of a still water level difference on the topographic change, *i.e.*, the mean water variation in the experiments, are discussed.

3.2 Numerical Model Description

The three-dimensional two-way coupled fluid-structure-sediment interaction model (FSSM) is composed of a main solver and three modules (Nakamura and Mizutani, 2010; Nakamura and Yim, 2011). The main solver is a large-eddy simulation (LES) model based on continuity and Navier-Stokes equations to compute incompressible viscous air, water, pore-air, and pore-water multi-phase flow that considers seepage flow in porous media. The three modules are: a volume-of-fluid (VOF) module based on the multi-interface advection and reconstruction solver (MARS) to track air-water interface motion; a sediment transport module (STM) to compute seabed profile evolution induced by the bed load and suspended sediment transport, and the motion of suspended sediment that considers all transport processes of pickup, advection,

diffusion, and settling; and an immersed-boundary (IB) module based on the body-force type of IB method dealing with the motion of a movable structure.

As stated above, the FSSM employs a two-way coupling procedure to connect the main solver, the VOF module, the STM and the IB module. **Figure 3.1** shows the coupling procedure, which is implemented in the follows:

1. The main solver is implemented.
2. The VOF module is activated using flow field data obtained from the main solver.
3. The STM computes sediment transport and updates seabed profile based on the flow field data and air-water interface data obtained from the VOF module.
4. The IB module applies the flow field data, the air-water interface data, and seabed profile data obtained from the STM to behavior of a structure.
5. The main solver at the next time step is carried out based on the air-water interface data, the seabed profile data, and structure motion data feeding back the results obtained from the VOF module, the STM and the IB modules into the main solver.
6. This procedure is iterated for specific numerical time steps.

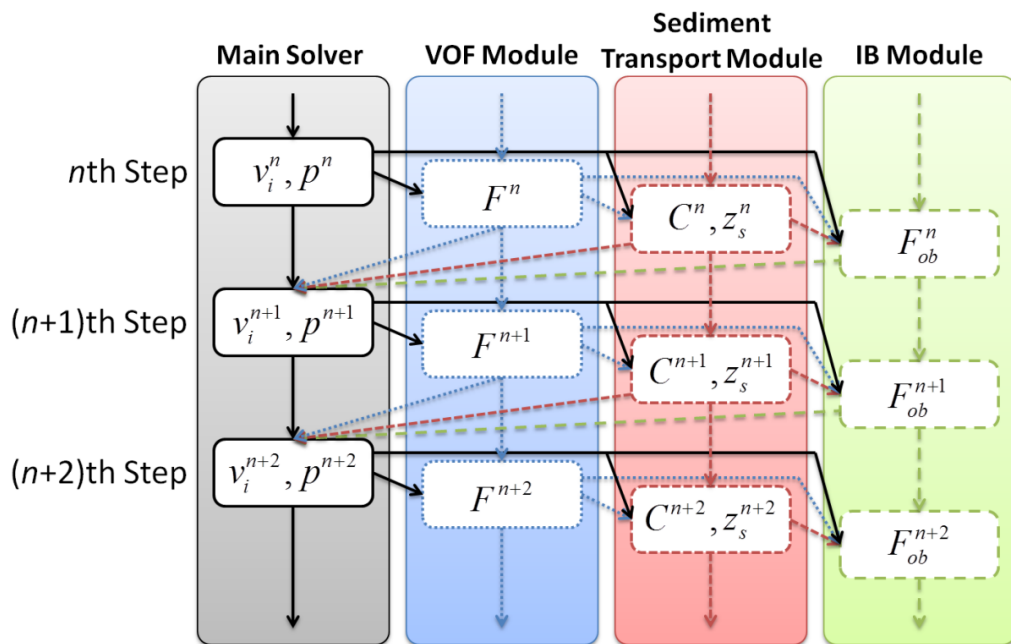


Fig. 3.1 Two-way coupling procedure of the FSSM.

In this study, the main solver, the VOF module, and the STM were used to compute wave-induced topographic change in shallows because the any motion of a movable structure was not included in the advanced experimental study (Chap. 2).

3.2.1 Generalized Navier-Stokes Solver (GNS)

Nakamura and Yim (2011) improved the governing equations eliminating the temporal derivative of the porosity m based on the assumption that the considerably small variation in m around the surface of the media can be neglected. The equations for the continuity, momentum and interface motion are as follows:

$$\frac{\partial(mv_j)}{\partial x_j} = q^* , \quad (3.1)$$

$$\begin{aligned} & \{m + C_A(1-m)\} \frac{\partial v_i}{\partial t} + \frac{\partial(mv_i v_j)}{\partial x_j} \\ & = -\frac{m}{\hat{\rho}} \frac{\partial p}{\partial x_i} + mg_i + \frac{m}{\hat{\rho}} (f_i^s + R_i) + \frac{\partial}{\partial x_j} (-m\tau_{ij}^a + 2m\hat{v}D_{ij}) + Q_i + m\beta_{ij}v_j \end{aligned} , \quad (3.2)$$

$$m \frac{\partial F}{\partial t} + \frac{\partial(mv_j F)}{\partial x_j} = Fq^* , \quad (3.3)$$

in which m is the volume fraction of void space in each cell ranging $1 \leq m \leq 0$ ($m = 0$ for pure impermeable solids; $1 < m < 0$ for porous media; and $m = 1$ for pure fluids); v_i and v_j are the fluid/seepage flow velocity vector; x_i and x_j are the position vector; q^* is the intensity of wave generation source/sink per unit time (Kawasaki, 1999); C_A is the added mass coefficient due to porous media; t is the time; p is the pressure; $g_i = -g\delta_{iz}$ is the gravitational acceleration vector (g_i is the gravitational acceleration; and δ_{ij} is Kronecker's delta); $\hat{\rho} = F\rho_w + (1-F)\rho_a$ is the density of fluid (subscripts of w and a indicate water and air respectively); F is the VOF function indicating the volume fraction of water in each cell ranging $0 \leq F \leq 1$ ($F = 0$ for air; $0 < F < 1$ for water surface; and $F = 1$ for water); f_i^s is the surface tension force vector based on the continuum surface force (CSF) model (Brackbill *et al.*, 1992); R_i is the laminar and turbulent drag force vector due to porous media (Mizutani *et al.*, 1996); τ_{ij}^a is the anisotropic part of the turbulent stress tensor; $\hat{v} = Fv_w + (1-F)v_a$ is the kinematic

molecular viscosity of fluid (subscripts are the same as $\hat{\rho}$); $D_{ij} = \partial v_i / x_j + \partial v_j / x_i$ is the strain rate tensor; Q_i is the wave generation source/sink vector; and β_{ij} is the artificial damping factor matrix. In the FSSM model, the x - and y -directions indicate the cross-shore and long-shore directions, respectively and the z -direction is the up and downward direction. In Eq. (3.2), f_i^s , R_i , Q_i and β_{ij} can be written as

$$f_i^s = \sigma \kappa \frac{\partial F}{\partial x_i} \frac{\hat{\rho}}{\bar{\rho}}, \quad (3.4)$$

$$R_i = -\frac{12C_{D2}\hat{\mu}(1-m)}{md_{50}^2}v_i - \frac{C_{D1}\hat{\rho}(1-m)}{2md_{50}}v_i\sqrt{v_jv_j}, \quad (3.5)$$

$$Q_i = v_i q^* - \frac{2}{3} \frac{\partial}{\partial x_i} \left\{ \hat{v} \frac{\partial (mv_j)}{\partial x_j} \right\}, \quad (3.6)$$

$$\beta_{ij} = \begin{cases} \beta(x, y, z) \delta_{iz} \delta_{jz} & \text{in artificial damping zone,} \\ 0 & \text{otherwise} \end{cases}, \quad (3.7)$$

in which σ is the surface tension coefficient; κ is the local surface curvature; $\bar{\rho} = (\rho_w + \rho_a) / 2$ is the density of fluid at the air-water interface; C_{D2} and C_{D1} are the laminar and turbulent drag coefficient, respectively; d_{50} is the median grain size of particles; $\hat{\mu} = \hat{\rho}\hat{v}$ is the molecular viscosity of fluid; and $\beta(x, y, z)$ is the artificial damping factor.

3.2.2 Sediment Transport Module (STM)

The mass conservation equation for sediments is as follows:

$$\frac{\partial z_s}{\partial t} + \frac{1}{1-m} \left(\frac{\partial q_x}{\partial x} + \frac{\partial q_y}{\partial y} \right) = 0, \quad (3.8)$$

in which z_s is the bed surface; and q_x and q_y are the bed load sediment transport rates in the x and y directions, respectively.

The bed load sediment transport rate per unit width and unit time in the i direction q_i is given as (Engelund and Fredsøe, 1976)

$$q_i = \frac{1}{6} \pi d p_{EF} v_{bi}, \quad (3.9)$$

in which v_{bi} is the sediment transport velocity in the i direction; d is the grain diameter; and p_{EF} is the percentage of sediment particles in bed load motion in the surface layer of the bed and it can be written as

$$p_{EF} \begin{cases} 0 & \text{if } \tau_* < \tau_{*c} \\ \frac{6}{\pi \mu_d} (\tau_* - \tau_{*c}) & \text{if } \tau_* \geq \tau_{*c} \end{cases}, \quad (3.10)$$

in which $\mu_d = \tan \theta_d$ is the dynamic friction coefficient of the particles (θ_d is the dynamic friction angle); τ_* is the Shields parameter; and τ_{*c} is the critical Shields parameter for a sloping bed (Brooks, 1963).

Suspended load in the FSSM is based on the equation proposed by Sakakiyama *et al.* (2004). The generalized advection-diffusion equation for computing suspended load in an entire water domain is expressed as

$$m \frac{\partial C}{\partial t} + \frac{\partial}{\partial x_j} (q_j^A + q_j^D + q_j^S) = 0, \quad (3.11)$$

in which C is the suspended sediment concentration and q_j^A , q_j^D and q_j^S are the suspended sediment transport fluxes due to advection, diffusion and settling, respectively. The equations of q_j^A , q_j^D and q_j^S are as follows:

$$q_j^A = m v_j C, \quad (3.12)$$

$$q_j^D = -m \varepsilon_s \frac{\partial C}{\partial x_j}, \quad (3.13)$$

$$q_j^S = m w_{sj} C, \quad (3.14)$$

in which ε_s is the diffusion coefficient of suspended particles and $w_{sj} = [0 \quad 0 \quad -w_s]^T$ is the settling velocity vector of particles.

The suspended sediment transport flux due to diffusion q_j^D is assumed as equaling to a pick up function p_N derived by Nielsen (1992). p_N is expressed as

$$p_N = \begin{cases} 0 & \text{if } \tau_* > \tau_{*c} \\ C_p \left(\frac{\tau_* - \tau_{*c}}{\tau_{*c}} \right)^{1.5} \frac{(s-1)^{0.6} g^{0.6} d_{50}^{0.8}}{\nu_w^{0.2}} & \text{if } \tau_* > \tau_{*c} \end{cases}, \quad (3.15)$$

in which C_p is the non-dimensional parameter involving sediment pickup; ν_w is the kinematic molecular viscosity of water; and $s = \rho_s / \rho_w$ is the specific weight of particles. More detailed explanations of the modules can be found in Nakamura and Mizutani (2010) and Nakamura and Yim (2011).

3.3 Numerical Conditions

A schematic of a computational domain is shown in **Fig. 3.2**. Based on the experimental setup in Chap. 2, shallows (crown width: 2.0 m, height: 0.2 m, seaward slope: 1/20), composed of fine sand with a median grain size d_{50} of 0.1 mm, was laid 1.4 m away from a wave generation source/sink, and a 0.2 m high vertical impermeable wall was fixed behind the shallows because it was observed in Nakamura *et al.* (2011) that the surface profile of the shallows exhibited little topographic change on its landward slope. To prevent reflected waves from seaward and landward boundaries, damping zones were set at more than twice the wavelength of incident waves. Note that the two-dimensional computational domain was adopted

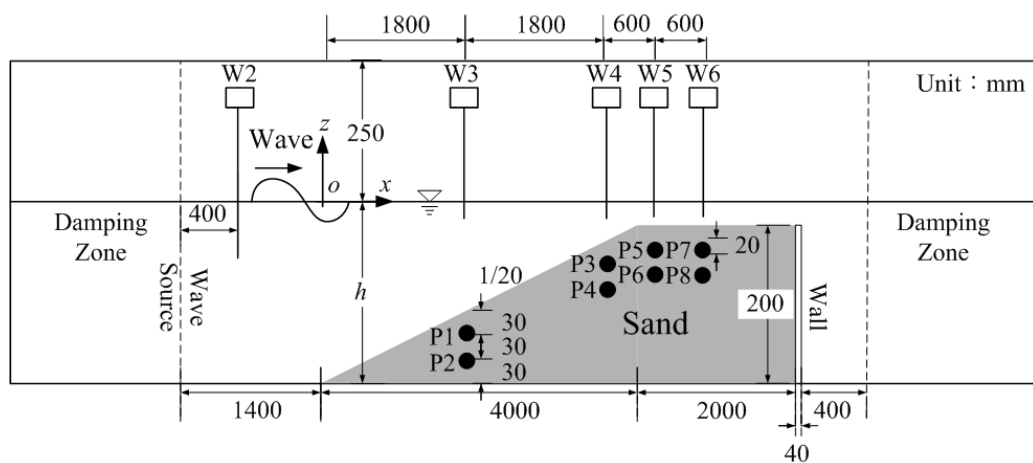


Fig. 3.2 Schematic numerical wave flume for a shallow profile change against regular waves: W2 to W6 are wave gages and P1 to P8 are pore-pressure gages.

Table 3.1 Parameters in the FSSM.

Gravitational acceleration g	9.81 m/s^2
Density of water ρ_w	$9.97 \times 10^2 \text{ kg/m}^3$
Density of air ρ_a	1.18 kg/m^3
Density of sand ρ_s	$2.65 \times 10^3 \text{ kg/m}^3$
Molecular viscosity of water ν_w	$8.93 \times 10^{-7} \text{ m}^2/\text{s}$
Molecular viscosity of air ν_a	$1.54 \times 10^{-5} \text{ m}^2/\text{s}$
Surface tension coefficient σ	$7.20 \times 10^{-2} \text{ N/m}$

to reduce computational cost on the assumption that the shallows had a uniform surface profile in the cross-shore direction.

The computational domain, except for the damping zones, was discretized with uniform numerical cells of $20.0 \text{ mm} \times 5.0 \text{ mm}$. The remainder of the entire domain was discretized with non-uniform numerical cells increasing in size in the x direction to further relieve computational cost. For flow velocity and pressure, the following boundary conditions were used: the slip condition for the surfaces of the bottom boundary and the vertical wall; the Sommerfeld radiation condition for the seaward and landward boundaries; and the constant-pressure condition for the top boundary. For the boundary condition of the VOF function, the gradient-free condition was used for all the boundaries. No bed load sediment was supplied from the seaward and landward edges of the shallows for the boundary condition of the bed load sediment transport. For the suspended sediment transport, the following boundary conditions were used: the impermeable condition for the surfaces of the bottom boundary and the vertical wall; and the gradient-free condition for the seaward and landward boundaries.

Table 1 lists the values of the main parameters adopted in the main solver of the FSSM based on the valued from National Astronomical Observatory of Japan (2003). The parameters relevant to porous media were determined based on the experimental results of Mizutani *et al.* (1996). These were the added mass coefficient $C_A = -0.04$, the turbulent drag coefficient $C_{D1} = 0.45$, and the laminar drag coefficient $C_{D2} = 25.0$. The porosity m of sand was taken as having a typical porosity value of 0.4. The dynamic friction coefficient μ_d was 0.51 (Fredsoe and Deigaard, 1992), the static friction coefficient μ_s was 0.63 (Lambe and Whitman, 2008), and the critical Shields parameter for a horizontal bed was adopted as 0.03.

Regular waves with an incident wave height H_i of 0.065 m, a period T of 1.0 s, and a still water depth h of 0.2250 m, which was selected as a representative wave condition from eight experimental cases in Chap. 2, were generated toward the shallows. In addition, a numerical experiment in which the still water depth on the crown was increased by 10%, *i.e.*, $h = 0.0275$ m on the crown of the shallows, thereby $h = 0.2275$ m in front of the shallows, was conducted to examine the effects of the still water level on sediment transport since the different trends of topographic change in the shallows was observed in the predicted and measured results for the same still water depth condition. It will be explained in Section 3.4. As the regular waves were generated, water surface elevations were measured at a point near the wave generation source/sink (W2) and four points over the shallows (W3–W6), and pore-water pressures on the surface layer of the shallows were measured at P1–P8 collocated with W3–W6 (**Fig. 3.2**).

3.4 Validation of the Mean Water Level

In this section, the predicted results of the water surface elevations and the pore-water pressures are validated with the experimental results in different still water levels, $h = 0.2250$ m identical to the experimental condition, and 0.2275 m, which was proposed in this section to examine mean water level variations in the experiments. The results for the early and latter stages are discussed with the different tendencies of water surface elevations and pore-water pressures (**Figs. 3.3** and **3.4**).

Figure 3.3 shows a comparison of the water surface elevations in the early stage ($t = 15.0$ – 20.0 s) and latter stage ($t = 35.0$ – 40.0 s), in which the red circles are measured results in the experiments of Chap. 2 and the blue and pink solid lines are predicted data in this simulation for $h = 0.2250$ and 0.2275 m, respectively. Overall, the predicted results show reasonable agreement with measured data in the both early and latter stages except for the results at W5 and W6, where phase shift occurred. This phase shift problem after wave breakings in numerical simulation is closer to a technical issue than hydrodynamic behavior, thus the phase shift phenomenon is not elaborated in this study. In the early stage after the waves were generated (**Fig. 3.3(a)**), the predicted results for $h = 0.2250$ m show good agreement with the experimental results in terms of the wave crests and troughs. However, as shown in **Fig. 3.3(b)**, in

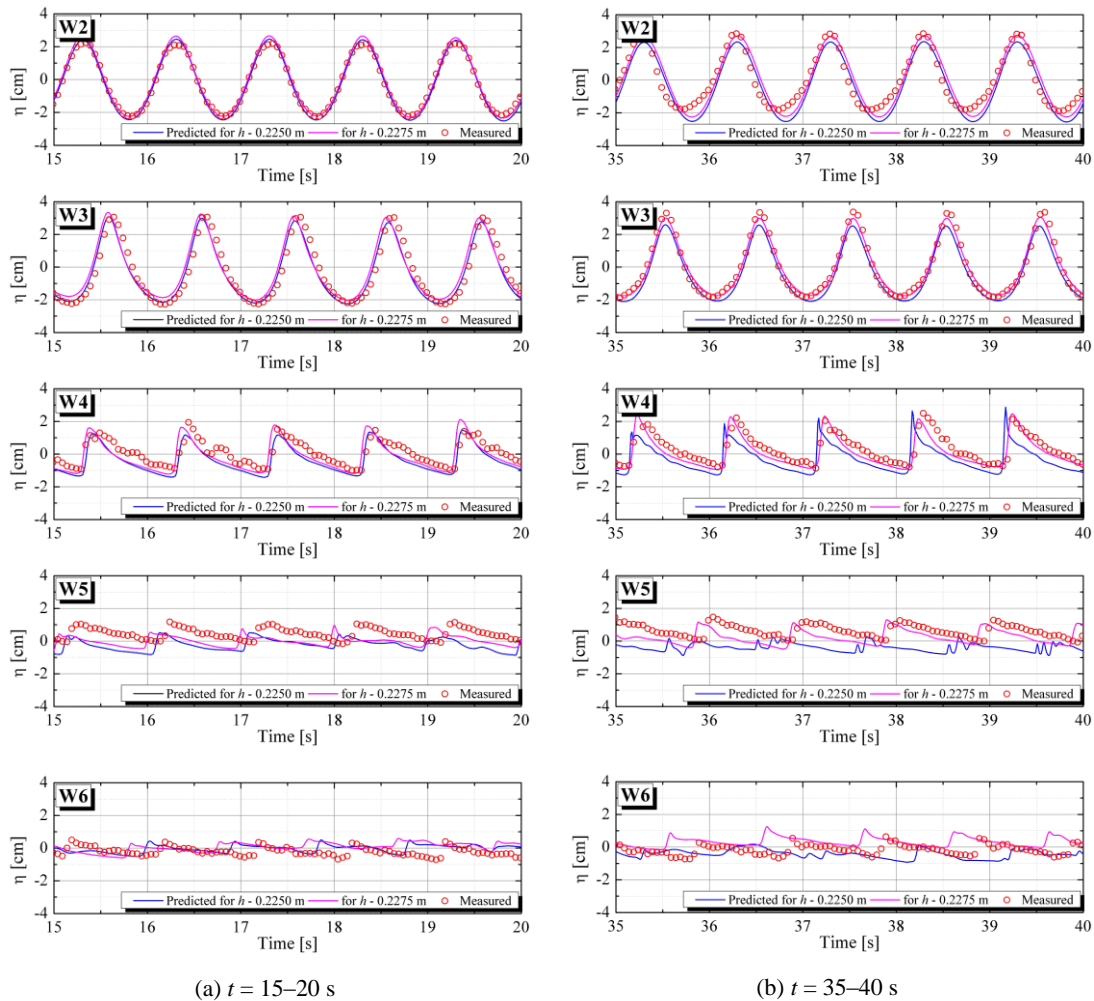


Fig. 3.3 Time series of water surface elevation predicted at W2, W3, W4, W5 and W6 for $h = 0.2250$ and 0.2275 m.

the latter stage, the results for $h = 0.2275$ m were consistent with the experimental results at all measurement points.

From the results at W2 and W3 over the area of pre-wave breaking, in the early stage, the predicted capability of the results for $h = 0.2250$ m was better than for $h = 0.2275$ m that were generally somewhat overestimated attributing to the higher still water level than the experiments. However, in the latter stage, the results for $h = 0.2250$ m fluctuated below the measured results, which was denoting an underestimation of the mean water level in the simulation. In contrast, it was found that the wave crests were predicted well in the results for $h = 0.2275$ m despite the slight underestimation of the wave troughs at W2 in the latter stage. Particularly at W3, the results for $h = 0.2275$ m show reasonable agreement with the measured data, which is different from the underestimated results for $h = 0.2250$ m. These tendencies

imply that the mean water level variation during the experimental time took place on the sloping shallows after about $t = 20$ s, and the rise in the mean water level around the shallows in the experiments can be assumed to be about 0.0025 m based on the results of the water surface elevations. A distinctive characteristic is observed at both W2 and W3. That is, the phase of the measured data seems to be a little slower than the both predicted results in the early stage, while the tendency is reversed in the latter stage as shown in **Figs. 3.3(a)** and **(b)**.

The results at W4 over the post-wave breaking area show a slightly different tendency. In the early stage, the results for $h = 0.2275$ m show better agreement with the measured results than for $h = 0.2250$ m despite the small phase shift. Furthermore, although the results for $h = 0.2275$ m are underestimated near wave troughs with little phase shift, the data for $h = 0.2275$ m are in reasonable agreement with the measured data in the latter stage. It is assumed that the mean water level variation near W4 occurred early than W3, which will be discussed later. At W5 and W6, the magnitude of wave height was well matched to the measured data. However, at W5 and W6 in the area behind the breaking wave, a phase shift was observed and the phase lag became larger away from the breaking point. These phase problems are, as aforementioned earlier, still remained task to overcome the problem in post-wave breaking area for precisely estimating wave fields in the landward area.

The pore-water pressure results are depicted in **Fig. 3.4**, where the red squares are the measured results in Chap. 2 and the solid blue and pink lines are the predicted results, the blue lines for $h = 0.2250$ m and the pink lines for $h = 0.2275$ m. In this study, the pore-water pressure results are described at P1 and P2 over the pre-wave breaking area corresponding to the location at W3, and P3 and P4 over the post-wave breaking area corresponding to the location at W4.

From the results at P1, in the early stage, the crests and troughs of the pore-water pressure for the both predicted results show good agreement with the measured data, which was different from the results at W3 appearing better results for $h = 0.2250$ m. This result indicates that the influence of the small change of 0.0025 m in the still water level between two cases is insignificant to change a tendency of the pore-water pressure results since this pore-water pressure results are dynamic pressures varied by water surface fluctuation with time. However, the predicted

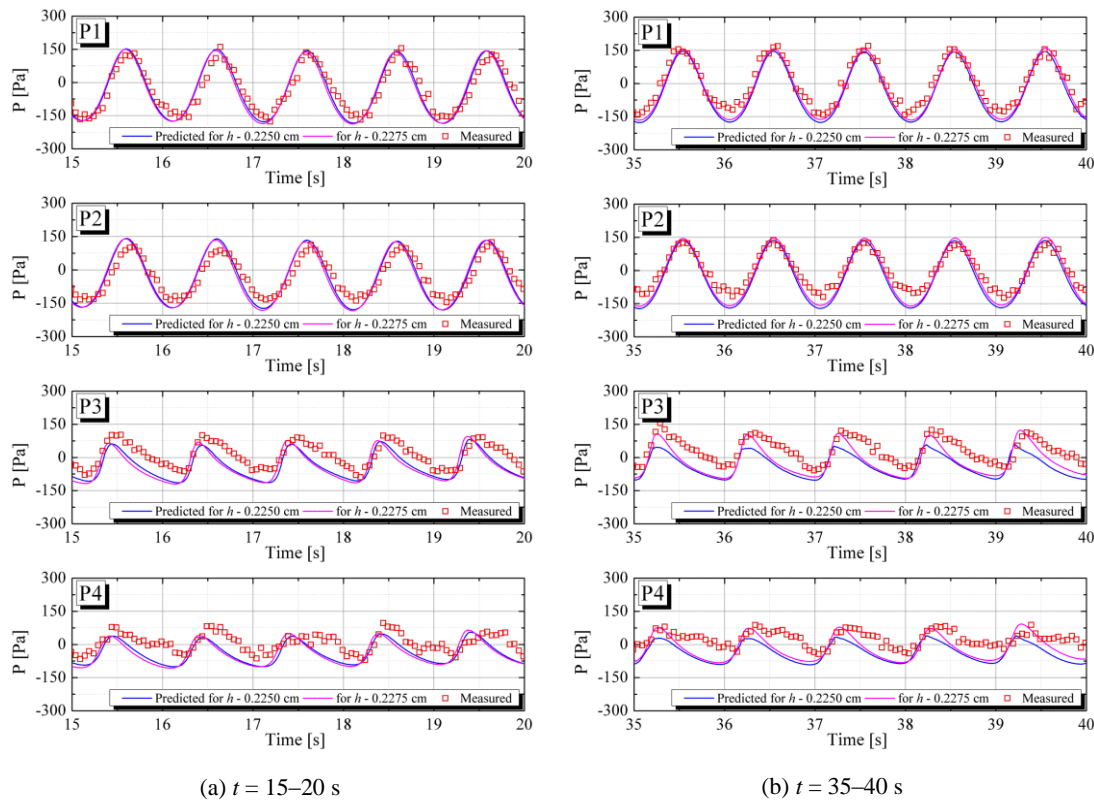


Fig. 3.4 Time series of the pore-water pressure in the shallows at P1, P2, P3 and P4 for $h = 0.2250$ and 0.2275 m.

results of the pore-water pressures show underestimation in the latter stage (**Fig. 3.4(b)**). At P2, which was buried in the shallows 30 mm deeper than P1, the predicted results were underestimated compared with the measured data. It seems that this tendency was dependent on the influence of the porosity. Though a constant value of porosity was used during the numerical simulation, the porosity can vary in the experiments because of natural consolidation and compaction induced by wave action. At P3 and P4 over the post-wave breaking area, the overall predicted results were underestimated. The crests of the pore-water pressure were reproduced well for $h = 0.2275$ m, whereas the troughs were underestimated. In the pore-water pressure results, the phase shift phenomenon also was observed at P1 and P2 with time, which was similar to the results at W3 in the experiments.

These results suggest that, in the hydraulic experiments, a slight rise in the mean water level, which was assumed to be about 0.0025 m around the shallows, was induced by some factors other than the wave setup. In the experiments, as mentioned in Chap. 2, the 2.22-m wide wave tank was divided into the 0.40-m wide channel and the remaining channel by the partition board, and shallows were installed in the former wave channel. However, the partition board did not extend sufficiently to a

wave absorbing beach at the end of the wave tank. Accordingly, it is inferred that the mean water level rose around the wave absorbing beach at the side of the remaining channel due to different hydraulic conditions between two channels with whether the shallows were installed or not, which were able to influence the velocity of the propagating waves, and its propagation to the 0.40-m wide channel used in the experiments generated and caused the further rise in the mean water level around the shallows. In contrast, in the numerical simulations, it was difficult to apply such the phenomenon of additional rise in the mean water level in the two-dimensional computational domain that was used to take into account an appropriate balance with computational cost. However, as shown in **Figs. 3.3** and **3.4**, the increase of 0.0025 m in the still water depth equivalent to 10% of the initial still water depth on the crown, improved efficiently the computational accuracy of the simulations and this improvement of the simulation was noticeable in the results of topographic change which is described in Section 3.5. From this result, it is suggested that it is necessary to confirm the condition of mean water level variation in three-dimensional hydraulic experiments, especially in the case of incompletely blocked out experimental domain, when simulating a two-dimensional numerical simulation for sufficient accuracy.

3.5 Effects of Still Water Level on the Topographic Change in the Shallows

The final topographic change in the shallows is discussed with respect to the effects of the still water level. **Figures 3.5(a)** and **3.5(b)** show the final profiles of the shallows and the topographic change in the shallows. In this study, the final topographic change and profile defined the results at $t = 1$ min. The red circles are the measured data, the blue solid line is the predicted results for $h = 0.2250$ m, and the pink dashed line is the predicted results for $h = 0.2275$ m.

As shown in **Fig. 3.5(b)**, erosion and accretion are shown alternately from $x = 1.5$ m to $x = 3.0$ m in the measured results, and there is little topographic change in the area behind $x = 4.0$ m where the horizontal region of the shallows begins. However, the predicted results for $h = 0.2250$ m shows substantial erosion in the horizontal region of the shallows ($x \geq 3.7$ m). In addition, accretion occurred in $x = 5.0$ – 5.5 m and near the vertical wall. In contrast, for $h = 0.2275$ m, little topographic change on the top of the shallows was observed. It was consistent with the trend in the measured data. Only a small quantity of erosion took place on the

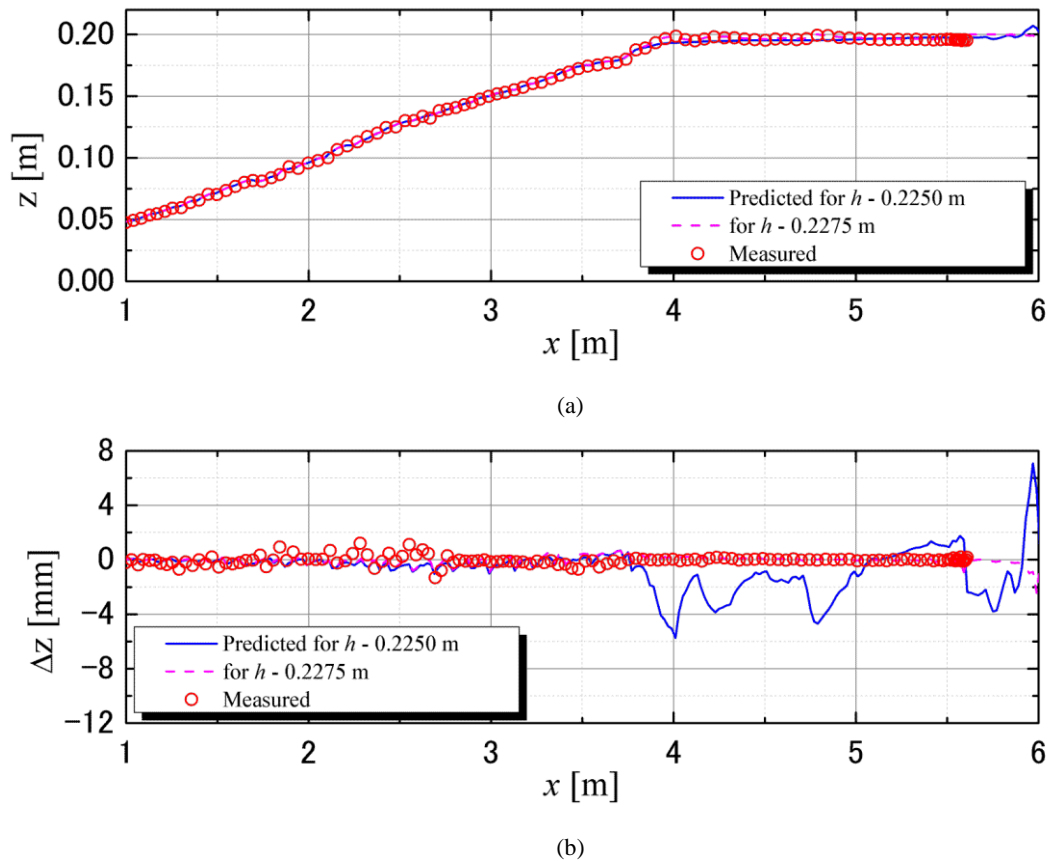


Fig. 3.5 Cross-shore distribution of: (a) final shallows profile and (b) topographic change with different still water levels of $h = 0.2250$ and 0.2275 m.

middle of the slope, in which incident waves experience shoaling in the form of an increase in wave height. Moreover, erosion is also shown near the wall, which differed from the results for $h = 0.2250$ m. It is difficult to discuss the validity of the topographic change near the vertical wall because any comparable measured data were unavailable as a result of the limitations in the measurement devices.

From the comparison of the results for $h = 0.2250$ m and 0.2275 m, the increase in the initial still water level seemed to suppress sediment transport near the top of the shallows by thickening the fluid layer above them. The increase of 0.0025 m in still water level is a very small quantity with 1.1% of total water depth, while it is corresponding to 10% of water depth on the crown of the shallows. The thickened water layer on the crown of 10% seems to be enough to reduce wave energy and results in less topographic change in the crown. Furthermore, an increase in still water level above the shallows also causes the different hydrodynamic conditions such as a breaking point migration. Wave breaking is one of the important factors of erosion

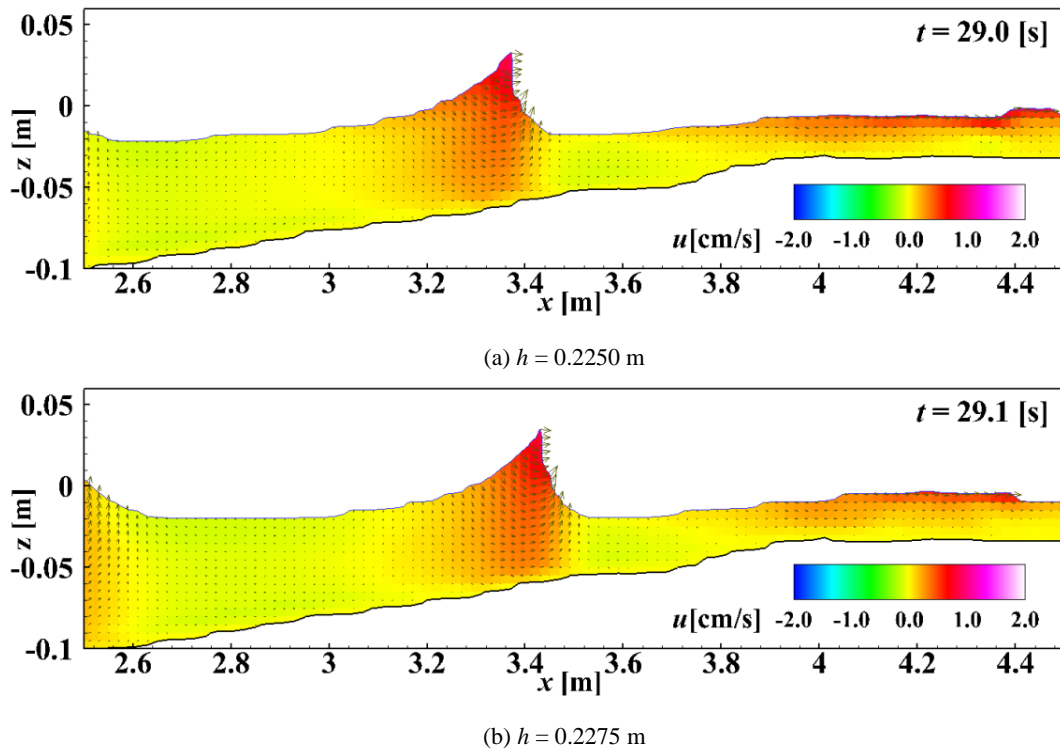


Fig. 3.6 Distribution of the horizontal velocity u .

and the unstable and driving flows generated after wave breaking play the important role of eroding and entraining sediments on the bed. Thus, the condition of wave breaking should be considered to estimate sediment transport problems.

As shown in **Fig. 3.6**, the tendency for wave breaking in different positions with still water level changes was observed. Wave breaking was determined by the moment of the highest wave height at the simulation time with the appearance of the velocity vector on the top of the wave falling down in the results of the time series of wave motion with velocity vectors. Wave fields with horizontal velocity u contours are presented over the shallows for $h = 0.2250$ at $t = 29.0$ s and 0.2275 at $t = 29.1$ s. Vectors indicate wave velocity components consisting of u and w in the x direction and z direction, respectively. The snapshots represent the waves on the verge of breaking with the steepest face just before the wave approaching the shallows begins to recede. The positions of the breaking waves varied with the still water levels as shown in **Fig. 3.6**. Despite of the increase of 0.0025 m in the still water level, the position of the breaking waves moved landward about 0.14 m. Each breaking position was approximately $x = 3.34$ m for $h = 0.2250$ m and $x = 3.40$ m for $h = 0.2275$ m away from the beginning of the shallows. These different wave breaking positions

also resulted in the considerably dissimilar results of topographic change. That is, the predicted hydrodynamic condition for $h = 0.2275$ m, in which wave breaking appears closer to the crown of the shallows, is supposed as a neighboring result to the experiments.

Consequently, as mentioned earlier, the predicted results for the increase of 10% in the still water level on the crown of the shallows represent good correspondence with the measured data in the results of topographic change. These results emphasize again the importance to consider mean water level variation resulting in dissimilar topographic change due to the different tendency of wave fields on the shallows and wave breaking.

3.6 Suspended Sediment Concentration

In this section, time dependent distributions of suspended sediment concentration are investigated to give a better understanding of sediment transport around the shallows and the characteristics of the topographic change in the shallows with two different still water levels, $h = 0.2250$ and 0.2275 m.

When the initial still water level h is 0.2250 m, the predicted distribution of suspended sediment concentration (**Fig. 3.7(a)**) and the topographic change in the shallows (**Fig. 3.7(b)**) are depicted. The results were taken at $t = 19.8, 20.5, 24.0, 26.3, 34.5, 38.4,$ and 57.6 s when different suspended sediment movements on the shallows were confirmed between the results for $h = 0.2250$ and 0.2275 m. In **Fig. 3.7(a)**, the red contour means a high density of suspended sediment concentration. Incident waves experienced shoaling effects when approaching the shallows as shown in **Fig. 3.7(a)** at $t = 19.8$ and 24.0 s. As these surface waves were entering a shallower water area on the slope of the shallows with an increase in wave height, wave velocity near the shallows increased, and the shallows were then agitated by the waves. This shoaling process on the shallows results in the sediments triggering to suspend near $x = 1.60$ m away from the beginning of the shallows, and the sediment transport on the shallows takes place according to the migration of crests of incident waves. The suspended sediments by the progressing waves seemed to be entrained to near $x = 3.60$ – 3.70 m with low concentrations. During this process, wave breaking was observed between $x = 3.40$ – 3.60 m accompanied with low but relatively higher suspended sediment concentration (see **Fig. 3.7(a)** at $t = 19.8, 24.0,$ and 26.3 s).

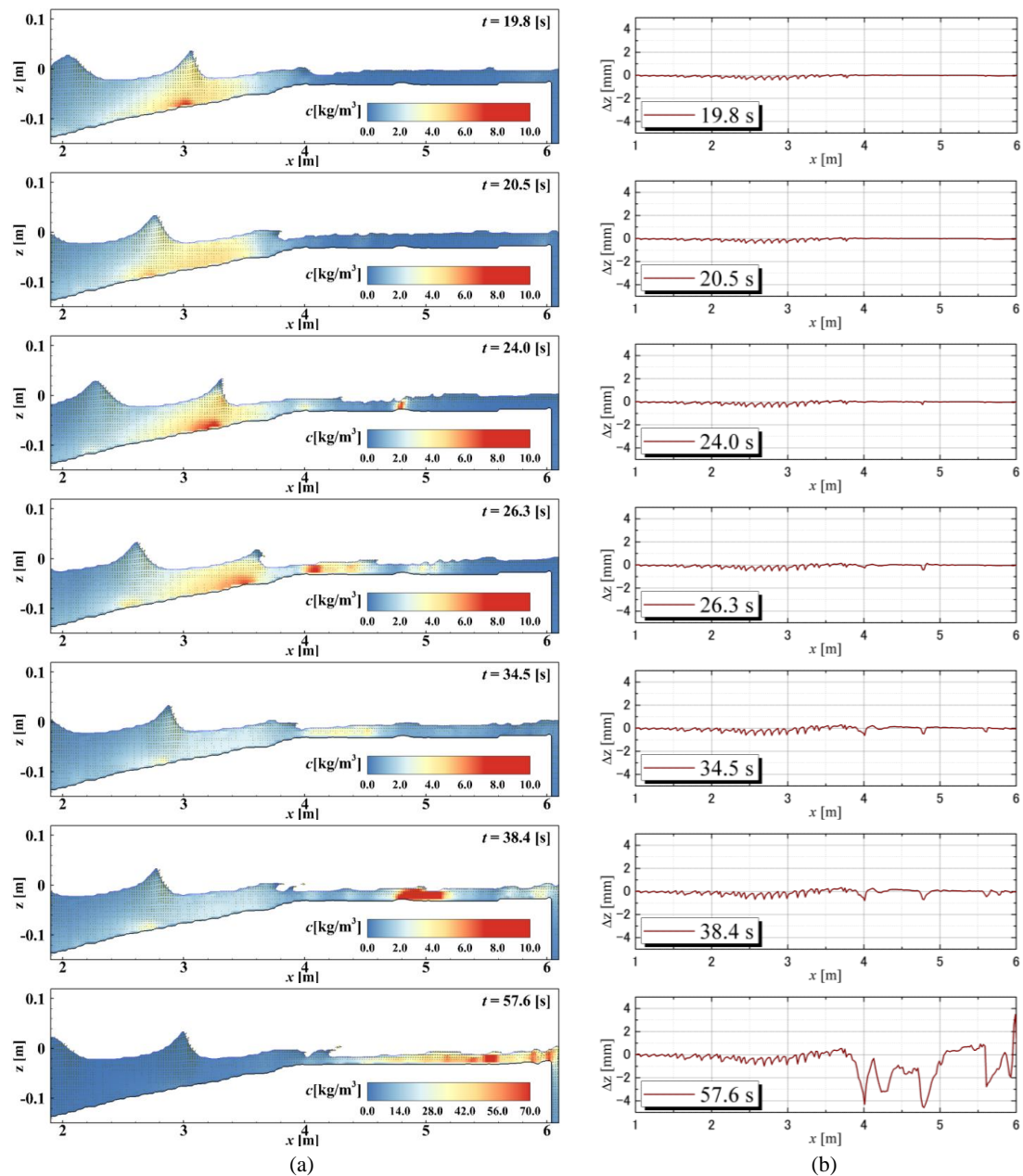


Fig. 3.7 Cross-shore distribution of: (a) suspended sediment concentration and (b) topographic change for $h = 0.2250$ m at $t = 19.8, 20.5, 24.0, 26.3, 34.5, 38.4,$ and 57.6 s.

However, most of entrained suspended sediments, which were generated from around $x = 1.60$ m and the wave breaking zone, stayed in the surf zone that is located from approximated $x = 2.25$ – 3.80 m, and only a part of the suspended sediments migrated to the direction of wave progress by the flow generated from the wave breaking. These results were also observed in the results of topographic change (**Fig. 3.7(b)**) showing the disturbed temporary topography of the shallows ranging from $x = 2.10$ – 3.50 m after $t = 19.8$ s.

The other trend of the phenomenon of suspensions over time was observed, especially on the top of the shallows. Prominent suspended sediments occurred near the protruding area (approximately $x = 4.80$ m) on the shallows temporarily at $t = 24.0$ s and the beginning of the horizontal area of the shallows ($x = 4.10$ m) at $t = 26.3$ s. The latter phenomenon of suspensions persisted with small quantities of sediment concentration after $t = 26.3$ s. The erosion near the protruding location, which was observed transiently at $t = 24.0$ s, took place again at the same position after $t = 38.4$ s as shown in **Fig. 3.7(a)**. This result is also confirmed in **Fig. 3.7(b)** at about $x = 4.80$ m where the protruding topography was located. The somewhat erosion in protruding area on the top of the shallows occurred in the early numerical time accelerated, and sequent erosion took place over time near the same position. Eventually, this consecutive process drew considerable erosion on the top of the shallows as shown in **Fig. 3.7(a)** at $t = 57.6$ s. A remarkable characteristic of this erosion is that copious amounts of suspended sediments eroded on the top of the shallows migrated behind the shallows contrary to those on the sloped shallows, which mostly stayed in the surf zone. In addition, deposited sediments were observed at $x = 4.90$ – 5.60 m and near the vertical wall. The deposition seemed to be fed from the sediments suspended on the top of the shallows. These results were clearly observed in the results for the topographic change (**Fig. 3.7(b)**).

For $h = 0.2275$ m, the suspended sediment concentration and topographic change in the shallows are presented in **Figs. 3.8(a)** and **3.8(b)**. Similar to the results for $h = 0.2250$ m, a part of the bottom sediment was agitated near the inclined shallows as shown in **Fig. 3.8(b)**. A dissimilar characteristic to the results for $h = 0.2250$ m was shown in the suspension of sediments near the vertical wall during the early time steps. A small quantity of suspended sediments are observed near the vertical wall indicating thin yellow contour in **Fig. 3.8(a)** at $t = 19.8$ s. The erosion continued for the simulation time. The intensity of suspended sediments gradually increased until $t = 57.6$ s and then decreased as shown in **Fig. 3.8(a)**. The results of suspension are also confirmed in the topographic change results (**Fig. 3.8(b)**). Erosion depth in front of the vertical wall increased for the simulation time and it was observed that substantial erosion took place during $t = 38.4$ – 57.6 s (**Fig. 3.8(b)** at $t = 57.6$ s). Another noticeable characteristic is that there was little erosion on the top

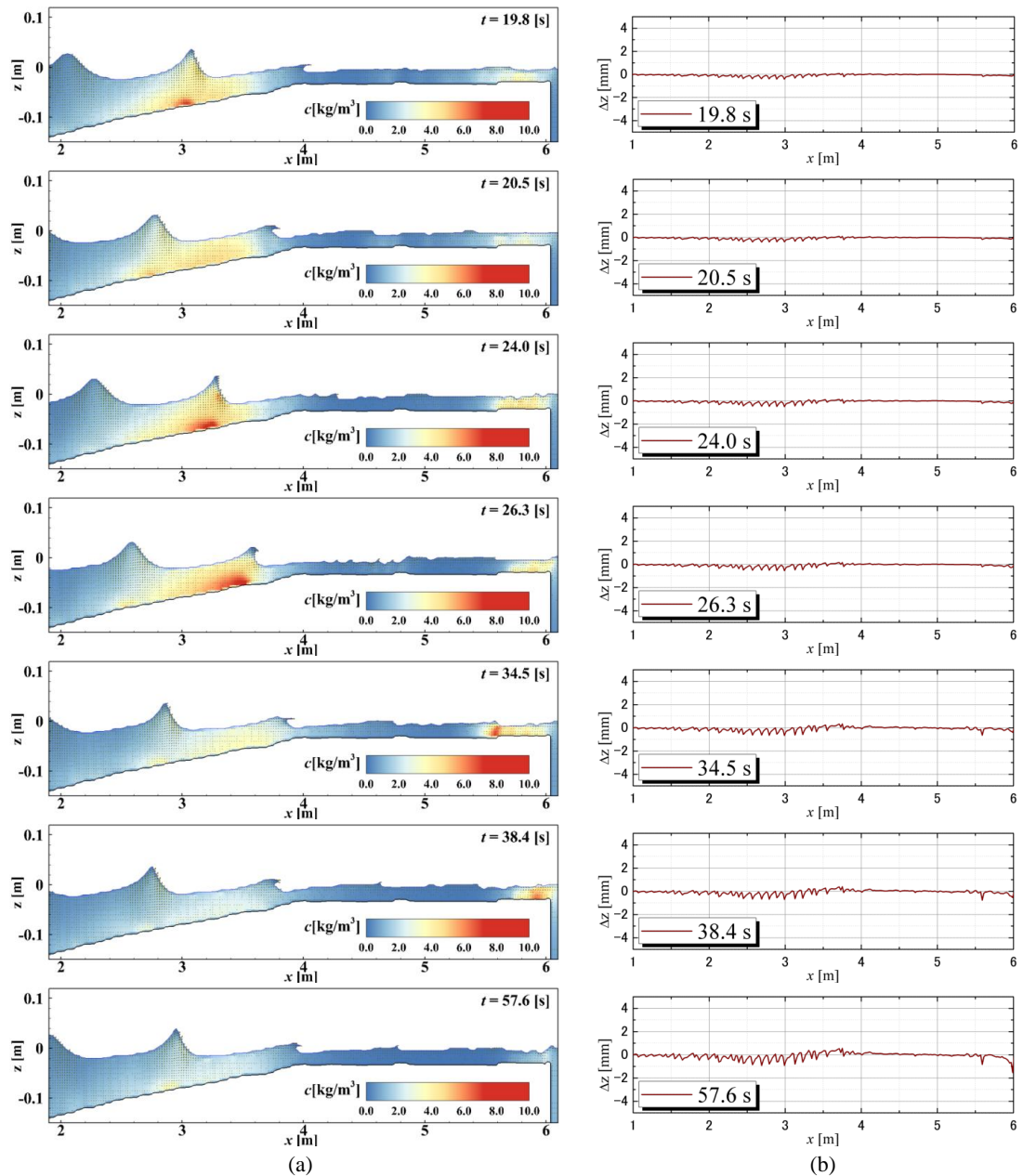


Fig. 3.8 Cross-shore distribution of: (a) suspended sediment concentration and (b) topographic change for $h = 0.2275$ m at $t = 19.8, 20.5, 24.0, 26.3, 34.5, 38.4,$ and 57.6 s.

of the shallows, which was the identical result to the laboratory experiments (Fig. 3.5(b)).

Consequently, different still water levels, $h = 0.2250$ and 0.2275 m, contributed to the separate trend of topographic change and the hydrodynamic conditions on the shallows. As mentioned before, the position where the wave breaking occurred and thickened water layer on the crown were the important factor for analyzing erosive phenomenon in the surf zone. However, only the factor of wave breaking point is not enough to explain the different trend in topographic change due to the small amount

of differences between two still water levels. The most important factor in initiating sediment movement is the horizontal flow velocity component. In particular, in the surf zone, there are substantially disturbed wave fields generated by wave breakings. When the waves fall down to the shallower water of the shallows, relatively more disturbed and faster flows are generated bounding up and down. If horizontal flows are enough to stimulate incipient motion of sediments and approach closely to the bottom, the surface of the shallows are exposed to erosion such as the results for $h = 0.2250$ m. Furthermore, because of the relatively shallower fluid layer on the top of the shallows similar to the case for $h = 0.2250$ m, the energetic turbulences are likely to influence the shallows directly. However, an increase of 10% in water level on the top of the shallows seems to play the role to absorb considerable part of the turbulence, *i.e.*, relatively weakened turbulent flows with the low velocity approach the surface of the shallows, thus the erosion on the top of the shallows is reduced. In the laboratory experiments, the reason for little erosion on the top of the shallows is expectable through the aforementioned process based on the results of mean water level variation during the experimental time.

3.7 Remarks

The improvement in the predictive capability of the FSSM with an increase in still water level has been presented. The predicted results for the water surface elevation and pore-water pressure suggest that an increase in mean water level occurred near the shallows in the latter stage of the experiments because the predicted results for $h = 0.2275$ m had reasonable agreement with the measured data different from those for $h = 0.2250$ m, which matched well with the measured data in the early stage, while somewhat discrepancy appeared in the latter stage. The results showed somewhat variation of mean water level in the both experiment and numerical simulation can have significant effects on the tendency of topographic change in the shallows, thus, the attention of conforming mean water level variation is highlighted when simulating wave-induced topographic change in two dimensions. The results of the suspended sediment concentration and topographic change offered comprehensive understandings of the characteristics of sediment migration. Improved predictive capability of the FSSM model in terms of the analysis of wave-induced topographic change was confirmed by managing the initial still water level.

Chapter 4

SEDIMENT TRANSPORT CALCULATION CONSIDERING COHESIVE EFFECTS

4.1 General

The stability of artificial shallows composed of dredged sand against incident waves is of concern because of the low weight of fine sediments in the dredged sand. The experimental study described in Chap. 2 was carried out in terms of the characteristics of the topographic change in shallows comprised of fine sand. However, the experiments encountered limitations because it only considered non-cohesive fine sand, whereas actual dredged sand contains fine sediments with cohesive forces. Moreover, there is little understanding of the characteristic of cohesive fine sediment transport and the topographic change in artificial shallows made up of dredged sand.

Most research on sediment transport phenomena has been based on non-cohesive sediments and there is little research that accounts for the effects of cohesive forces in topographic change. Ashida *et al.* (1982) proposed a formula concerning the non-dimensional critical shear stress and the non-equilibrium sediment transport of the sand particles. This formula considered the effects of the fine sediments with cohesive force (hereinafter called clay) existing in the pore space of the sand particles and confirmed the validity of the formula through comparison with experimental tests. However, there was no attempt to apply the cohesive effects to the formula in wave fields, which is a more energetic environment than river stream, and to analyze the characteristics of sediment transport covering the cohesive effects in mixed soil coexisting with sand and clay. Consequently, the characteristics of sediment transport

in mixed soil including cohesive effects are not fully understood, particularly in a coastal field.

In this section, a sediment transport calculation considering the cohesive effects induced by clay in the pores of sand particles is proposed and the basic characteristics of the calculation are investigated in terms of the correlation between cohesive intensity and the bed load sediment transport rate. In addition, the calculation is incorporated into a three-dimensional coupled fluid-structure-sediment interaction model (FSSM) developed by Nakamura *et al.* (2011), which can analyze the interaction between waves and topographic change. The calculation is also applied to the condition of hydraulic experiments on the topographic change in shallows composed of fine sand (Chap. 2). Last, the predictive capability of the modified model is examined with experimental results and a sensitivity analysis is carried out in terms of the effects of cohesive force on the topographic change in the shallows assuming that clay exists in the pores of the sand particles of the shallows.

4.2 Sediment Transport Calculation Considering Cohesive Effects

Sediment transport calculation considering the cohesive effects induced by clay contained in the pores of the sand particle is proposed following Ashida *et al.* (1982). Specifically, the critical Shields parameter τ_{*c} and bed load sediment transport rate q_i are modified.

Ashida *et al.* (1982) considered the soil mixture composed of spherical sand particles with uniform particle diameter d_{50} and clay filling in the pores of the sand particles as a bed condition. It was assumed that the friction between the sand particles did not change even for the condition without clay. That is, even though the clay is eliminated, sand particles can maintain a static stable state. Based on the assumptions, the clay-induced cohesive force F_C can be expressed by

$$F_C = k_1' d_{50}^2 f_c, \quad (4.1)$$

in which $k_1' d_{50}^2$ is the cohesive area of the clay contributing to the cohesive resistance and f_c is the cohesive resistance force of the clay per unit surface area. Here, assuming that the cohesive area per contact point between sand particles is a , the cohesive area a can be obtained approximately from a simple geometric relationship with some physical factors of cohesive sediments as in Ashida *et al.* (1982). As shown in

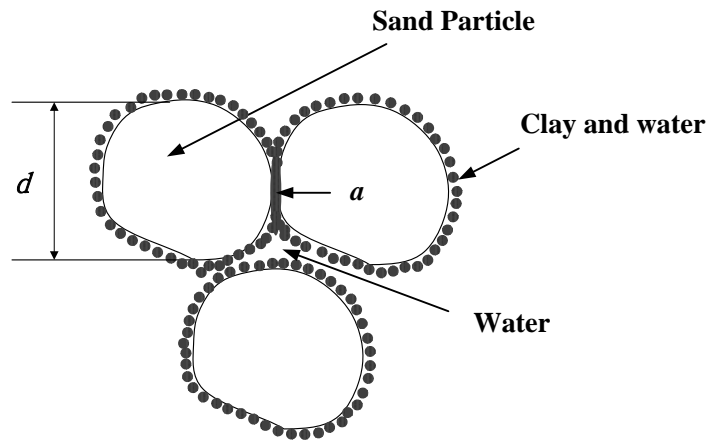


Fig. 4.1 The concept of sand-clay mixture (Ashida *et al.*, 1982).

Fig. 4.1, when one sand particle is supported by the number of contact points n , this can be given by $k_1' d_{50}^2 = an$, and finally, Eq. (4.1) is rewritten by

$$F_C = \frac{\pi d_{50}^2}{4} \left[\left\{ 1 + \frac{1}{1-m} \frac{p_f(1+s\omega)}{p_f s\omega + 1} \right\}^{2/3} - 1 \right] n f_c, \quad (4.2)$$

in which m is the porosity; p_f is the content ratio of the clay; ω is the water content; and s is the specific weight of the sand particle ($= \rho_s/\rho_w$, where ρ_s is the sand particle density and ρ_w is the water density). Additionally, there are the submerged weight of the particle W , and the drag and lift forces F_D and F_L , which depend on the bottom velocity. The forces acting on the sand particles, apart from the cohesive force F_C expressed in Eq. (4.2), are expressed as follows:

$$W = \frac{1}{6} \pi (\rho_s - \rho_w) g d_{50}^3, \quad (4.3)$$

$$F_D = \frac{1}{8} \pi \varepsilon C_{D1} \rho_w d_{50}^2 v_r^2 = C_{FD} v_r^2, \quad (4.4)$$

$$F_L = \frac{1}{8} \pi \varepsilon C_L \rho_w d_{50}^2 v_r^2 = k_L C_{FD} v_r^2, \quad (4.5)$$

in which g is the gravitational acceleration; ε is the shading coefficient; C_{D1} and C_L are the turbulent drag and lift coefficients, respectively; k_L is the ratio between C_{D1} and C_L ($= C_L/C_{D1}$); v_r is the relative flow velocity acting on the particle for the mean transport velocity v_b of a sediment particle in bed load motion; and $C_{FD} = \pi \varepsilon C_{D1} \rho_w d_{50}^2 / 8$. In the following, τ_{*c} and q_i are derived by incorporating the effects of F_C .

4.2.1 Critical Shields parameter

In the critical state, the forces acting on a sand particle exist as shown in **Fig. 4.2**. Here, v_f is the friction velocity; C_{vf} is the coefficient of the friction velocity; α is the angle between the flow velocity $C_{vf}v_f$ and the direction of the steepest bed slope; Ψ is the angle between the flow velocity $C_{vf}v_f$ and the sediment transport velocity v_b ; and Ψ_1 is the angle between the relative flow velocity v_r and the sediment transport velocity v_b . The values of F_{DC} , F_{LC} , v_{fc} , v_{bc} , v_{rc} , α_c , Ψ_c and Ψ_{1c} represent those of F_D , F_L , v_f , v_b , v_r , α , Ψ and Ψ_1 in the critical state. In addition, β is the angle of the steepest bed slope and μ_s is the static friction coefficient of the sand particle. In this case, $v_{bc} = 0$, which means that $v_{rc} = C_{vf}v_{fc}$ and $\Psi_c = \Psi_{1c}$, because it is under the critical state. The formulations of Ψ_c and v_{rc}^2 are given as follows from the force balance in the directions the same as and perpendicular to v_{bc} :

$$v_{rc}^2 = \frac{\{\mu_s \cos \beta - \sin \beta \cos(\alpha_c - \Psi_c)\}W + F_c}{(\cos \Psi_c + \mu_s k_L)C_{FD}}, \quad (4.6)$$

$$\Psi_c = \arctan \left\{ \frac{W \sin \beta \sin \alpha_c}{C_{FD}v_{rc}^2 + W \sin \beta \cos \alpha_c} \right\}, \quad (4.7)$$

In Eq. (4.7), Ψ_c and α_c have the same sign and $|\Psi_c| \leq |\alpha_c|$. Here, the unknown parameters, v_{rc}^2 and Ψ_c , are determined by iterative calculations. Defining τ_{*c0} as a critical Shields parameter in the horizontal plane ($\beta = 0$) without considering the cohesive force (*i.e.*, $F_C = 0$), τ_{*c} can be written by the following equation:

$$\frac{\tau_{*c}}{\tau_{*c0}} = \frac{v_{fc}^2 / \{(s-1)gd_{50}\}}{v_{fc0}^2 / \{(s-1)gd_{50}\}} = \frac{v_{rc}^2 / \{C_{vf}^2(s-1)gd_{50}\}}{v_{rc0}^2 / \{C_{vf}^2(s-1)gd_{50}\}} = \frac{v_{rc}^2}{v_{rc0}^2}, \quad (4.8)$$

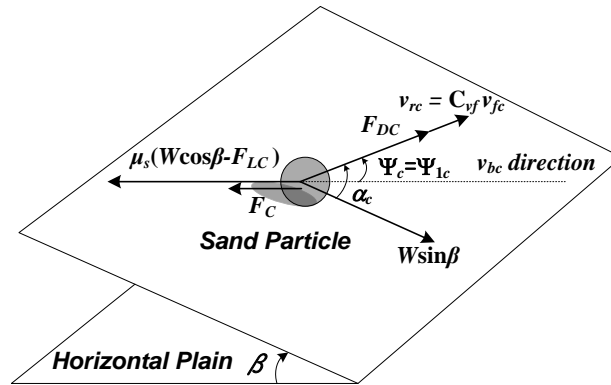


Fig. 4.2 Force balance on a sediment particle on a sloping bed in the critical state.

in which v_{rc0}^2 and v_{fc0}^2 are v_{rc}^2 and v_{fc}^2 in the horizontal plane ($\beta=0$) without the cohesive force ($F_C=0$), and v_{rc0}^2 is obtained from substituting $F_C=\beta=\Psi_c=\Psi_{1c}=0$ into Eq. (4.6) as follows:

$$v_{rc0}^2 = \frac{\mu_s W}{(1 + \mu_s k_L) C_{FD}}, \quad (4.9)$$

Furthermore, for the cross-sectional two-dimensional phenomenon, the following equation is obtained because of $\alpha_c = \Psi_c = \Psi_{1c} = 0$:

$$\frac{\tau_{*c}}{\tau_{*c0}} = \frac{(\mu_s \cos \beta - \sin \beta)W + F_c}{\mu_s W}, \quad (4.10)$$

In addition, the influence of the cohesive force is also considered to be a pickup function of suspended sediment through the value of the critical Shields parameter τ_{*c} .

4.2.2 Bed load sediment transport rate

The bed load sediment transport rate q_i per unit width and unit time is defined as follows (Engelund and Fredsøe 1976):

$$q_i = \frac{1}{6} \pi d_{50} p_{EF} v_{bi}, \quad (4.11)$$

where p_{EF} is the percentage of sediment particles in bed load motion in the surface layer of the bed, which is expressed as

$$p_{EF} = \begin{cases} 0 & \text{if } \tau_* \leq \tau_{*c} \\ \frac{6}{\pi \mu_d} (\tau_* - \tau_{*c}) & \text{if } \tau_* > \tau_{*c} \end{cases}, \quad (4.12)$$

in which μ_d is the dynamic friction coefficient ($\mu_d \leq \mu_s$) and τ_* is the Shields parameter, which is defined as:

$$\tau_* = \frac{v_f^2}{(s-1)gd_{50}}, \quad (4.13)$$

Figure 4.3 shows the agitating and stabilizing forces acting on a sand particle in the bed load motion. The equation of motion in the same direction as the sand particle movement (*i.e.*, the direction of v_b) is given as:

$$F_D \cos \Psi_1 + W \sin \beta \cos(\alpha - \Psi) = \mu_d (W \cos \beta - F_L) + F_c, \quad (4.14)$$

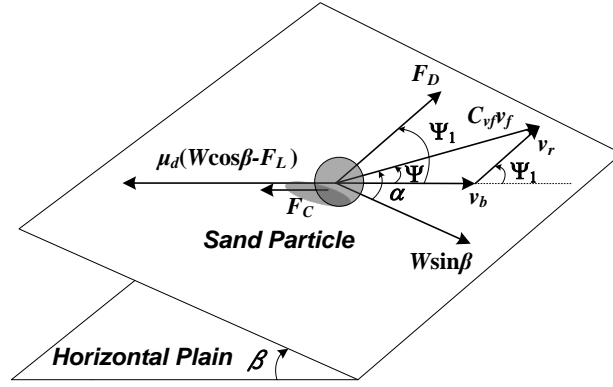


Fig. 4.3 Force balance on a moving sediment particle on a sloping bed.

In the same way, the equation of motion in the direction perpendicular to the sand particle movement is

$$F_D \sin \Psi_1 = W \sin \beta \sin(\alpha - \Psi), \quad (4.15)$$

In addition, the simple geometric relationship between v_b , $C_{vf} v_f$ and v_r gives

$$v_r \sin \Psi_1 = C_{vf} v_f \sin \Psi, \quad (4.16)$$

$$v_r \cos \Psi_1 + v_b = C_{vf} v_f \cos \Psi, \quad (4.17)$$

Here, there are four unknown variables (*i.e.*, v_b , v_r , Ψ and Ψ_1) and four equations, and v_{bi} is computed by iterative calculations. Thus, the bed load sediment transport rate q_i is given by Eqs. (4.11) and (4.12) together with τ_{*c} that is obtained in the previous section. Furthermore, for the cross-sectional two-dimensional phenomenon, the equation is summarized as follows from the relationship of $\alpha = \Psi = \Psi_1 = 0$:

$$v_b = C_{vf} v_f - v_r, \quad (4.18)$$

$$v_r = \left\{ \frac{(\mu_d \cos \beta - \sin \beta)W + F_c}{C_{FD}(1 + \mu_d k_L)} \right\}^{1/2}, \quad (4.19)$$

4.3 Characteristics of Sediment Transport Calculation Considering Cohesive Effects

In this section, the fundamental characteristics of the proposed sediment transport calculation are investigated based on Eqs. (4.10), (4.18) and (4.19) for a cross-sectional two-dimensional condition, for which there is no need to perform any iterative calculation. Specifically, sand particles with $\rho_s = 2.65 \times 10^3 \text{ kg/m}^3$, $d_{50} = 0.1 \text{ mm}$, and $\tau_{*c0} = 0.03$ were assumed to be on the horizontal plane ($\beta = 0^\circ$).

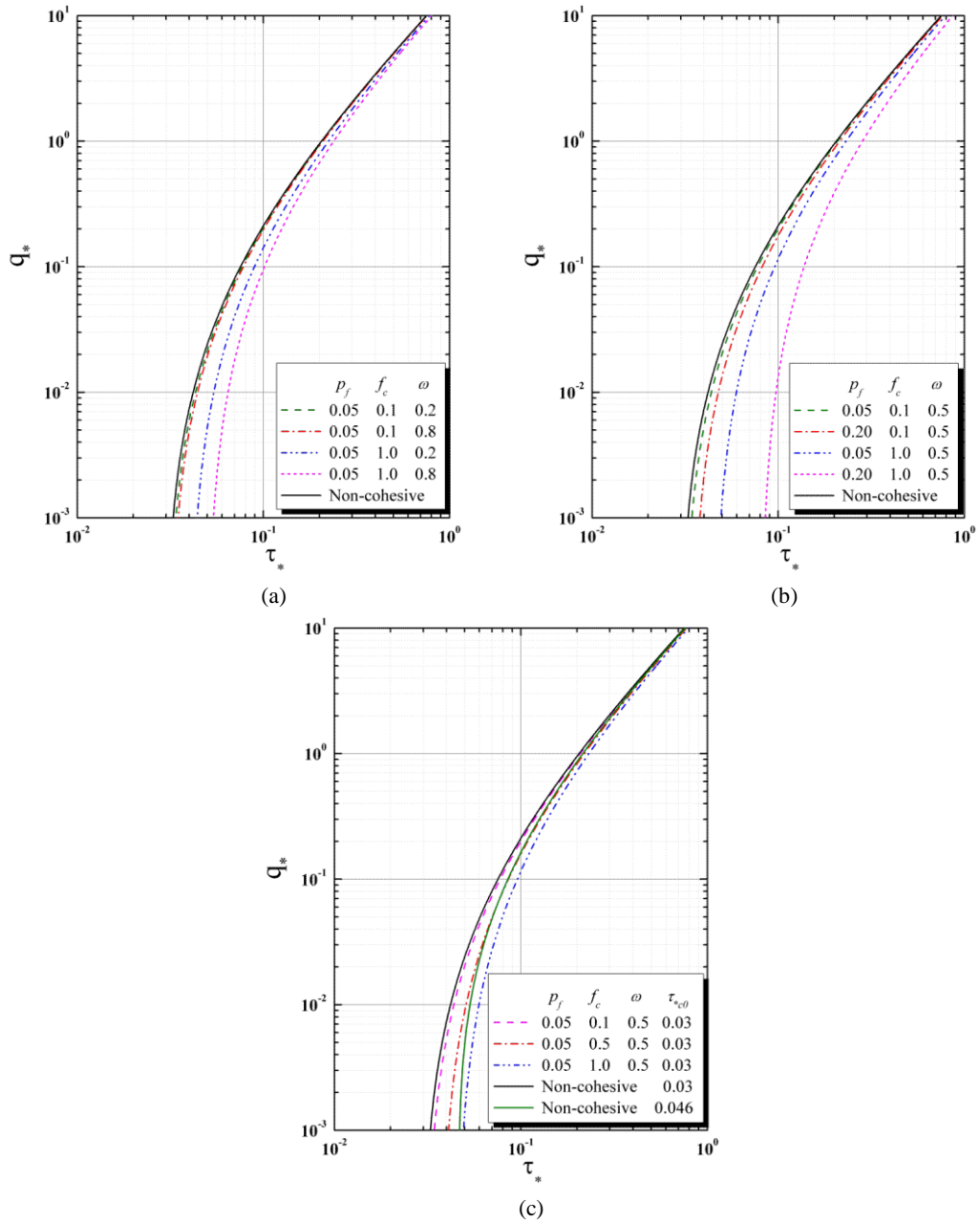


Fig. 4.4 Non-dimensional bed load sediment transport rate q_* versus the Shields parameter τ_* : (a) the characteristic of q_* according to ω ; (b) the characteristic of q_* according to p_f ; and (c) the characteristic of q_* according to f_c .

The three cases for the water content ω ($= 0.2, 0.5$ and 0.8), two cases for the content ratio of the clay p_f ($= 0.05$ and 0.20) and three cases for the cohesive force per unit surface area f_c ($= 0.1, 0.5$ and 1.0 N/m^2) were then used as the main variables. The calculation for a non-cohesive condition ($f_c = 0.0 \text{ N/m}^2$) was also carried out for comparative analysis. Other parameters were adopted by the following values: $g = 9.81 \text{ m/s}^2$, $\rho_w = 9.97 \times 10^2 \text{ kg/m}^3$, $C_{D1} = 0.45$, $C_{vf} = 10.0$, $k_L = 0.85$, $\varepsilon = 0.4$, $\mu_s = 0.63$ and $\mu_d = 0.51$.

Figure 4.4 shows the relationship of the non-dimensional bed load sediment transport rate q_* versus the Shields parameter τ_* . As shown in **Fig. 4.4(a)**, an increase in ω causes an increase in the critical Shields parameter τ_{*c} . In addition, it is observed that q_* tends to decrease with an increase in ω when the same condition of τ_* . However, the effect of ω on q_* varies with the value of f_c . The decline in q_* increases with an increase in f_c (see the red and pink dotted line/the green and blue dotted line in **Fig. 4.4(a)**). A similar phenomenon is also observed in **Fig. 4.4(b)**. Although a decrease in q_* according to an increase in p_f is small for $f_c = 0.1 \text{ N/m}^2$, it is found that a degree of decline in q_* for $f_c = 1.0 \text{ N/m}^2$ is larger than that for $f_c = 0.1 \text{ N/m}^2$ (see **Fig. 4.4(b)**). In **Fig. 4.4(c)**, the value of τ_{*c} increases with an increase in f_c , and it is also found that q_* decreases with an increase in f_c . Furthermore, the case of $\tau_{*c0} = 0.046$ that is the solid green line for the non-cohesive condition ($f_c = 0.0 \text{ N/m}^2$), and the case of $f_c = 1.0 \text{ N/m}^2$ with $\tau_{*c0} = 0.03$, which is the blue two-dot chain line, are compared based on the same critical Shields parameter τ_{*c} , *i.e.*, τ_{*c} is approximately equal to 0.046 when $f_c = 1.0 \text{ N/m}^2$ with $\tau_{*c0} = 0.03$. A different trend in q_* is observed in spite of the same critical Shields parameter, that is, q_* for $f_c = 1.0 \text{ N/m}^2$ is smaller than that for non-cohesive effect consideration. This result emphasizes the importance of appropriate modeling taking into account the cohesive effects caused by the clay in sediment transport calculation since the cohesive force influences not only the increasing critical Shields parameter, but the trend of bed load sediment transport rate.

4.4 Three-dimensional Coupled Fluid-Structure-Sediment Interaction Model

The three-dimensional coupled fluid-structure-sediment interaction model developed by Nakamura *et al.* (2011) is briefly described in this section. The model is composed of a main solver and three modules. The main solver is a large-eddy simulation (LES) based on a continuity equation and a Navier-Stokes equation for analyzing the motion of an incompressible viscous air-water two-phase fluid including the pore fluid inside the porous media taking into account the movement of the movable structure and topographic change. The three modules are a volume-of-fluid (VOF) module based on the multi-interface advection and reconstruction solver (MARS) to track the gas-liquid interface, an immersed-boundary (IB) module based on the body-force type of IB method dealing with the movable structure, and the sediment transport module to analyze the concentration of suspended sediment transport and the topographic

change associated with bed load and suspended sediment transport. The three modules are incorporated into the main solver with a two-way coupling technique to take into account the fluid-structure-sediment interaction. Here, the proposed sediment transport calculation was applied into the sediment transport module to take into account the cohesive effects caused by clay filling in the pores of the sand particles. It should be noted that, in this section, the IB module was not included because motion of the structure was not dealt with.

4.5 Application of the Modified Model Considering Cohesive Effects

The modified model is applied to hydraulic experiments on the topographic change in artificial shallows consisting of fine sand (Chap. 2) and a numerical simulation is carried out on the supposed condition that the pores of the sand particles contain the clay with the cohesive force. The sensitivity analysis of the modified model is also investigated focusing on the relationship between the variation of the parameters (f_c , p_f , ω) and topographic change in the shallows.

4.5.1 Numerical condition

Figure 4.5 shows a schematic of a computational domain. As shown in **Fig. 4.5**, shallows (height: 20.0 cm; crown width: 200.0 cm; slope gradient: 1/20) composed of fine sand with a median grain size, $d_{50} = 0.1$ mm, was installed based on the initial topography measured in the hydraulic experiments. In addition, a wave generating source/sink was placed 140.0 cm away from the beginning of the shallows, and damping zones were installed in the offshore side of the wave generating source and the onshore side of the vertical wall. Here, the length of the damping zones was about twice as long as the incident wavelength to reduce the wave reflection from the

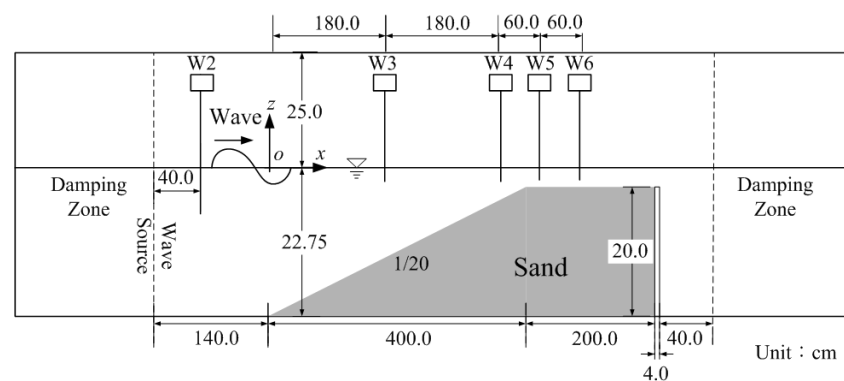


Fig. 4.5 Computational domain for the topographic change in the shallows.

boundaries. Regular waves were generated with a wave height $H_i = 6.5$ cm, a wave period $T = 1.0$ s, and a still water depth $h = 22.75$ cm that was described amply in Chap. 3. The entire domain except for the damping zones was discretized using orthogonal staggered cells with a uniform size of $\Delta x = 2.0$ cm and $\Delta z = 0.5$ cm, whereas non-uniform cells widening gradually were used in the damping zones for efficient numerical simulation. The boundary conditions were the same as in Nakamura *et al.* (2012). The parameters were the porosity of fine sand $m = 0.4$, the density $\rho_s = 2.65 \times 10^3$ kg/m³, the critical Shields parameter on the horizontal plane $\tau_{*c0} = 0.03$, the submerged angle of repose $\theta_r = 30.0^\circ$. The main physical parameters of cohesive forces were used by three cases of f_c ($= 0.1, 0.5$ and 1.0 N/m²) and p_f ($= 0.05, 0.10$ and 0.20), and five cases of ω ($= 0.3, 0.5, 0.8, 0.9$ and 1.0). Other computational parameters were referred to in Nakamura *et al.* (2011).

4.5.2 Effects of the cohesive force on the topographic change in shallows

The sensitivity analysis for the main parameters (f_c , ω and p_f) contributing to cohesive force is carried out with $h = 22.75$ cm to investigate the effects of the cohesive force on the topographic changes in the shallows. It is assumed that clay filled the pores of the sand particles forming the shallows. The cohesive resistance force per unit surface area f_c , the water content ω and the content ratio of the clay p_f are noted as the main parameters which arouse cohesive force, and the effects of these parameters on the topographic change in the shallows are investigated.

The effects of f_c , ω and p_f on the topographic change Δz at $t = 60$ s are shown in **Fig. 4.6**. In the figure, only Δz in the range of $x = 50$ – 450 cm of the whole domain is presented because the topographic change mainly occurred on the slope of the shallows as shown in Chap 3. It was confirmed from the result in **Fig. 4.6(a)** that the amount of Δz tends to decrease with an increase in f_c . Specifically, when f_c was increased from 0.1 N/m² to 1.0 N/m², it was observed that little deposition emerged on the location from the upper slope to the crown and little erosion appeared on the middle of the slope. This is because, as shown in **Fig. 4.4(c)**, the critical Shields parameter increased and the bed load sediment transport rate decreased with an increase in f_c , and finally this sequence had the effect of decreasing Δz . In the result for ω , although Δz decreased with an increase in ω , the distinction was very small as shown in **Fig. 4.6(b)**. This result is close relation to the small value of f_c , 0.1 N/m²

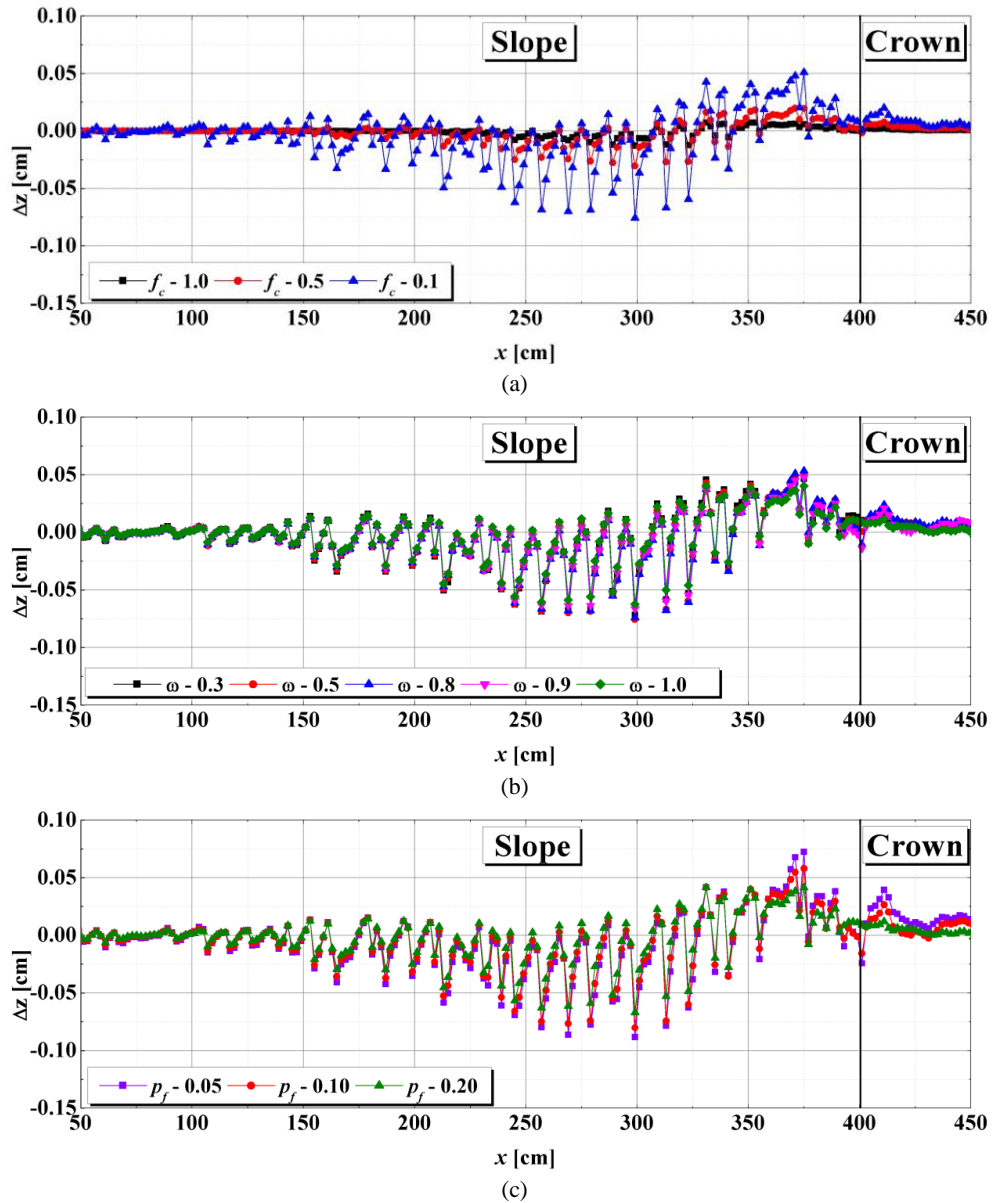


Fig. 4.6 Difference in the amount of topographic change Δz caused by the cohesive force at $t = 60$ s: (a) the effects of the cohesive force per unit surface area ($\omega = 0.5$, $p_f = 0.15$); (b) the effects of the water content ($p_f = 0.15$, $f_c = 0.1$ N/m²); (c) the effects of the content ratio of the clay ($\omega = 0.5$, $f_c = 0.1$ N/m²).

that was adopted on account of the little topographic change that occurred for $f_c = 1.0$ N/m². In addition, the effects of ω on the critical Shields parameter and the bed load sediment transport rate were very small when $f_c = 0.1$ N/m² as shown in **Fig. 4.4(a)**. A similar trend to that shown in **Fig. 4.6(b)** is also observed in **Fig. 4.6(c)**. The variation of the parameters f_c , ω and p_f seems to have little effect on the trend for the topographic change in the shallows in these simulations. The little trend of topographic change seems to contradict the result shown in **Fig. 4.4**, which shows different trend of q^* with an increase in Shields parameter according to the intensity of

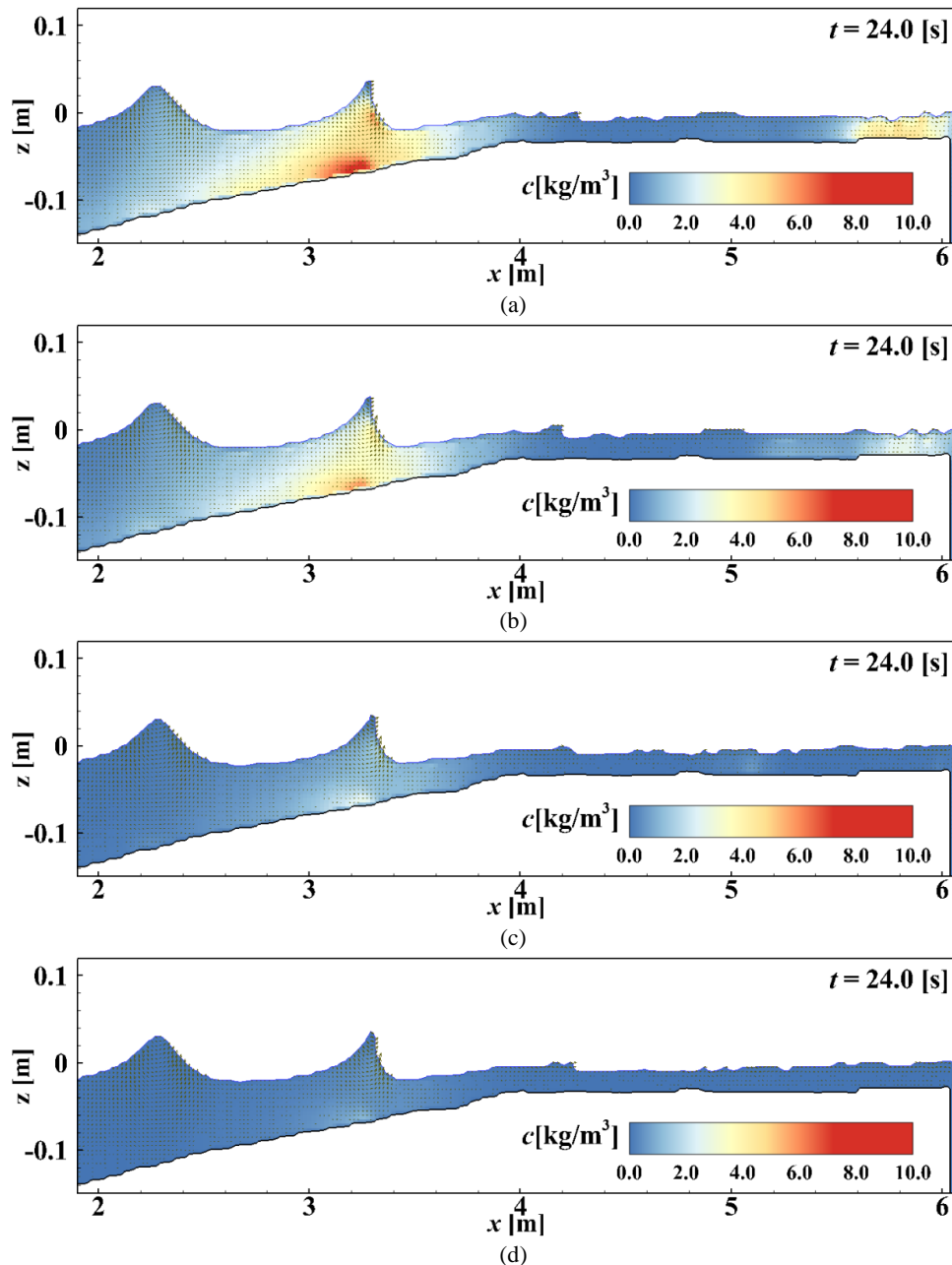


Fig. 4.7 Comparison of cross-shore distribution of the suspended sediment concentration at $t = 24$ s: (a) with non-cohesive effect; (b) $f_c = 0.1 \text{ N/m}^2$; (c) $f_c = 0.5 \text{ N/m}^2$; (d) $f_c = 1.0 \text{ N/m}^2$ ($\omega = 0.5$, $p_f = 0.15$).

cohesive force. The inconsistency in the different results of the trend of topographic change can be considered as follows. First, the simulation time is too short to reflect the characteristics of cohesive effects on bed load trend. If extending the simulation time, successive varied velocity field induced by the evolved topography near the surface of the shallows would cause different trends between topographic change in non-cohesive and cohesive shallows. Secondly, the flow velocity near the sloping shallows in the simulation is so small that the trend of topographic change is not

outstanding to be recognizable in the results due to the somewhat differences of q_* at low f_c . Therefore, these results imply that by filling the pores of the sand particles with clay, the wave-induced topographic change in the shallows can be reduced without changing the topographic change pattern under the conditions of relatively short duration or mild wave fields.

The snapshots of suspended sediment concentration at $t = 24.0$ s when the different trends in suspended sediments are shown obviously are presented in **Figs. 4.7(a)-(d)**. In the case of a non-cohesive condition, *i.e.*, the same as the experimental condition, suspended sediments are observed on the slope of the shallows and near the wall located on the end of the shallows as shown in **Fig. 4.7(a)**. However, as cohesive force increases, it is shown that the relatively stabilized shallows are observed with low concentration of suspended sediments, in particular in the results for $f_c = 1.0 \text{ N/m}^2$. The sediment migration behavior of the case considering cohesive effects shows the similar process to the case for the non-cohesive sediment condition on the slope of the shallows as described in Chap 3. That is, the initial suspended sediments take place on the region apart from the initial point of the shallows and are entrained to the end of the slope, and only a part of the entrained sediments is propagate with flow generated after wave breaking. However, the amount of the sediment traveling is very small for the case considering cohesive effects.

4.6 Remarks

In this section, the sediment transport calculation considering the cohesive force generated by clay filled in the pore between sand particles was proposed. The basic characteristics of the calculation were examined, and the numerical simulation model incorporating the proposed calculation was investigated by applying it to the hydraulic experiments on the topographic change in the shallows composed of fine sand. In addition, the sensitivity analysis of the cohesive effects on the topographic change in the shallows was conducted. As a result, the conclusion can be summarized as follows:

1. Through the relationship between the non-dimensional bed load sediment transport rate and Shields parameter, an increase in the cohesive resistance force per unit surface area f_c , the water content ω and the content ratio of

the clay p_f contribute to an increase in the critical Shields parameter and a decrease in the bed load sediment transport rate. Furthermore, the existence of clay in the pores of the sand particles indicates the importance of proper modeling taking into account the cohesive effects. This is because the results presented different patterns for the bed load sediment transport rate between the cases considering cohesive and non-cohesive effects in spite of the same critical Shields number.

2. By carrying out the sensitivity analysis on the effects of the three parameters, f_c , ω and p_f , on the topographic change in the shallows, it was confirmed that the topographic change decreased with an increase in f_c , ω and p_f . In addition, the results show that the consideration of the cohesive effects had little influence on the topographic change pattern in the simulations because of relatively gentle wave conditions and short simulation time. Consequently, the possibility of reducing topographic change by containing the clay in the sand particles is confirmed.

From these results, the computational capability of this proposed model for analyzing sediment transport problems in mixed soil condition coexisting with sand and clay was confirmed.

Chapter 5

INFLUENCE OF COHESIVE SEDIMENTS ON TOPOGRAPHIC CHANGE IN A TIDAL FLAT

5.1 General

Constructions of tidal flats and shallows with dredged sand near coastal regions have a variety of benefits in coastal environments and calmness, while there still remains little understanding to the structural stability of dredged sand against waves. Generally, since dredged soil consists of cohesive sediments more than 60%, dredged sand should contain an amount of cohesive sediments. Thus, one of the major required understandings is the cohesive effects on erosion in mixed sediments. Most studies on sediment transport have been conducted with either cohesive or non-cohesive sediments due to quite differences of behavior characteristics and physical properties between them. In advanced researches on the condition of sand-mud mixtures, it was found that an even small volume of sand adding to mud resulted in a significant increase in erosion resistance (McCave, 1984) and an increase in mud content in sand-mud mixtures decreased erosion (Amos *et al.*, 1996; Kamphuis and Hall, 1983). Moreover, there are two representative modes of erosion, which are sandy and muddy erosion, in the mixture sediment condition with the transition stage where the dominant mode of erosion is changed from sandy to muddy erosion or vice versa (Mitchener and Torfs, 1996). However, the influence of the cohesive sediments on sediment transport has not been accounted for sufficiently in the wave fields.

This section examines and compares the influence of clay as a component in mud, kaolin used in the present study, on sediment transport using steady flow in open channel focusing on sediment transport rate. In addition, the characteristics of time-dependent topographic change in a constant sloping tidal flat composed of sand and

sand-clay mixtures are investigated in regular wave conditions. The modified critical Shields parameter considering cohesive effects presented in Chap. 4 is applied to the results of topographic change for analyzing the characteristics of sediment behavior in mixed soil condition. Last, the predictive capability of the numerical model proposed in Chap. 4 is examined with cohesive sediment effects based on experimental results in the case of a tidal flat composed of sand and clay.

5.2 Experimental Description

5.2.1 Open channel experiment

Pure sand (median grain size, $d_{50} = 0.26$ mm), sand-clay mixtures, and sand-steel slag mixtures (**Table 5.1**) were filled in a 1.0-m-long and 0.045-m-deep trench, and steady

Table 5.1 Sediment conditions for the open channel experiment.

	Sediments	p_f	ω	ω_t
Case 1	Pure sand	0.00	0.00	0.06
Case 2	Sand + kaolin	0.21	0.60	0.126
Case 3		0.10	0.60	0.06
Case 4	Sand + steel slag	0.50	0.00	1.00
Case 5		0.21		
Case 6		0.10		

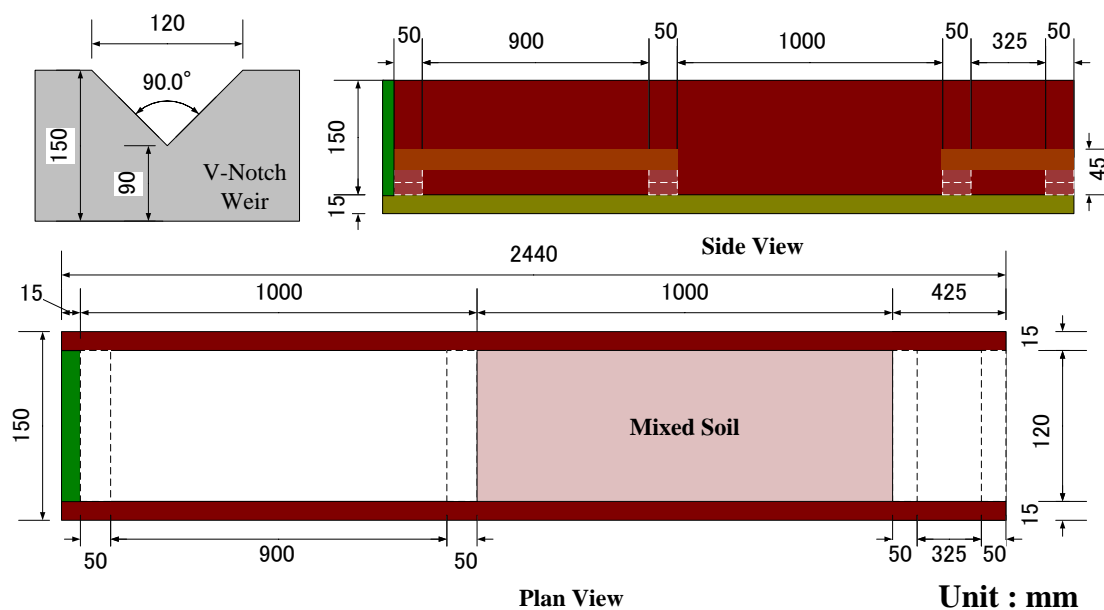


Fig. 5.1 Set-up for steady flow experiments.

flow was discharged for 90 s using a V-notch weir (**Fig. 5.1**). There are two different mechanisms between the sand-clay and sand-steel slag mixtures. The resistance forces against erosion are defined as the cohesive force in the sand-clay mixtures and the surface roughness effects in the sand-steel slag mixtures. In this experiment, the steel slag mixtures were used as a comparison test with cohesive effects in an order-of-magnitude difference. The content ratio of clay and steel slag, $p_f = w/(w_s + w)$, were 0.10, 0.21 and 0.50, in which w is the either clay or steel slag weight and w_s is the sand weight. Water contents were controlled using $\omega = w_w/w_c$ between Cases 2 and 3 for the effects of p_f based on the definition of cohesive force depending on the water content (Ashida *et al.*, 1982) in clay, and $\omega_t = w_w/(w_s + w)$ between Cases 1 and 3 for the effects of clay in the conventional definition of the water contents. Subscripts w and c indicate water and clay, respectively. Sand-steel slag mixtures were prepared by submerging for a few days for making hardening effects leading to an increase in surface roughness between steel slag and sand particles. The initial and final topographic profiles were measured in two lines with the ten measurement points per each line along the open channel using a digital point gage (KENEK, PH-340).

5.2.2 Wave flume experiment

It was a small scale wave flume of 16.50 m long, 2.22 m width and 1 m deep. The experimental domain with the length of 10.14 m and width of 0.40 m was set up by dividing the wave tank with connected partition boards. An initial tidal flat composed of pure sand ($d_{50} = 0.096$ mm) and sand-clay mixtures with a gradient of 1/20 and a crown width of 0.60 m, which is defined by the horizontal flat area of the tidal flat, was installed on a impermeable bed of the 0.4 m height based on the experiment in Chap. 2 as illustrated in **Fig. 5.2**. The constant sloping beach with the gradient of 1/20 was a sufficiently gentle slope as an initial equilibrium slope corresponding to the size of sand mainly consisting of the tidal flat due to the smaller angle than the repose angle of a submerged sand particle. Three different regular waves were generated against the tidal flat to investigate the effects of the variation of wave height and wave period on topographic change in the tidal flat (**Table 5.2**). Water surface elevations and flow velocities were measured using capacitance-type wave gages (KENEK, CHT6-30 and CHT6-40) along seven points ($x = -1.25, -1.00, 1.00, 1.50, 2.00$ and 2.25 m) and electro-magnetic velocimeters (KENEK, VM-801H) along two points ($x = 1.50$ and 2.00 m) for 0-1, 1-2, 30-31, 60-61 min, respectively, as shown in

Table 5.2 Experimental conditions for the wave flume experiment.

	Sediments	p_f	H_i [m]	T_i [s]
Case 7	Pure sand	0.00	0.019	1.0
Case 8			0.040	1.0
Case 9			0.026	1.6
Case 10	Sand + kaolin	0.20	0.040	1.0
Case 11			0.026	1.6

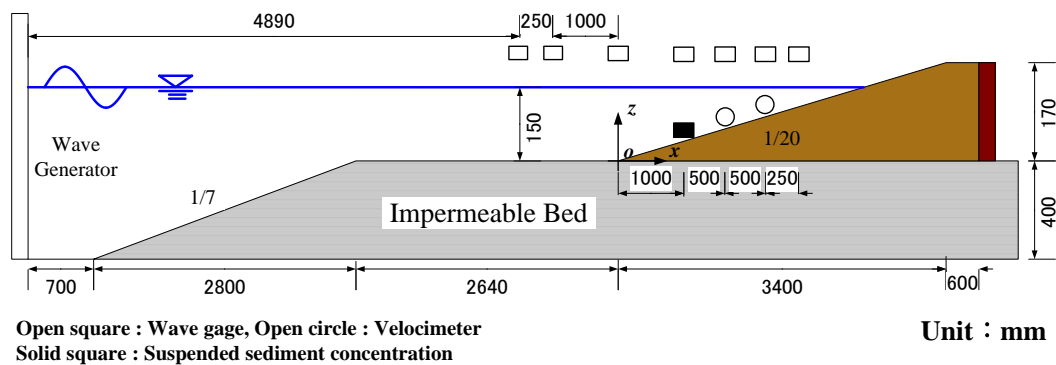
**Fig. 5.2** Set-up for wave flume experiments.

Fig. 5.2. The origin was located at the beginning of the tidal flat. In particular, the velocimeters were positioned 10 mm away from the surface of the tidal flat at each experimental time set at $t = 0, 1, 30$ and 60 min. The tidal flat profile along the center line of the flume was measured using a sand surface profiler (Masatoyo Instrument, Mt-E.P.I.-2) at $1, 30, 60$ and 300 min halting after the wave generation.

5.3 Sediment Transport in the Open Channel

The experiments for Cases 1-3 were carried out three times, in which six results of topographic change were obtained, and those for Cases 4-6 were performed twice with four data. Each measured data was averaged.

Sediment transport rate q (positive downstream) was calculated from bed evolution measurements using the standard form of the Exner equation of sediment mass balance (Parker *et al.*, 2000) assuming $q = 0$ at $x = 0$ where the beginning of bed as follows:

$$(1-m) \frac{\partial z}{\partial t} + \frac{\partial q}{\partial x} = 0, \quad (5.1)$$

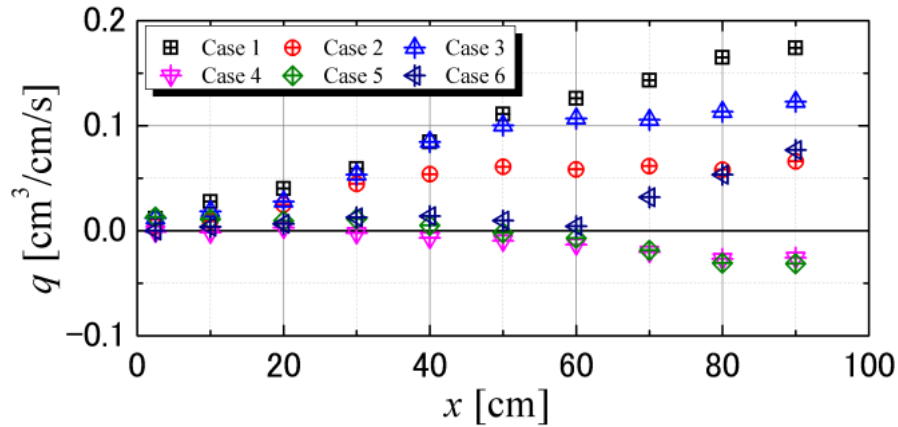


Fig. 5.3 Longitudinal averaged sediment transport rate computed from bed evolution measurements in Cases 1-6.

in which m ($= 0.40$) denotes the porosity; z denotes the bed elevation; and t denotes the time. In the analysis, ∂x and ∂t were simplified by Δx ($= 10$ cm) and Δt ($= 90$ s) respectively based on the experimental conditions.

The averaged sediment transport rates are depicted in **Fig. 5.3**. In the result for Case 1, erosive tendency was observed with the largest q downstream. With an increase in p_f of clay, the value of q decreased, particularly at $x \geq 50$ cm despite of similar tendency of q in the upstream side. It was rarely observed to be the separation of clay from the mixture bed mentioned by Mitchener and Torfs (1996) due to a relatively short experimental time, 90 s. This reduction trend of q attributing to cohesive effects was also shown in the results for Cases 4-6. As mentioned earlier, sand-steel slag mixtures depend on the influence of an increase in surface roughness different from sand-clay mixtures with cohesive effects.

The degree of reduction effects in q for the steel slag was larger than that for clay in the same p_f with the trend of sediment transport upstream for Case 5 (sand-steel slag mixtures) and downstream for Case 6 (sand-clay mixtures). Although it is difficult to characterize the trend of q for the mixtures due to the variability of topographic change in each case due to non-uniform flow triggered by initial topography, the degree of the cumulated sediment transport rate is meaningful to understand the influences of clay and steel slag on sediment transport. From the results for Cases 5 and 6, q decreased with an increase in p_f of steel slag, whereas there was little change for Case 4 in spite of an increase of 0.3 in p_f than that of Case 5. This result implies that although the effects of steel slag show a prominent reduction

in q rather than clay, it seems to be an optimal value of p_f to decrease q similar to the trend of cohesive sediment mixtures (Mitchener and Torfs, 1996). However, the limited number of the experimental bases requires additional experiments for steel slag mixtures to reveal steel slag effects on sand-based bed or structures.

5.4 Results in the Wave Flume Experiment

The evolution of the tidal flat with time is presented for three cases of sandy tidal flats and for two cases of sand-clay mixture tidal flats. The influence of cohesive sediments on topographic change is discussed with the signed Shields parameter presented in Chap. 2 calculated from the measured flow velocity data at the two points ($x = 1.50$ and 2.00 m).

5.4.1 A tidal flat profile evolution

Cross-shore distributions of tidal flat profile z and topographic change Δz , in which positive sign means accretion, with time for five cases are illustrated in **Fig. 5.4**. The gray vertical dashed lines mean the initial crown position of the tidal flats, and the dark blue dash-dot lines indicate the still water levels. The results of non-dimensional wave height H/H_i and mean water level η/H_i were defined by the averaged three wave heights that were adopted in the stabilized state after wave generating at five points above the sloping tidal flat.

For the sandy tidal flat cases, it was observed that the crown of the tidal flat and shoreline were retrogressed in the final profiles defined by the profile at $t = 300$ min in this section. Specifically, there are shoreline retrogressions of approximately 0.31, 0.48 and 0.30 m for Cases 7, 8 and 9, respectively, away from the initial shoreline in the landward direction. The significant topographic change was appeared from $t = 30$ min, blue solid lines for all cases in **Fig. 5.4**, and it shows the tendency of the structure of sequent erosion and accretion in the seaward direction which seemed to be established by the process of the interaction between breaking waves and backwash (Kemp, 1960). These erosion and accretion were elongated and deepened landward and seaward respectively, from the boundary between erosion and accretion built at $t = 30$ min besides Case 9.

The result for Case 9 shows the separated two accretions on the lower sloped tidal flat with the length of about 0.78 m that is smaller than a half of the wave length.

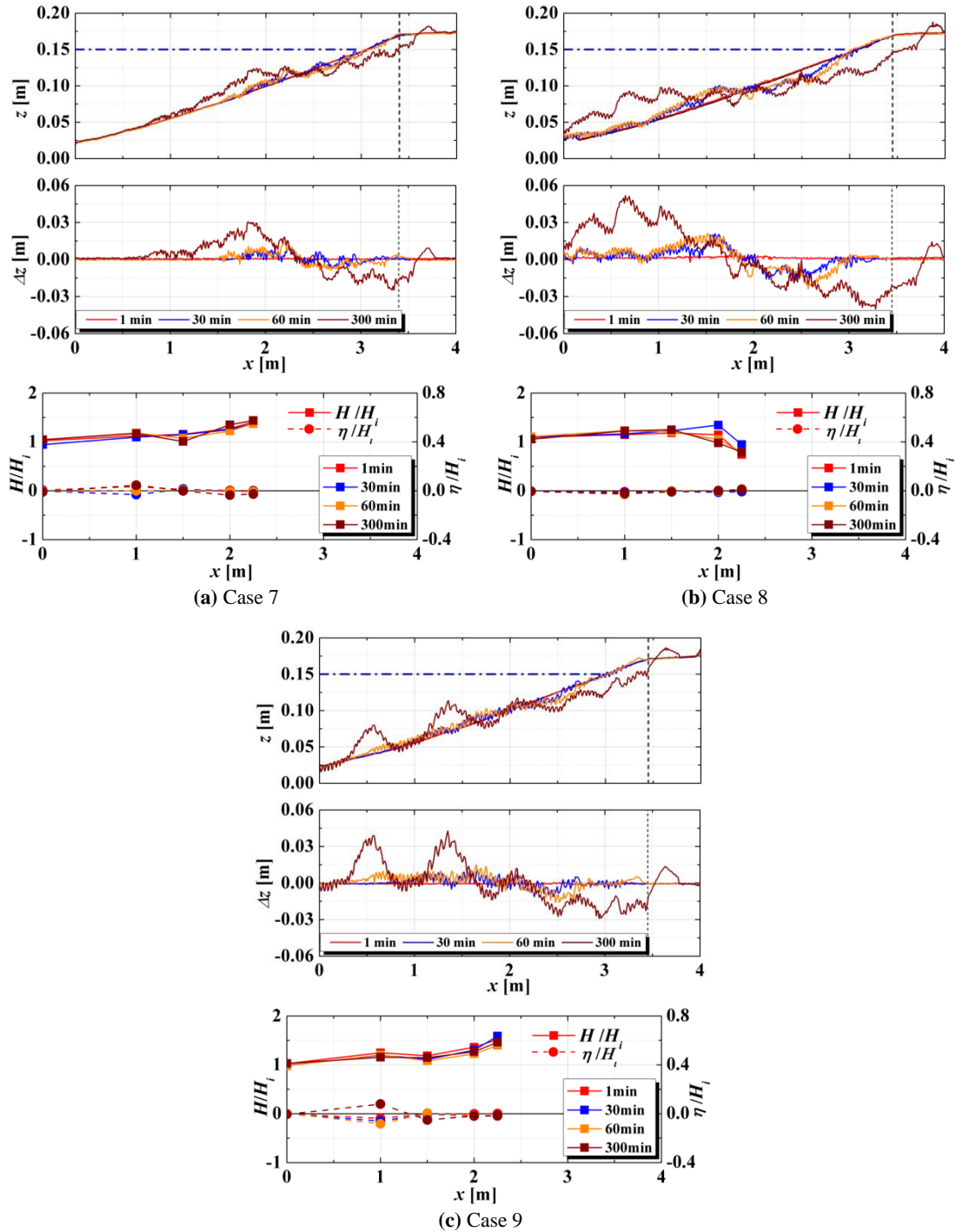


Fig. 5.4 Cross-shore distribution of: tidal flat profile z (upper); topographic change Δz (middle); and non-dimensional wave height H/H_i and mean water level η/H_i (lower) at experimental time $t = 1, 30, 60$ and 300 min.

This kind of topographic change seems to be the result from wave period, *i.e.*, wave length. Relatively long waves can entrain a larger volume of sediments on the bed away from the tidal flat where x is negative to the sloping tidal flat. There were a small volume of sediments on the bed in the offshore area before experimental set up because of the difficulties to clean up the sediments completely. Thus, the supply of

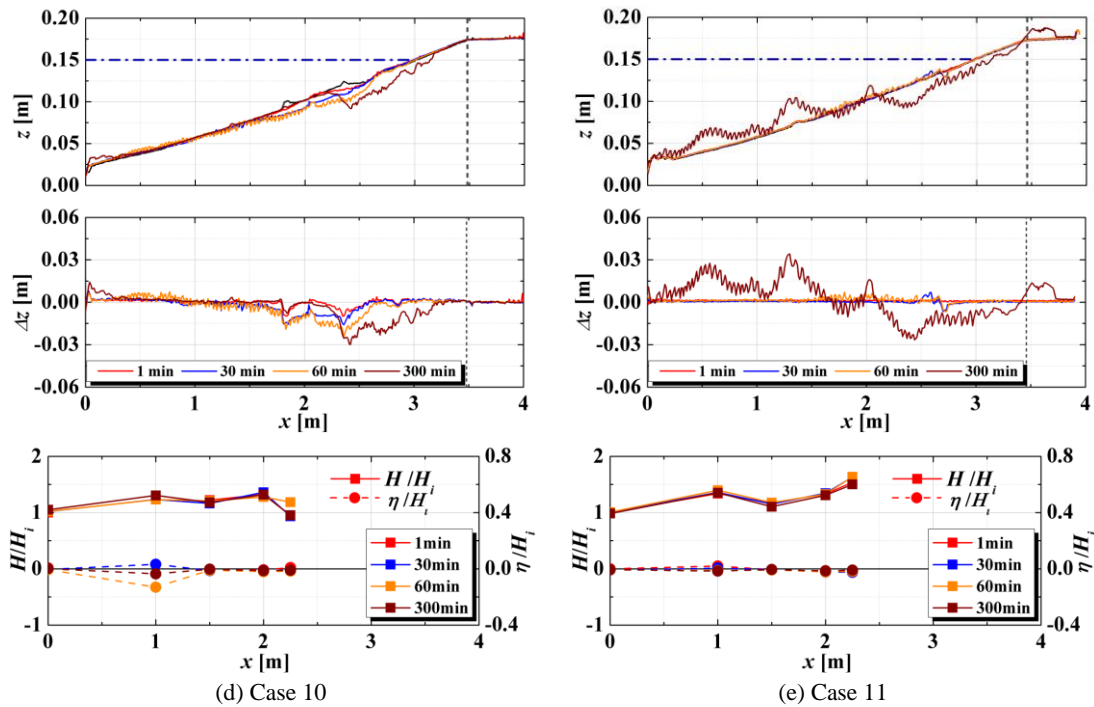


Fig. 5.4 (Continued).

the sand from offshore was able to contribute to one of the accretion in the seaward direction. In addition, another possibility can be considered to the formation of the separated accretions. That is the interaction between the bottom flow generated by backwash and approaching waves at the two points where the accretions appeared. These two flows first encountered at the region near the accretion formed landward and the backwash decreased the energy of approach waves, *i.e.*, bottom velocity, resulting in accretion. However, different from other cases, the offset of wave energy was appeared over a wide area for Case 9 with the occurrence of the formation of accretion ranging $x = 0-1.80$ m (see the results for z and Δz at $t = 60$ min, the yellow solid lines). It implies that backwash is strong enough to influence the area far away from the shoreline when the wave period is longer. Consequently, the separation of the accretion was considered to be taken place in the process of the transition to the fully developed topographic profile called as equilibrium state by decreasing momentum between incident waves and backwash under the wave condition as stated earlier (Kemp, 1960) and the aforementioned supply of sand from offshore.

The formation of the ripples characterized by the representative sediment transport of non-cohesive sediments is observed from $t = 30$ min with the waved lines of the topographic profiles in the entire cases for the sandy tidal flats. From the results

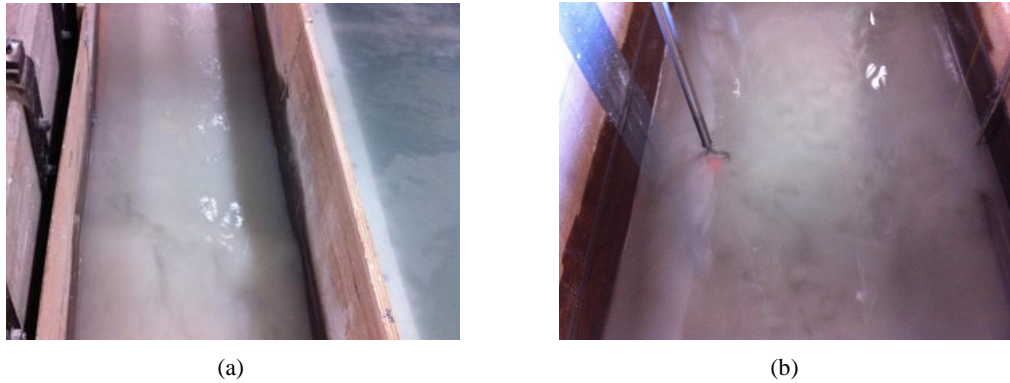


Photo 5.1 Visual observation for: (a) Case 10; and (b) Case 11 during $t = 1-10$ min.

H/H_i , each wave breaking point is predicted after $x = 2.25$ m for Cases 7 and 9, and near $x = 2.00$ m for Case 8. In particular, the highest value of H/H_i for Case 8 moved to seaward after $t = 60$ min corresponding to topographic change. That is, the higher waves seem to be more sensitive to the bed topography. As the erosion and accretion took place generally in the surf zone, the experimental results for Cases 7-9 show the correspondence to the conventional trend of topographic change. Most of the results of η/H_i increased with a decrease in H/H_i and decreased with an increase in H/H_i with small quantities, while at $x = 1.00$ m where the trough area between two crest accretions for Case 9, relatively large variations are observed.

On the other hand, the topographic change for sandy tidal flats with clay shows significantly different trends. Little change near the shoreline for Case 10 and the advanced crown of about 0.04 m with the accretion piled up offshore for Case 11 are observed at the final tidal flat profile. The tidal flat evolution with time for Case 10 shows substantial erosion in the initial stage at $t = 1$ min without ripples, which are confirmed by the little waved line and the visible observation in the laboratory experiments. This abnormal erosion was arisen from the extruded initial topography ranged from $x = 1.80-2.50$ m. Although the significant erosion on the sloping tidal flat is shown, there is relatively small topographic change after $t = 1$ min compared with Case 8. There is no successive accretion after erosion in the seaward area, *i.e.*, eroded sediments were migrated seaward besides the beginning of the slope where the small volume of accretion was formed. In addition, the remarkable topographic change is the waved topographic profile on the lower sloped tidal flat ($x \leq 2.00$ m) at $t = 60$ min, which indicated the ripple formation. This result was due to the loss of clay gradually washed away from the surface of the tidal flat during the experimental time, thus the

influence of cohesive effects was vanished. The loss of the clay in the surface of the tidal flat was confirmed by murky water in the wave flume from the initial stage of the experiments as shown in **Photo 5.1(a)**. Consequently, the behavior of sediment transport was likely to be the same as that in the clay-free condition with ripple formation. This clay-free sediment transport shows at $t = 60$ min. Moreover, there was the disappeared ripple structures formed at $t = 300$ min from the smoothed brown solid line in **Fig. 5.4(d)** except for the eroded area in the final tidal flat profile. It was difficult to describe this phenomenon in the present experiment. However, it is clear that for Case 10, the initial topography of the tidal flat and the effects of cohesive sediments had a great effects on the topographic change, thus substantially different tendency of topographic change is shown from Case 8.

In the results of Case 11, the hydrodynamic characteristics on the sloping tidal flat show the similarity to Case 9 as shown in the results of η/H_i and H/H_i (**Fig. 5.4(d)**). The evolution of topographic change for Case 11 shows little topographic change until $t = 30$ min. After $t = 30$ min, a little topographic change occurred, while a number of ripples, which were rarely observed in the advanced time step, are observed on the sloping area with the similar process to the results for Case 10. The final topographic profile shows the similar trend to that for Case 9. However, the crown migration of the tidal flat is noticeably different, *i.e.*, the crown was advanced for Case 11 despite of the shoreline retrogression of 0.13 m. The final profiles presented in Cases 9 and 11 were not equilibrium states and it was difficult to decide that the final profiles of the Cases 9 and 11 are under either a reversible or irreversible state due to the relatively shorter experimental time of 300 min than the minimum time of 40 hour as mentioned in Sunamura and Horikawa (1974). On the other hand, the countered crown migrations show the possibility to affect the trend of topographic change by containing clay. Consequently, cohesive sediments presented in the tidal flat not only increased the erosion resistance in the early stage, but also showed the possibility of influences on the tendency of the topographic change when the tidal flat is exposed to waves for longer experimental time.

As described in Chap. 2, the C_s value proposed by Sunamura and Horikawa (1974) is applied to the results of topographic change and evaluated the trend of topographic change in the different wave conditions with the two types of the tidal flats. **Table 5.3** shows the C_s value in the experimental conditions. The overall

Table 5.3 C_s values for Cases 7-11.

Case	C_s	Type
7	4.06	Transitional type
8	8.54	Erosion type
9	4.65	Transitional type
10	8.54	Erosion type
11	4.65	Transitional type

displacement of the final shoreline change from the initial tidal flat are retrogressions of 0.31 m for Case 7, 0.48 m for Case 8, 0.30 m for Case 9, 0.15 m for Case 10 and 0.135 m for Case 11. Although Cases 7, 9 and 11 show the erosion type despite of the transitional type based on the C_s value, it is within the permissible range. Sunamura and Horikawa (1974) showed that in the range of transitional type, erosion type and transitional type coexisted on the basis of the experimental results implemented by other researchers. However, the accumulated sediments on the crown of the tidal flat provided from the erosion area can be classified by either deposition type or transitional type from the definition of them.

These accretions on the crown except for Case 10 were arisen from the incomplete beach. The structures used in this experiment were the tidal flats with the crown. The existence of the crown was able to make sediments, which are climbing up along with the sloping tidal flat entrained by the flows swashing up after wave breaking, accumulate easier than normal beaches with a successive constant slope. Furthermore, the size of the accretion formed on the crown was a negligible quantity compared to the accretion on the sloping tidal flat. For Cases 10 and 11, it does not make sure that the evaluation of the tidal flat profile using the C_s value can apply to the tidal flat since the C_s value rarely includes any cohesive effects. However, in this experiment, the applicability of the C_s value to the tidal flat containing clay was confirmed due to the phenomenon of the loss of the cohesive sediments with experimental time. Therefore, by using the beach profile classification based on the C_s value, the transformation of the tidal flat composed of only sand as well as mixed soil can be predicted.

5.4.2 Evaluation of signed critical Shields parameter

To evaluate sediment transport, fluctuating signed Shields parameters with time φ_d (positive landward) are presented in **Fig. 5.5** calculated from the flow velocities at

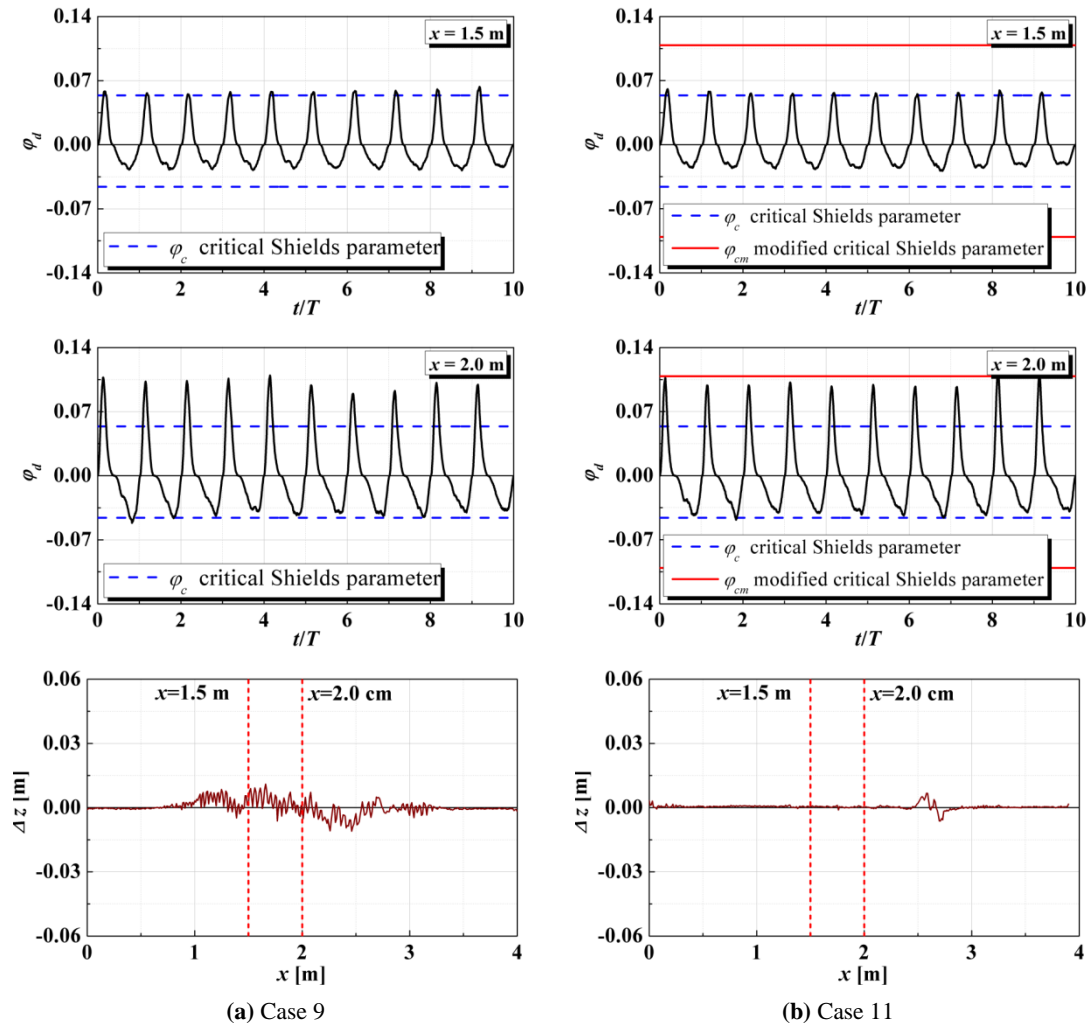


Fig. 5.5 Time distribution of signed Shields parameter φ_d at $x = 1.50$ m (upper) and 2.00 m (middle) during $t = 1$ - 30 min and topographic change Δz (lower) at $t = 30$ min.

$x = 1.50$ and 2.00 m together with the topographic change Δz during 30 min in Cases 9 and 11 using:

$$\varphi_d = \frac{u_* \cdot |u_*|}{(\rho_s / \rho_w - 1) g d_{50}}, \quad (5.2)$$

in which u_* is the friction velocity defined as positive landward; ρ_s and ρ_w are the densities of sand particles ($= 2.65 \times 10^3 \text{ kg/m}^3$) and water ($= 0.9970 \times 10^3 \text{ kg/m}^3$); and g is the gravitational acceleration ($= 9.81 \text{ m/s}^2$). The value of u_* was calculated from the measured velocities near bottom based on the logarithmic velocity profile (Parker *et al.*, 2000). The velocity data was adopted after ten waves generated so that the stable velocity data was available. According to φ_d , the traditional signed critical Shields parameter φ_c were adopted to be 0.0539 and 0.0460 in the landward and seaward

direction respectively using the following equation (Kawata, 1989; Nakamura and Yim, 2011):

$$|\varphi_c| = (\cos \beta \mp \sin \beta / \mu_s) \varphi_{c0}, \quad (5.3)$$

in which φ_{c0} ($= 0.05$) is the critical Shields parameter for a horizontal bed; β is the angle of bed slope; μ_s is the static friction coefficient ($= 0.63$) related to the repose angle of a submerged sand particle ϕ ($= 32.2^\circ$); and the signs of + and - in Eq. (5.3) correspond to the landward and seaward directions.

From the results with φ_d (black solid line) and φ_c (blue dotted lines) for Case 9, there is relatively small φ_d slightly larger than φ_c at $x = 1.50$ m with accretion in the results of Δz , and the value of φ_d periodically exceeding landward φ_c is observed at $x = 2.00$ m (middle in **Fig. 5.5(a)**), corresponding to the erosion at $t = 30$ min (right in **Fig. 5.5(a)**). This estimation with the traditional critical Shields parameter in sediment transport shows good agreement with Δz for Case 9. However, from the results for Case 11 (**Fig. 5.5(b)**), there is little change in Δz despite of the expectation of the erosion at $x = 2.00$ m due to φ_d frequently exceeding φ_c . This result implies that the parameter considering cohesive force of the present clay is required to accurately evaluate sediment transport in mixed soil condition with cohesive sediments. In this section, the modified critical Shields parameter φ_{cm} derived from the force balance for a sand particle with cohesive force as resistance force in the condition of clay filling in the pore of sand as shown in Chap. 4 is applied as the following equation:

$$|\varphi_{cm}| = \frac{(\mu_s \cos \beta \mp \sin \beta)W + F_c}{\mu_s W} \varphi_{c0}, \quad (5.4)$$

in which $W = 1/6\pi(\rho_s - \rho_w)gd_{50}^3$ is the submerged weight of the particle; and F_c ($= 0.052$ N) is the cohesive force with the cohesive resistance force per unit surface area f_c ($= 5.0$ N/m²). As a result, the increased critical Shields parameters (red solid lines in **Fig. 5.5(b)**) were obtained as 0.1087 landward and 0.1008 seaward, resulting in a decrease in φ_d exceeding φ_{cm} with the less incipient sediment transport, which is corresponding to the results of Δz as shown in **Fig. 5.5(b)**. The proposed φ_{cm} shows better agreement with the topographic results, thus, to consider cohesive force in the critical Shields parameter is suggested for better evaluation of sediment transport in mixed soil structures with cohesive sediments.

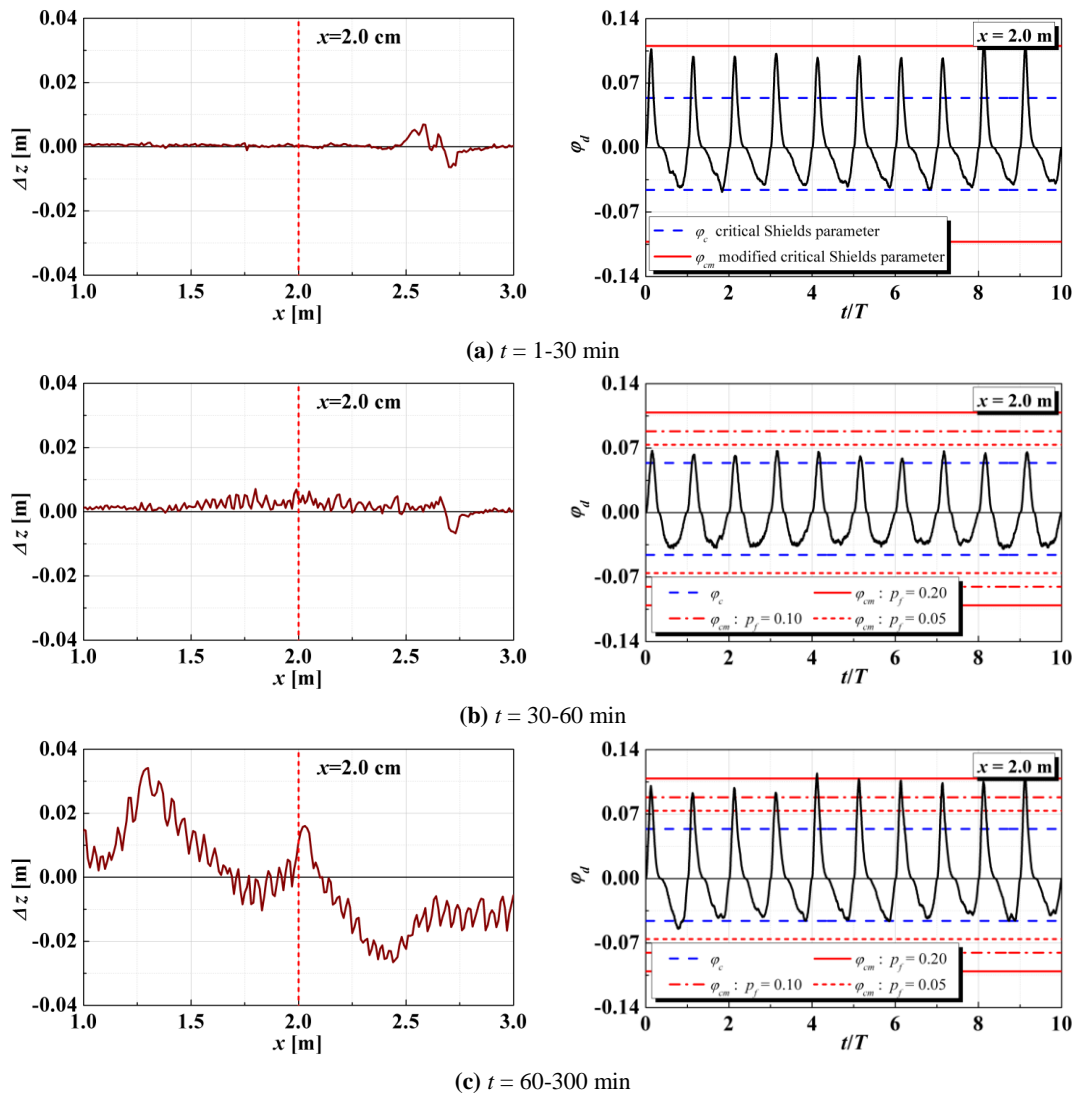


Fig. 5.6 Topographic change Δz and time distribution of the signed Shields parameter φ_d at $x = 2.00$ m with the modified critical Shields parameter φ_{cm} for Case 11 during $t = 1-30$ (upper), $30-60$ (middle) and $60-300$ min (lower).

The modified critical Shields parameter φ_{cm} considering cohesive effects is also applied to the prediction of the degree of the loss of the clay during the experimental time. **Figure 5.6** shows topographic change and time distribution of the signed Shields parameter φ_d at $x = 2.00$ m during $t = 1-30$, $30-60$ and $60-300$ min with the modified critical Shields parameter φ_{cm} for Case 11. The blue dotted lines and red solid lines indicate the typical critical Shields parameter φ_c and the modified critical Shields parameter φ_{cm} , respectively. At $t = 30$ min, aforementioned little topographic change shows better correspondence to φ_{cm} assuming $f_c = 5.0 \text{ N/m}^2$ in inverse operation to adjust the experimental results. The value of f_c is discussed minutely in Chap. 6. During the experimental time, Shields parameter φ_d relevant to the flow

velocity near the bottom decreased due to the influence of the evolved topography accompanied with the accretion over a wide range on the sloping tidal flat as shown in **Fig. 5.6(b)**. The formation of the wide ranged accretion resulted from the some factors as described above. Furthermore, in the results of φ_d at the same experimental period, the value of φ_{cm} seems to be overestimated because φ_d fluctuated under φ_{cm} . In particular, during $t = 30-60$ min, a few formations of the ripple on the tidal flat is observed in the results of the topographic change, which are not rarely showed in the former stage. It means that the clay was washed away and it resulted in the non-cohesive sediment behavior, thus the initial content ratio of the clay p_f on the surface of the tidal flat is not suitable to evaluate sediment behavior. In **Fig. 5.6(b)**, the values of φ_{cm} with decreased p_f , 0.10 and 0.05, are depicted. The red alternate long and short dash lines are φ_{cm} with $p_f = 0.10$ and the red dotted lines are φ_{cm} with $p_f = 0.05$. Despite of the decrease of p_f , φ_{cm} for $p_f = 0.05$ is still above and under φ_d . That is, in the experimental time step, the degree of the loss of the clay on the surface of the tidal flat can be predicted by $p_f = 0.05$ or less. Though the cohesive effects on the surface of the tidal flat decreased due to the loss of the clay, the cohesive force by remained clay was enough to have resistance force to relatively declined φ_d and led to accretion around $x = 2.00$ m. The existence of the clay on the surface of the tidal flat can be confirmed by the result of the blue dotted lines that indicate φ_{cm} without cohesive effects because the erosion was predicted due to the frequently exceeding φ_d .

At $t = 300$ min, significantly changed topography and increased φ_d are shown in **Fig. 5.6(c)**. The increased φ_d seems to mainly attribute to the topography with accumulated sediments in front of the measuring point ($x = 2.00$ m). From the final Δz , the accretion was more effective than the erosion despite of the large φ_d . This result was caused by several factors. First, φ_{cm} for $p_f = 0.05$ as well as 0.10 predicted in the former time step is unsuitable to evaluate sediment transport due to considerably large φ_d inducing erosion dissimilar to the results of Δz . Considering the results of φ_d , larger φ_{cm} is required with larger p_f . However, in the former step, the loss of the clay was observed, which indicates the surface of the tidal flat with less cohesive sediments. Therefore, reattached clay, once swept away, can be considered. Another possibility is the occurrence of the less loss of the clay at $t = 30-60$ min ranging $p_f = 0.10-0.20$ that make the evaluation of φ_d with φ_{cm} better. The other factor is the balance of the loss

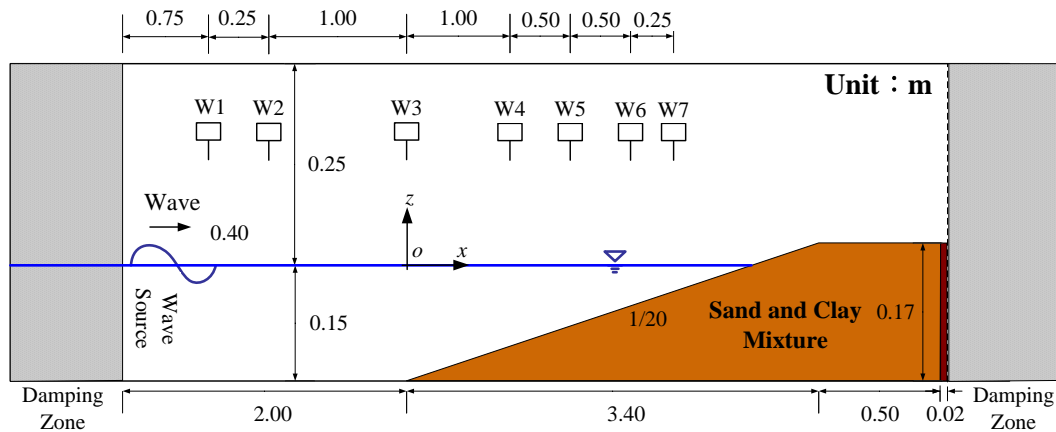


Fig. 5.7 Schematic of the computational domain for topographic change in the tidal flat.

and supply of the sediments covering the whole area on the sloping tidal flat. The location at $x = 2.00$ m is on right after the erosion area occurred in the upper slope of the tidal flat. The eroded sediments entrained back to the offshore and some parts of the sediments are reattached during traveling in this procedure. In addition, there are entrained sediments by approaching waves from the offshore side out of the range of the experimental domain. The accretions taking place in the lower part of the slope (Fig. 5.4(e)) seem to be the results of this procedure of the supply system of the sediments. Consequently, at $x = 2.00$ m, the amount of accretion was larger than that of erosion arisen from local ϕ_d . Though, in the experimental results, it is hard to verify what kind of factors are dominant, it is clear that the modified critical Shields parameter shows the possibility to evaluate the sediment transport in a mixed soil condition and predict the degree of the loss of the cohesive sediments.

5.4.3 Application of the modified sediment calculation

The predictive capability of the sediment calculation considering cohesive effects proposed in Chap. 4 is investigated in this section. Figure 5.7 shows the computational domain based on the same dimension as the experimental domain for Case 11. On the impermeable horizontal bed with non-slip condition, a tidal flat with a 0.17 m high and 3.40 m long sloping beach with a gradient of 1/20 and a 0.17 m high and 0.50 m wide crown composed of fine sand with a median grain size, $d_{50} = 0.096$ mm, and kaolin. The domain of numerical simulation of $-2.00 \leq x \leq 3.92$ m and $-0.15 \leq z \leq 0.25$ m is discretized using orthogonal staggered cells with a uniform size of $\Delta x = 1.00$ cm and $\Delta z = 0.50$ except for damping zones located on the both ends

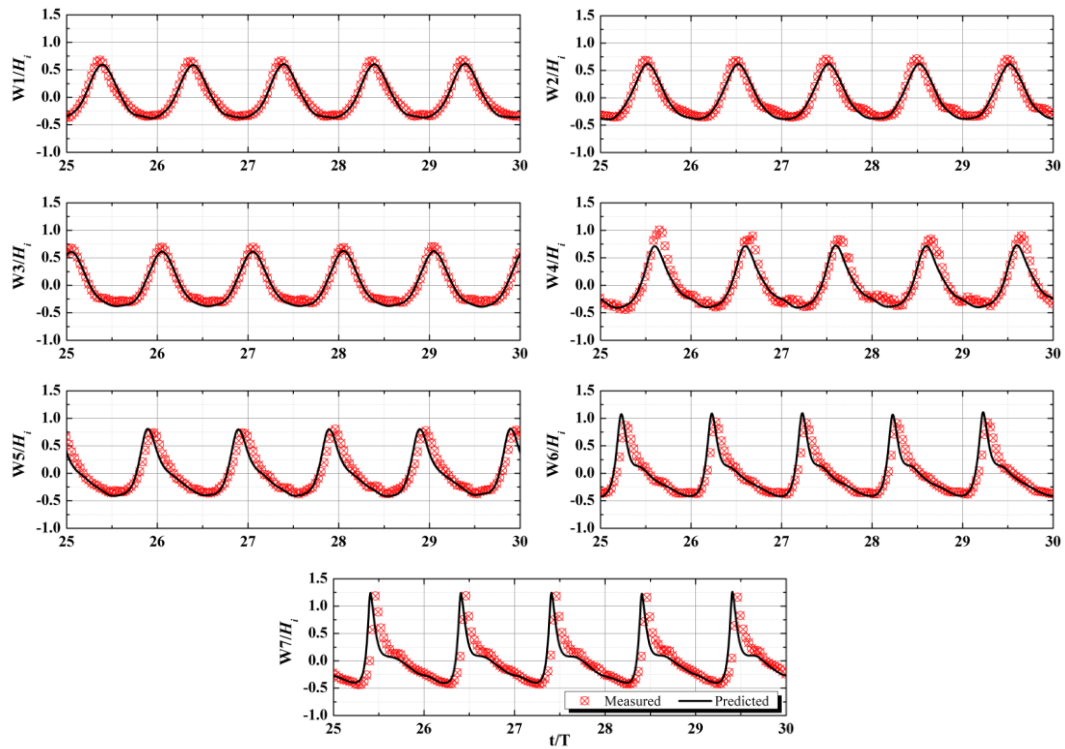


Fig. 5.8 Time series of non-dimensional water surface elevation against incident waves H_i predicted at W1, W2, W3, W4, W5, W6 and W7 during 1 min.

of the domain. In the damping zones, non-uniform cells that are widening gradually for dissipating waves effectively and reducing the computational efforts were used. The length of the damping zones were longer than about four times an incident wave length at seaward to minimize reflection waves from the tidal flat and the end of the seaward boundary and smaller than that at landward due to a free of reflecting waves. Wave generating source was set at the boundary between the damping zone seaward and the main domain. Regular waves were generated with a wave height $H_i = 0.026$ m, a wave period $T = 1.6$ s, and a still water depth $h = 0.15$ m. The parameters relevant to cohesive force were adopted by $f_c = 5.0$ N/m², $\omega = 1.0$ and $p_f = 0.2$ corresponding to the aforementioned condition in Section 5.4.2. The critical Shields parameter on the horizontal plane was used by $\tau_{*c0} = 0.05$. Other numerical parameters were identical to Chap 4. The numerical simulation was carried out for 1 min.

Figure 5.8 shows the results of non-dimensional water surface elevation predicted at W1-W7 for 5 waves after 25 waves generating. In the figures, the black solid lines are the predicted results and the circles with the mark are the measured data from the experiments for Case 11. The predicted results show good agreement

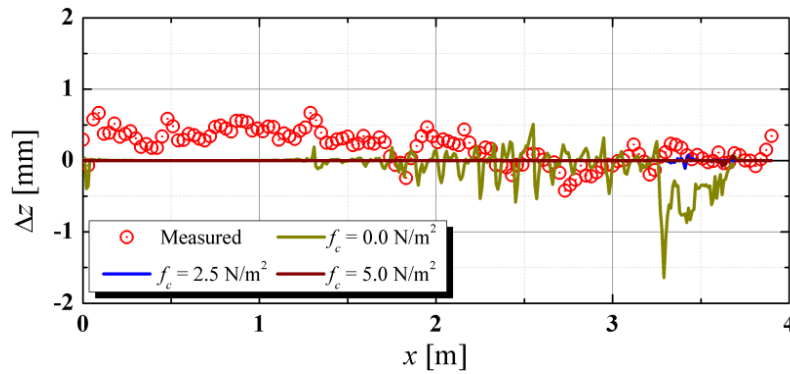


Fig. 5.9 Cross-shore distribution of topographic change Δz with comparison between the measured data and the predicted results for $f_c = 0.0, 2.5$ and 5.0 N/m^2 .

with the measured data except for the results at W4, in which the predicted results underestimated as shown in **Fig. 5.8**. The measured data at W4 shows somewhat increased water surface elevations compared to the results at W3 and W5 estimated. The abnormal measured data results from the mechanical problem at wave gage W4. In the entire measured data of the water surface elevation at W4 that is not presented in this section, the data showed unstable measurements during $t = 0-1$ min presenting a rise in mean water level and irregular wave heights. At W5-W7, although the crest and trough of the waves were predicted well, somewhat phase shift is observed in the predicted results. The phase of the predicted results becomes faster than the measured data. This phase shift is not arisen from the hydraulic phenomenon such as wave breaking or the interaction between approaching waves and backwash flows since this result was showed at the beginning of the waves first approaching. There are two assumptions in this discrepancy. One is that the measuring point in the experiments was a little dislocated at W5-W7 because the difference of phase is very small. Another assumption is a bit difference of wave period between the experiment and the simulation. The latter cause is difficult to be confirmed from the results due to a relatively short simulation time. However, since the discrepancy of the phase of the waves is too small to influence the other results such as topographic change, the predicted results can be considered to be reasonable to the measured data.

The cross-shore distribution of topographic change Δz is depicted in **Fig. 5.9** with the three predicted results for $f_c = 0.0$ (light green solid line), 2.5 (blue solid line) and 5.0 N/m^2 (brown solid line). In the measured data, a small volume of the accretion over a wide range at $x = 0-1.80$ m and the disturbed topographic profile on the upper

part of the tidal flat including the crown. The accretion that is not occurred in the predicted results seems to be formed from the aforementioned supply of the sediments placed on the impermeable bed of the flow channel out of the range of the experimental domain because of the contrary results of the mass balance of the sediments between accretion and erosion as shown in **Fig. 5.9**, in which there is little erosion in the entire domain. An additional possibility of the results in the accretion is the way of measuring topographic profile. In this experiment, the topographies were measured when wave fields were stabilized after wave generating was ceased. However, disturbed sediments on the surface of the tidal flat apt to slightly float than the initial profile that was measured waiting for enough time after installation of the tidal flat for a day. In this process, in the initial profile, enough natural consolidation could be progressed, whereas there was lack of time to expect natural consolidation in the profile after wave generating for 1 min, which was measured at 10 min after wave fields were stabilized. In addition, the lower part of the sloping tidal flat experience the lower effect of compaction induced by breaking waves than the upper part of the tidal flat on which the surf zone is located. Therefore, this wide ranged accretion can be negligible.

In the predicted results, disturbed topography on the upper part of the tidal flat is shown for the results for $f_c = 0.0 \text{ N/m}^2$, while the results for $f_c = 2.5$ and 5.0 N/m^2 present little topographic change over the entire computational domain with slight erosion occurred near $x = 3.40\text{m}$ for $f_c = 2.5 \text{ N/m}^2$. Comparing the measured data showing the disturbed topography on the upper part with a little volume, the predicted results for $f_c = 5.0 \text{ N/m}^2$ estimated for evaluating the sediment behavior with φ_{cm} shows the more stabilized tidal flat with little topographic change except for the area where very small erosion of about 0.05 mm took place on the same location of the erosion occurred in the case for $f_c = 2.5 \text{ N/m}^2$. Despite of a decrease in the cohesive force up to $f_c = 2.5 \text{ N/m}^2$, the similar trend of topographic change is observed. The calculation considering cohesive effects seems to give the better prediction than that of non-cohesive effects ($f_c = 0.0 \text{ N/m}^2$) because the erosion occurred in the result for $f_c = 0.0 \text{ N/m}^2$ is vulnerable to the next approaching waves. These eroded areas are able to accelerate consecutive erosion as show in Chap. 3 unlike the measured results with little erosion on the upper part of the tidal flat. Therefore, although the improvement of the proposed model considering cohesive effects is required for

accurate prediction, the possibility of application to the mixed soil condition is confirmed.

5.5 Remarks

The influence of cohesive sediments on topographic change has been presented using the open channel and wave flume experiments. The results of the averaged sediment transport rate q in the open channel tests demonstrated that not only the increase in the content ratio p_f of clay decreased q , but the increase in p_f of steel slag showed reduction tendency of q with different mechanism. The reduction effects of q by cohesive force were smaller than that by surface roughness and it seems to be optimum p_f between 0.21-0.50 for steel slag.

Containing clay in the tidal flat structure led to the increase in erosion resistance contributing to the less topographic change without ripple formation as well as less shoreline displacement with the different tendency of topographic profile. It seemed to be difficult to investigate the effects of cohesive force on topographic change for relatively long time because of the phenomenon of clay washing away after the onset of erosion. The proposed modified critical Shields parameter considering cohesive force offered better evaluation of sediment transport in the mixed soil condition. Moreover, it is confirmed that by applying the modified critical Shields parameter, the degree of the loss of the clay is able to be predicted indirectly with the parameter of p_f . In the numerical study, the possibility of the application of the proposed calculation considering cohesive effects in mixed soil condition was confirmed with the necessity of the improvement. Thus, it was suggested that the cohesive effects should be taken into account in the evaluation of topographic change in mixed soil such as dredged sand.

Chapter 6

CONCLUSIONS

The progress of scientific technologies in various fields in recent decades has not only improved the quality of human life, but caused a lot of concerns drawing diverse problems in effective managements and applications for retaining the current system. Dredging is one of the salient issues accompanying with a heavy volume of dredged soil induced by periodic dredging works. The advanced research within a decade showed the applicability of dredged soil to costal structures composed of dredged sand such as a tidal flat and shallows with the positive influence in marine environment (Kazama *et al.*, 2006). However, dredged soil generally excavated in fluvial and nearby sea contains a large quantity of fine sediments, particularly cohesive sediments with the occupation ratio of 62% to total dredged soil (Japanese Ministry of Land, Infrastructure, Transport and Tourism, 2010). Thus, the stability of the structures is concerned against approaching waves. Advanced related researches have been implemented on the sediment problem of either cohesive or non-cohesive sediments due to considerably different characteristics. However, for the evaluation of the stability of the structures made by dredged sand, understandings of cohesive forces in mixed soil condition is required, particularly in wave fields. To achieve the subject, the author fulfilled experimental and numerical investigations of the behavior of sediment transport in shallows and a tidal flat composed of fine sand and sand-clay focusing on wave-induced topographic change. In this chapter, the author gives an overview of not only main conclusions, but also perspective and recommendations in regard to the present study for further studies in future.

Dredging produces large volumes of not only cohesive sediments, but also sand. In Chap. 2, the hydraulic experiments of artificial shallows composed of fine sand

were modeled based on the Froude similarity law with a length scale of 1/20 targeting the earth structure composed of dredged sand installed in Mikawa Bay. The characteristics of wave-induced topographic change in artificial shallows were examined. Although the soil structures were the shallows in this experiment, the classification of the final topographic profile to evaluate the trend of the final beach profile (Sunamura and Horikawa, 1974) was able to apply the evaluation of the characteristics of topographic change under the cases with shallower water depth on the crown of the shallows. Since the fine sediments are sensitive to pore-water pressure variation due to relatively low weight, the effects of pore-water pressure on topographic change were examined. The results showed that the relative vertical effective normal stress ratio calculated from pore-water pressure was negatively correlated with the signed Shields parameter defined as positive landward. Its relationship was unchanged despite a change in the surface profile of the shallows. It implied an increase in seaward sediment transport and a decrease in landward sediment transport. Furthermore, the modified signed Shields parameter considering the effects of pore-water pressure gave a reasonable evaluation of the trend in the sediment transport for $d_{50} = 0.1$ mm. These results showed that the consideration of the pore-water pressure effects is underlined when discussing the sediment transport of fine sand such as dredged sand.

The experiments related to sediment problems of fine sediments has many limitations to adjust an experiment scale based on the law of similarity and obtain limited data due to a costly apparatus and laboratory condition. With the computer technology development, numerical analysis is the best alternative. In Chap. 3, the coupled fluid-structure-sediment interaction model (FSSM) developed by Nakamura and Mizutani (2010) was applied to the laboratory experiments implemented in Chap. 2 to investigate the predictive capability of the model based on wave-induced topographic change in shallows composed of fine sand. It was found that excessive erosion in the predicted results was occurred over the shallows for the same still water depth as the experimental condition, which was a different trend from the measured data. In contrast, a small increase in the still water depth of the numerical condition improved the computational accuracy of the water surface elevations, pore-water pressure and final topographic change in the shallows. The variation of mean water level in the experiments was confirmed in the simulation on the basis of the

comparison of the results of water surface elevation between the predicted and measured data. From the results, since the varied experimental condition during experimental time was able to induce discordance between numerical and experimental results, the careful attention in the variation of experimental conditions was recommended. Moreover, the predictive capability of the model was verified in terms of wave field as well as wave-induced topographic change in the initial stage.

Dredging sand contains a volume of cohesive sediments, thus cohesive effects in mixed soil condition should be examined for the analysis of the stability problem of dredged sand structures. In Chap. 4, the modified sediment transport calculation considering cohesive effects was proposed to deal with the behavior of mixed soil including cohesive sediments. In the proposed calculation, each sand particle was assumed to be surrounded by a thin layer of clay and cohesive forces were operated as resistance forces in a force balance on a sand particle (Ashida *et al.*, 1982). The critical Shields parameter and bed load sediment transport rate in FSSM were modified to apply the cohesive force acting on the sand particles. The characteristics of the calculation showed the cohesive force increases resistance against flows as well as influences tendency of bed load sediment transport rate. The calculation was incorporated into FSSM, and applied to the simulation of wave-induced topographic change in artificial shallows. Numerical results showed that an increase in the content ratio of the clay, cohesive resistance force per unit surface area and water content increased the critical Shields parameter, thus reduced the topographic change of the shallows. Based on the numerical results, cohesive effects should be considered in analysis of behavior of mixed soil containing cohesive sediments such as dredged sand since the different wave-induced topographic change was shown despite of small quantity of cohesive sediments.

On the basis of the numerical results of the effects of cohesive sediments, it was required to verify the modified model and the trend of sediment transport of mixed soil in laboratory experiments. Chapter 5 described the results of experiments of sediment transport and topographic change in mixed soil conditions exposed to steady flow in the open channel and regular waves in the wave flume with the tidal flat structure. The influence of cohesive sediments on sediment transport in cohesive and non-cohesive sediment mixtures was investigated. Kaolin was employed as cohesive sediments. In the open channel experiments, the sediment transport rate q was

investigated with the influence of clay and steel slag increasing resistance force by cohesive effects and surface roughness by adding to sand on sediment transport under the same hydrodynamic condition. From the results, both the steel slag and clay mixtures decreased q and the effects of a decrease in q for steel slag mixtures were larger than that for clay mixtures in the same content ratio p_f . In the wave flume experiments, an increase in wave height led to increasing shoreline retrogression and broadening eroded area with ripple formation with time in the sandy tidal flat. However, in the sand-clay tidal flat, the topographic change was characterized by the little topographic change without ripple formation in the early stage, the advanced crown in the final profile, and the loss of clay on the surface layer of the tidal flat with time. Moreover, the opposite crown migrations between sandy and sand-clay tidal flats were observed. The modified critical Shields parameter considering cohesive force (Chap. 4) showed better performance to evaluate sediment transport in the sand-clay tidal flat. Thus, it was highlighted once more to take into account cohesive effects when discussing the sediment dynamics in mixed soil conditions. The modified critical Shields parameter also showed the possibility of prediction of the degree of the clay loss in a roundabout way. The numerical model considering cohesive effects proposed in Chap. 4 was applied to the experimental condition of the sand-clay tidal flat. Despite of a situation capable of improvement for accurate analysis in sediment calculation, the applicability of the model to mixed soil condition was confirmed.

As summarized above, the author confirmed the importance of the consideration of pore-water pressure in fine non-cohesive sediment analysis and the cohesive effects in analysis of the mixed soil including cohesive sediments. The applicability of the proposed sediment transport calculation considering cohesive effects to the estimations of behavior of mixed soil in experiments as well as in numerical simulations was confirmed.

Although the author obtained the aforementioned main conclusions, there are still unsolved assignments. The effects of pore-water pressure shown in Chap. 2 is limited to fine sand with $d_{50} = 0.1$ mm in the present study. Thus, it remains open to question when sediments composing shallows are finer than 0.1 mm. In addition, it remains to investigate why pore-water pressure has small effects on sediment transport in some experimental cases, why the effects of pore-water pressure depend

on the direction of the sediment transport and whether the effects of pore-water pressure on sediment transport are affected by other parameters besides the median grain size of sediment particles. It is recommended that further research be conducted to address these issues.

In numerical prediction of sediment transport, there are many parameters to influence sediment calculations, *e.g.*, the horizontal critical Shields parameter, the angle of repose, the adoption of bottom velocity to be used in sediment transport calculation, *etc.* In addition, this study focused on the topographic change in the early stage due to the computational load. The prediction of initial topographic change is important because the trend of topographic change depends on the initial stage as shown in Chap. 3. However, the predictive capability of the FSSM is still left as a question in longer simulation time. For improving accuracy and performance of the simulation, the establishment of optimal value of parameters and the computation with longer simulation time are required from further numerical studies.

Furthermore, lots of variables relevant to cohesive sediment problems are still unrevealed subjects. In the present study, only physical factors of cohesive sediments were considered to sediment calculation in mixed soil condition with a small volume of cohesive sediments. However, to investigate the stability of the structures composed of dredged sand, other factors introduced in Chap. 1 should be considered and more studies are required.

In the proposed sediment calculation, cohesive resistance force per unit surface area f_c is the physical parameter of cohesive sediments estimated by experiments. However, as mentioned in Ashida *et al.* (1982), the relationship between f_c and shear stress has little consistency. For improving the applicability of the sediment calculation, the precise correlations between them should be established from experiments.

In addition, cohesive effects were incorporated into the critical Shields parameter and bed load sediment transport rate in this study, while in the experiments, the loss of the clay with experimental time was observed. Although the possibility to predict the degree of the clay loss was confirmed by using the modified critical Shields parameter with the adjustment of the content ratio of the clay p_f , the separation of migrated sediments was not considered in this study. With time, the

balance of cohesive sediments uniformly distributed in soil structures is lost because of the loss of the cohesive sediments as shown in the experiments. The sediments on accretion area contains little cohesive sediments since most of deposited sediments were traveled with little cohesive sediments after the process of the loss of cohesive sediments, while the sediments on erosion area has relatively more cohesive sediments due to remained cohesive sediments existing from the initial stage. This imbalance condition of cohesive sediments led to different sediment transport which was not included in the prediction of the proposed model assuming the well distributed cohesive sediment condition at all times during a simulation. Thus, the consideration of this imbalance condition of cohesive sediments is also a required task for better understandings of behavior of mixed soil and improvements of the predictive capability of the model.

Since this study targeted dredged sand structures, wave-induced topographic change was estimated based on the sand particles. However, the investigation of the effects of cohesive sediments suspended and reattached is recommended in future studies. Suspended cohesive sediments have the possibility to induce more sediment transport on the surface of the soil structures due to non-Newtonian fluid containing cohesive sediments, thus agitating forces acting on sand particles increase. On the other hand, reattached cohesive particles seem to play a role to increase resistance forces of incipient motion of sand particles different from suspended cohesive sediments. Therefore, further studies about these effects of traveled cohesive sediments are required.

REFERENCES

- Amos, C. L., Sutherland, T. F., & Zevenhuizen, J. (1996). The stability of fine-grained sediments in a subarctic estuary. *Sedimentology* , 43 (1), 1-19.
- Ariathurai, R., & Arulanandan, K. (1978). Erosion rates of cohesive soils. *Journal of the hydraulics division* , 104 (2), 279-283.
- Arulanandan, K. (1975). Fundamental aspects of erosion of cohesive soils. *Journal of the Hydraulics Division* , 101 (5), 635-639.
- Ashida, K., Egashira, S., & Kamoto, M. (1982). Study on the erosion and variation of mountain streams - on the erosion and transportation of sand-clay mixtures. *Disaster Prevention Research Institute Annuals B* , 25 (B2), pp. 349-360 (in Japanese).
- Bagnold, R. A. (1954). Experiments on a gravity-free dispersion of large solid spheres in a Newtonian fluid under shear. *Proceedings of the Royal Society of London* , 225 (1160), pp. 49-63.
- Bennett, R. H., O'Brien, N. R., & Hulbert, M. H. (1991). *Determinants of clay and shale microfabric signatures: processes and mechanisms*. New York: Springer-Verlag.
- Bhattacharya, P. K. (1971). *Sediment suspension in shoaling waves*. Ph D thesis, University of Iowa, Iowa.
- Brackbill, J. U., Kothe, B. D., & Zemach, C. (1992). A continuum method for modeling surface tension. *Journal of Computational Physics* , 100 (2), 335-354.
- Brooks, N. H. (1963). Discussion of 'Boundary shear stresses in curved trapezoidal channels' by A. T. Ippen and P. A. Drinker. *Journal of the Hydraulic Division, ASCE* , 89 (HY3), 327-333.

- Brø, B. (1999). Numerical modeling of flow and scour at pipelines. *Journal of Hydraulic Engineering* , 125 (5), 511-523.
- Carling, P. A. (1983). Threshold of coarse sediment transport in broad and narrow natural streams. *Earth Surface Processes and Landforms* , 8, 1-18.
- Chepil, W. S. (1959). Equilibrium of soil grains at the threshold of movement by wind. *Soil Science Society of America Proceedings* 23, (pp. 422-428).
- Chepil, W. S. (1958). The use of evenly spaced hemispheres to evaluate aerodynamic forces on a soil surface. *American Geophysical Union, Transactions* , 39, 397-404.
- Chepil, W. S. (1961). The use of spheres to measure lift and drag on wind-eroded soil grains. *Soil Science Society of America Journal* , 25 (5), 343-345.
- Coleman, N. L. (1967). A theoretical and experimental study of drag and lift forces acting on a sphere resting on a hypothetical stream bed. *Proceedings of 12th International Association for Hydraulic Research*, 3, pp. 185-192.
- Dade, W., Nowell, A., & Jumars, P. (1992). Predicting erosion resistance of muds. *Marine Geology* , 105, 285-297.
- Dancey, C. L., Diplas, P., Papanicolaou, A., & Bala, M. (2002). Probability of individual grain movement and the threshold condition. *Journal of Hydraulic Engineering* , 128 (12), 1069-1075.
- Dennett, K. E., Sturm, T. W., Amirtharajah, A., & Mahmood, T. (1998). Effects of adsorbed natural organic matter on the erosion of kaolinite sediments. *Water Environment Research* , 70 (3), 268-275.
- Dey, S., & Raju, U. (2002). Incipient motion of gravel and coal beds. *Sadhana* , 27 (5), 559-568.
- Dou, G. (1962). Theorie de l'entrainement des particules sedimentaires. *Scientia Sinica*, vol. XI, Nr. 7, Trad. 1314 CREC .
- Dubois, P. (1879). Le rhone et les rivieres a lit affouillable. *Annales des Ponts et Chaussees, Series 5* , 18, 141-195.

-
- Egiazaroff, I. V. (1965). Calculation of non-uniform sediment concentrations. *Journal of Hydraulic Division, ASCE* , 91, 225-247.
- Einstein, H. A. (1950). The bed-load function for sediment transportation in open channel flows. *Washington: U. S. Department of Agriculture* , 71P.
- Einstein, H. A., & El-Samni, E. A. (1949). Hydrodynamic forces on a rough wall. *Reviews of Modern Physics* , 21, 520-524.
- Engelund, F., & Fredsøe, J. (1976). A sediment transport model for straight alluvial channels. *Nordic Hydrology* , 7 (5), 293-306.
- Engelund, F., & Fredsøe, J. (1982). Hydraulic theory of alluvial rivers. *Advances in Hydroscience* , 13, 187-215.
- Fenton, J. D., & Abbott, J. E. (1977). Initial movement of grain on a stream bed: the effect of relative protrusion. *Proceedings of the Royal Society of London. A. Mathematical and Physical Sciences*, 352, pp. 523-537.
- Fenton, J. D., & Abbott, J. E. (1977). Initial movement of grains on a stream bed: the effects of relative protrusion. *Proceedings of the Royal Society of London*, 352, pp. 523-537.
- Fredsøe, J., & Deigaard, R. (1992). *Mechanics of Coastal Sediment Transport* (Advanced Series on Ocean Engineering 3 ed.). Singapore: World Scientific.
- Garcia, M., & Parker, G. (1991). Entrainment of bed sediment into suspension. *Journal of Hydraulic Engineering* , 117 (4), 414-435.
- Great Lakes Commission. (2013). *Beneficial use of dredged material in Great Lakes*. Great Lakes Dredging Team.
- Hattori, M. (1969). The mechanics of suspended sediment due to standing waves. *Coastal Engineering, JSCE* , 12, 69-81.
- Hjulström, F. (1939). Transportation of debris by moving water. *Recent Marine Sediments* (pp. 5-31). Oklahoma: American Association of Petroleum Geologists.

Horikawa, K., Watanabe, A., & Katori, S. (1982). Sediment transport under sheet flow condition. *Proceeding of 18th International Conference on Coastal Engineering*, 1 (18), pp. 1335-1352.

Japanese Ministry of Land, Infrastructure, Transport and Tourism. (2010). *Ministry of Land, Infrastructure, Transport and Tourism*. Retrieved from MLTT website: http://www.mlit.go.jp/statistics/details/port_list.html

Jeffreys, H. (1929). On the transport of sediment by streams. *Proceedings Cambridge Philosophy Society*, 25(3), pp. 272-276. Cambridge University Press.

Kamphuis, J., & Hall, K. Cohesive material erosion by unidirectional current. *Journal of Hydraulic Engineering*, 109 (1), 49-61.

Kang, Y., Takahashi, S., Nonomura, O., Takano, T., & Kuroda, T. (2000). A fundamental experiment on the stability of the artificial tideland. *Proceedings of Coastal Engineering, JSCE*, 47, pp. 526-530 (in Japanese).

Kawasaki, K. (1999). Numerical simulation of breaking and post-breaking wave deformation process around a submerged breakwater. *Coastal Engineering Journal, JSCE*, 41 (3-4), 201-223.

Kawata, Y. (1989). Sediment transport rate on a sloping beach. *Proceedings of Coastal Engineering, JSCE*, 36, pp. 289-293 (in Japanese).

Kazama, T., Nakata, K., Tanabe, Y., Hasegawa, M., Oshima, I., & Nagakura, T. (2006). Tidal flats and shallows created through the utilization of dredged sand and its effectiveness on coastal sea environment and its problem. *Proceedings of JSCE in the Ocean*, 22, 607-612 (in Japanese).

Kelin. (2004). Chapter 9. Threshold of movement. Course Notes: MIT OpenCourseWare.

Kelly, W. E., & Gularte, R. C. (1981). Erosion resistance of cohesive soils. *Journal of the Hydraulics Division*, 107 (10), 1211-1224.

Kemp, P. H. (1960). The relationship between wave action and beach profile characteristics. *Proceedings of 7th International Conference on Coastal Engineering, ASCE*, (pp. 262-277). Hague.

-
- Komar, P. D., & Miller, M. C. (1974). The initiation of oscillatory ripple marks and the development of plane-bed at high stresses under waves. *Journal of Sedimentary Research* , 45 (3), 697-703.
- Kramer, H. (1935). Sand mixtures and sand movement in fluvial models. *Transactions of ASCE* , 100, 798-878.
- Lambe, T. W., & Whitman, R. V. (2008). *Soil Mechanics SI version*. Wiley India Pvt. Limited.
- Li, L., Barry, D. A., Pattiaratchi, C. B., & Masselink, G. (2002). BeachWin: modeling groundwater effects on swash sediment transport and beach profile changes. *Environmental Modelling & Software* , 17 (3), 313-320.
- Liang, D., & Cheng, L. (2005). Numerical model for wave-induced scour below a submarine pipeline. *Journal of Waterway, Port, Coastal and Ocean Engineering, ASCE* , 131 (5), 193-202.
- Lick, W., Jin, L., & Gailani, J. (2004). Initiation of movement of quartz particles. *Journal of Hydraulic Engineering* , 130 (8), 755-761.
- Liu, X., & Garcia, M. H. (2008). Three-dimensional numerical model with free water surface and mesh deformation for local sediment scour. *Journal of Waterway, Port, Coastal, Ocean Engineering, ASCE* , 134 (4), 203-217.
- Luque, R. F., & van Beek, R. (1976). Erosion and transport of bed-load sediment. *Journal of Hydraulic Research* , 14 (2), 127-144.
- Manohar, M. (1955). *Mechanics of bottom sediment movement due to wave action*. Mechanics of bottom sediment movement due to wave action, Dayton.
- McCave, I. N. (1984). Erosion, transport and deposition of fine-grained marine sediments. *Geological Society of London, Special Publication* (15).
- Miedema, S. A. (2013). Constructing the Shields Curve: Part C - Cohesion by Silt, Hjulstrom, Sundborg. *Proceedings of ASME 2013 32nd International Conference on Ocean, Offshore and Arctic Engineering*. 6, p. 19P. Nantes, France: OMAE2013.

Millar, R. G., & Quick, M. C. (1998). Stable width and depth of gravel bed rivers with cohesive banks. *Journal of Hydraulic Engineering* , 124 (10), 1005-1013.

Miller, M. C., McCave, I. N., & Komar, P. D. (1977). Threshold of sediment motion under unidirectional currents. *Sedimentology* , 24, 507-527.

Mitchener, H., & Torfs, H. (1996). Erosion of mud/sand mixtures. *Coastal Engineering* , 29 (1), 1-25.

Miura, K., Morimasa, S., Ohtsuka, N., Yamazaki, H., & Konami, T. (2010). Combined effect of flow velocity and water pressure change on wave-induced seabed destabilization. *Journal of Japan Society of Civil Engineers, Series. B2 (Coastal Eng.)*, JSCE , 66 (1), 851-855 (in Japanese).

Mizutani, N., McDougal, W. G., & Mostafa, A. M. (1996). BEM-FEM combined analysis of nonlinear interaction between wave and submerged break-water. *Proceedings of 25th International Conference on Coastal Engineering, ASCE, Orlando* , pp. 2377-2390.

Nakamura, M., & Ishikawa, K. (2007). *Construction method of tidal flats*. Tokyo: Kouseisha Kouseikaku Co., Ltd. (in Japanese).

Nakamura, T., & Mizutani, N. (2010). Numerical simulation of local scouring around inland structure due to run-up tsunami using three-dimensional coupled fluid-structure-sediment interaction model. *Proceedings of 24th CFD Symposium, JSFM* , E10-4, p. 9P (in Japanese).

Nakamura, T., & Mizutani, N. (2011). Three-dimensional coupled fluid-sediment interaction numerical model for suspended sediment analysis. *Proceedings of the 2011 International Offshore and Polar Engineering Conference, ISOPE* , pp. 1032-1039.

Nakamura, T., & Yim, S. C. (2011). A nonlinear three-dimensional coupled fluid-sediment interaction model for large seabed deformation. *Journal of Offshore Mechanics and Arctic Engineering, ASME* , 133 (3), 031103-1-031103-14.

Nakamura, T., Ishihara, R., & Mizutani, N. (2012). Numerical analysis of topographic change of artificial shallow considering pore-water pressure in surface layer of

shallow. *Journal of JSCE Series B2 (Coastal Engineering)*, JSCE , 68, I_1161-I_1165 (in Japanese).

Nakamura, T., Ishihara, R., & Mizutani, N. (2011). Two-dimensional numerical analysis of wave-induced instability of artificial shallow composed of dredged soil. *Proceedings of Coastal Structures 2011, ASCE, Yokohama, D7-134* , pp. 1421-1432.

Nakamura, T., Kuramitsu, Y., & Mizutani, N. (2008). Tsunami scour around a square structure. *Coastal Engineering Journal, JSCE* , 50 (2), 209-246.

Nakamura, T., Yim, S. C., & Mizutani, N. (2011). Numerical simulation on local scouring around bottom-mounted movable short cylinder. *Proceedings of Coastal Structures 2011, ASCE* , p. 12P.

National Astronomical Observatory of Japan. (2003). *Chronological Scientific Tables*. Tokyo, Japan: Maruzen Cooperation.

Neil, C. R. (1968). Note on initial movement of coarse uniform bed-material. *Journal of Hydraulic Research* , 6, 173-176.

Nielsen, P. (1992). *Coastal bottom boundary layers and sediment transport* (Vol. 4). World Scientific.

Nielsen, P., Svendsen, I. A., & Staub, C. (1978). Onshore-offshore sediment movement on a beach. *Proceedings of 16th International Conference on Coastal Engineering*. 2, pp. 1475-1492. Hamburg: ASCE.

Parchure, T. M., & Mehta, A. J. (1985). Erosion of soft cohesive sediment deposits. *Journal of Hydraulic Engineering, ASCE* , 111 (10), 1308-1326.

Parker, G., Paola, C., & Leclair, S. (2000). Probabilistic Exner sediment continuity equation for mixtures with no active layer. *Journal of Hydraulic Engineering, ASCE* , 126 (11), 818-826.

Paterson, D. M. (1994). Microbiological mediation of sediment structure and behaviour. *Microbial Mats NATO ASI* , 35, 97-109.

Petit, F. (1994). Dimensionless critical shear stress evaluation from flume experiments using different gravel beds. *Earth Surface Processes and Landforms* , 19 (6), 565-576.

Postma, H. (1967). Sediment transport and sedimentation in the estuarine environment. *Estuaries*, G. H. Lauff Editor, American Association for Advancement of Science, Washington D. C. Publication 83 , 158-179.

Ravisangar, V., Dennett, K. E., Sturm, T. W., & Amirtharajah, A. (2001). Effect of sediment pH on resuspension of kaolinite sediments. *Journal of environmental engineering* , 127 (6), 531-538.

Roulund, A., Sumer, B. M., Fredsøe, J., & Michelsen, J. (2005). Numerical and experimental investigation of flow and scour around a circular pile. *Journal of Fluid Mechanics* , 534, 351-401.

Sakai, T., Goto, H., Harada, E., & Yeganeh-Bakhtiary, A. (2002). Unsteadiness of armoring in oscillatory sheet flow of graded sediment. *Proceedings of 28th International Conference on Coastal Engineering, ASCE* , pp. 2948-2986.

Sakakiyama, T., Ito, Y., Kobayashi, M., Itai, M., & Kobayashi, E. (2004). Numerical simulation of sediment transport through rubble mound breakwater. *Annual journal of Coastal Engineering, JSCE* , 51, 456-460 (in Japanese).

Schnitzer, M., & Khan, S. U. (1972). *Humic substances in the environment*. New York: Marcel Dekker.

Sherard, L. J., Decker, R. S., & Ryka, N. L. (1972). Piping in earth dams of dispersive clay. *ASCE Soil Mechanics and Foundation Conference*, (pp. 12-14). Lafayette.

Shields, A. (1936). Anwendung der Ähnlichkeitsmechanik und der Turbulenzforschung auf die Geschiebebewegung. *Mitteilungen der Preussische Versuchsanstalt für Wasserbau und Schiffbau* , 26, 25P.

Sumer, B. M., & Deigaard, R. (1981). Particle motions near the bottom in turbulent flow in an open channel. *Journal of Fluid Mechanics* , 109, 311-338.

- Sumer, B. M., Sen, M. B., Karagali, I., Ceren, B., Fredsøe, J., Sottile, M., et al. (2011). Flow and sediment transport induced by a plunging solitary wave. *Journal of Geophysical Research: Oceans (1978-2012)*, 116 (C1), 15P.
- Sunamura, T., & Horikawa, K. (1974). Two-dimensional beach transformation due to waves. *Proceedings of 14th International Conference on Coastal Engineering, ASCE*, pp. 920-938.
- Sunborg, A. (1956). The River Klaralven: Chapter 2. The morphological activity of flowing water-erosion of the stream bed. *Geografiska Annaler*, 38, 165-221.
- Suzuki, T., Okayasu, A., & Shibayama, T. (2007). A numerical study of intermittent sediment concentration under breaking waves in the surf zone. *Coastal Engineering*, 54 (5), 433-444.
- Takahashi, S., Suzuki, K., Kang, Y., & Tsunakazu, K. (1997). An experiment on liquefaction of fine sand seabed due to waves., 44, pp. 916-920 (in Japanese).
- Tonkin, S., Yeh, H., Kato, F., & Sato, S. (2003). Tsunami scour around a cylinder. *Journal of Fluid Mechanics*, 496, 165-192.
- Tooby, P. F., Wick, G. L., & Isacs, J. D. (1977). The motion of a small sphere in a rotating velocity field: A possible mechanism for suspending particles in turbulence. *Journal of Geophysical Research*, 82 (15), 2096-2100.
- U.S. Army Corps of Engineers (COE). (1994). *Engineering and Design: Channel Stability Assessment for Flood Control Projects*. Vicksburg: U.S. Army Engineer Waterways Experiment Station.
- Vanoni, V. A., Benedict, P. C., Bondurant, D. C., Mckee, J. E., Piest, R. F., & Smallshaw, J. (1966). Sediment transportation mechanics: initiation of motion, progress report of the task committee on preparation of sedimentation manual. *Journal of the Hydraulics Division, ASCE*, 92 (2), 291-314.
- Weiberg, P. L., & Smith, J. D. (1987). Calculations of the critical shear stress for motion of uniform and heterogeneous sediments. *Water Resources Research*, 23, 1471-1480.

White, C. M. (1940). The equilibrium of grains on the bed of a stream. *Proceedings of the Royal Society of London*, 174, pp. 322-338.

White, S. (1970). Plane bed thresholds of fine grained sediments. *Nature* , 228, 152-153.

Wilson, K. C. (1966). Bed-load transport at high shear stress. *Journal of Hydraulic Engineering* , 113 (1), 97-103.

Yalin, M. S. (1977). *Mechanics of Sediment Transport* (2nd Edition ed.). Oxford, U.K.: Pergamon.

Zanke, U. C. (1982). *Grundlagen der Sedimentbewegung*. Berlin, Heidelberg: New York: Springer Verlag.

Zanke, U. C. (1977). *Neuer Ansatz zur Berechnung des Transportbeginns von Sedimenten unter Stromungseinfluss*. Germany: Mitteilungen des Francius Instituts, Technical University Hannover.

Zanke, U. C. (2003). On the influence of turbulence on the initiation of sediment motion. *International Journal of Sediment Research* , 18 (1), 17-31.

Zen, K., & Yamazaki, H. (1990). Mechanism of wave-induced liquefaction and densification in seabed. *Soils and Foundations* , 30 (4), 90-104.

CHO Yong-Hwan

Ph.D. Candidate, Nagoya University

1-15-1, Asaokacho, Chikusa-ku,

Nagoya 464-0811, JAPAN

Email: wbj53@nate.com

PERSONAL DATA

Name: CHO Yong-Hwan
Sex: Male
Date of Birth: March 3, 1983
Place of Birth: Seoul, KOREA
Nationality: KOREA
Marital Status: Single
Languages: Korean, Japanese and English
Current Address: 1-15-1, Asaokacho, Chikusa-ku, Nagoya 464-0811, JAPAN
Home Address: 1329-905, 100, Mokdongdong-ro, Yangcheon-gu, Seoul, 158-773, KOREA
Mailing Address: Coastal & Ocean Eng. Lab., Dept. of Civil Eng., Nagoya University, Furo-cho, Chikusa-ku, Nagoya 464-8603, JAPAN

EDUCATION

M.S. (Civil Engineering), University of Seoul, Seoul, KOREA, 2011.

B.S. (Civil Engineering), University of Seoul, Seoul, KOREA, 2009.

SCHOLARSHIPS

1. Japanese government (Monbukagakusho:MEXT) scholarship, October 1, 2011-September 30, 2014.
-

AWARDS

1. Best Paper Award, 7th International Conference on Asian and Pacific Coasts, APAC 2013, September 25, 2013.

LIST OF PUBLICATIONS

Refereed Journal Articles:

1. Nakamura, T., Cho, Y. H., Mizutani, N. and Lee, K. H. (2013): Sediment Transport Calculation Considering Cohesive Effects and its Application to Wave-induced Topographic Change of Shallows, *Journal of Japan Society of Civil Engineers, Series B3 (Ocean Engineering), JSCE*, Vol. 69, No. 2, I_1036-I_1041 (in Japanese).
2. Nakamura, T., Nezasa, Y., Cho, Y. H., Ishihara, R. and Mizutani, N. (2014): An Experimental Study on the Wave-Induced Topographic Change in Artificial Shallows, *Coastal Engineering journal (CEJ), JSCE*, Vol. 56, No. 2, pp. 1450008_4-1450008_21.
3. Cho, Y. H., Nakamura, T., Mizutani, N. and Lee, K. H. (2013): Sediment Transport Calculation Considering Cohesive Effects and Its Application to Wave-Induced Topographic Change, *Journal of Korean Society of Coastal and Ocean Engineers (KSCOE)*, 25(6), 405-411.
4. Cho, Y. H., Nakamura, T., Suzuki, M. and Mizutani, N. (2014): An Experimental Study on Influences of Cohesive Sediments on Sediment Transport of Mixed Soil, *Journal of Japan Society of Civil Engineers, Series B3 (Ocean Engineering), JSCE*, (6 pages, scheduled to be issued in 2014).
5. Cho, Y. H., Nakamura, T., Mizutani, N. and Lee, K. H. (2014): A Numerical Simulation of Wave-Induced Topographic Change in shallows Composed of Fine Sand, *Journal of Advanced Simulation in Science and Engineering (JASSE)*, (15 pages, scheduled to be issued in 2014).

Conference Proceedings:

1. Cho, Y. H., Nakamura, T., Mizutani, N. and Lee, K. H. (2013): Sediment Transport Calculation Considering Cohesive Effects and its Application to Wave-induced Topographic Change, *Proceedings of 7th Asian and Pacific Coasts (APAC 2013)*, Bali, Indonesia, 338-345.
2. Cho, Y. H., Nakamura, T., Mizutani, N. and Lee, K. H. (2013): A Numerical Simulation of Wave-Induced Topographic Change of Shallow Composed of Fine Sand, *Proceedings of 32nd International Conference on Simulation Technology (JSST 2013)*, Tokyo, Japan, 2 p.

The Others:

1. Cho, Y. H., Cho, Y. J., Nakamura, T. and Mizutani, N. (2012): Possibility of Seiche of Pohang New Port due to Edge Waves under ever Present Amplitude Modulating Swell of Narrow Band Width, *JSCE Chubu Branch Annual Meeting 2012*, II-032, 131-132.
2. Cho, Y. H., Nakamura, T. and Mizutani, N. (2013): Study on Sediment Calculation Considering Cohesive Force and Cohesive Effects on Topographic Evolution, *JSCE Chubu Branch Annual Meeting 2013*, II-11, 95-96 (in Japanese).

-
3. Cho, Y. H., Nakamura, T. and Mizutani, N. (2014): Numerical Study on Topographic Change in a Tidal Flat Considering Cohesive Effects, *JSCE Chubu Branch Annual Meeting 2014*, II-022, 109-110 (in Japanese).
 4. Suzuki, M., Cho, Y. H., Nakamura, T. and Mizutani, N. (2014): Study on Characteristics of Topographic Change in a Tidal Flat with Influences of Mixing Components, *JSCE Chubu Branch Annual Meeting 2014*, II-023, 111-112 (in Japanese).
 5. Mizutani, N., Nakamura, T., Cho, Y. H. and Shinoda, Y. (2014): Evaluation of Stability of Surface Layer Sediments Consisting of Artificial Shallows and Tidal Flat against Approaching Waves, *Japan Sediments Management Association, HEDORO*, 45(120), 10-20 (in Japanese).
 6. Cho, Y. H., Nakamura, T., Suzuki, M. and Mizutani, N. (2014): Experimental Study on Topographic Characteristics of a Tidal Flat with Cohesive Sediments and Evaluations of Sediment Transport with Modified Shields Parameters Considering Cohesive Effects, *JSCE Annual Meeting 2014*, (2 pages, scheduled to be issued in 2014), (in Japanese).
-

PROFESSIONAL SOCIETIES

1. Member of Japan Society of Civil Engineers (JSCE), 2011-present.